Low voltage fast dielectric elastomer actuators

Thèse N° 9533

Présentée le 20 septembre 2019

à la Faculté des sciences et techniques de l'ingénieur
Laboratoire des microsystèmes pour les technologies spatiales
Programme doctoral en microsystèmes et microélectronique

pour l'obtention du grade de Docteur ès Sciences

par

Xiaobin JI

Acceptée sur proposition du jury

Prof. L. G. Villanueva Torrijo, président du jury
Prof. H. Shea, Dr. S. Cantin-Rivière, directeurs de thèse
Prof. D. R. Clarke, rapporteur
Prof. J. Rossiter, rapporteur
Prof. J. Paik, rapporteuse

2019

ÉCOLE POLYTECHNIQUE
FÉDÉRALE DE LAUSANNE

Acknowledgements

I would like to thank my supervisors Prof. Herbert Shea and Prof. Sophie Cantin for giving me this great opportunity to work on this exciting PhD project. During my four-year PhD, Herb and Sophie have been encouraging and supporting me with their supervision, and advises. Their patience, guidance, trust, and support, give me the confidence and determination to overcome all the problems and keep moving on.

I would like to thank Prof. Cédric Plesse, Prof. Pierre-Henri Aubert, and especially, Prof. Frédéric Vidal, for their recommendation on this PhD position.

I really appreciate Prof. David R. Clarke, Prof. Jonathan Rossiter, and Prof. Jamie Paik for accepting to become my jury members, and Prof. Guillermo Villanueva for accepting to be the jury president.

I would like to thank Dr. Samuel Rosset and Dr. Alae El Haitami for their help in the fields of DEA and Langmuir. They have been so patient to help me from the beginning with all the details and trained me how to do the related experiments.

I would like to thank our collaborators form EPFL-LAI for their input to develop the on-board electronics for our soft robotic and wearable haptic devices.

I would like to thank Dr. Jun Shintake, Dr. Vito Cacucciolo, Dr. Mathias Imboden, Dr. Alexandre Poulin, Dr. Oluwaseun Araromi, Dr. Zarate Juan José, and Dr. Edouard Leroy. For their helpful discussion and practical help with their strong technical skills.

I thank my friends and all lab members Danick, Ulas, Fabio, Rubaiyet, Ronan, Brince, Silvia, Francis, Min, Alessio, Morgan, Sylvain, Ryan, Valentin , Francesca, Alexis, Nadine, and many others for their contribution to this dynamic laboratory environment. Especially, I would like to thank Sam and Bekir, for their kindness for being my office mate and roommate respectively. And a big thank you to our secretary Myriam, for her kindness and help during the four years.

Finally, I would like to thank my parents for all their unconditional support, understanding and help. I deeply thank my wife, Feifei, for her support, understanding, and love. I also thank our newborn baby, Ruirui, for the pleasure he brings to the whole family.

Neuchâtel, le 1 Mai 2019   X. J.

Abstract

This thesis contributes to the field of Dielectric Elastomer Actuators (DEAs). DEAs are electrostatically driven soft actuators that are fast, capable of generating large actuation strains, high forces, and present high power density. A wide range of applications have been developed based on DEAs including: soft tunable optical devices, soft robotics and wearable haptic devices. DEAs generally require several kilovolts to operate. This high voltage leads to bulky control electronics and can limit consumer acceptance.

In this thesis work, we have decreased the DEAs voltage to below 450V while maintaining high performance, and report novel applications for the low-voltage DEAs.

The approach that we use to decrease the DEAs driving voltage is decreasing the dielectric elastomer (DE) membranes thickness. When the DE membrane is made thin, the properties of electrodes used for thin DE membranes become more critical than the ones for thick DE membranes. The stretchable electrodes must be made thin and soft to achieve low stiffness to not limit the thin DE membrane actuation, and should have high electrical conductivity to enable the DEA fast charging and discharging.

We developed two types of electrodes in this thesis. The first was a thin, transparent and extremely soft ionogel electrode, which we patterned to serve as an optical grating. The ionogel served simultaneously as the transparent electrode for the DEA and as the optical grating elements. Under high electric fields, the ions in the ionogel migrated into the dielectric, limiting lifetime, especially for thin dielectrics.

We then developed ultrathin stretchable conductors based on Carbon Nanotubes, using Langmuir monolayer method for 2D assembly. The nanometer thick stretchable conductors enabled single layer DEAs with a 1.4 µm-thick silicone dielectric layer to generate 8% area strain below 100 V. To increase the DEAs output force, we increased the dielectric membrane thickness to 6 µm, and stacked the DEAs. The DEAs reached full actuation area strain of 25% at 450V, and operated at a frequency from DC to higher than 200 Hz. The sub 500 V operating voltage enabled sub-gram control electronics including battery, which allowed the integration of all the power and control elements with the DEA for compact untethered devices. The high speed enabled a broad range of applications. We developed an untethered 1 g, 4 cm long soft DEA-driven robot capable of carrying its own power supply, and autonomously navigating complex paths. We used 18 µm-thick DEAs as wearable haptic devices, capable to generate notification signals from 1 Hz to 500 Hz on the fingertip.

Abstract

We decreased the DEA operating voltage by an order of magnitude, enabling wider use of DEAs in soft robotics and wearables.

Keywords: DEA, Low-voltage DEA, stacked DEA, soft robot, untethered, wearable haptics, transparent electrode, ultra-thin stretchable electrodes.

Résumé

Cette thèse contribue à l'avancement du domaine des actionneurs souples diélectrique (DEAs). Les DEA sont des actionneurs souples actionnés électrostatiquement, ils sont rapides et capables de fournir une déformation d'actionnement, une force et une densité de puissance élevées. Différentes applications ont été développées à partir des DEAs, telles que: les dispositifs optiques accordables, les robots mous, et les dispositifs haptiques portables. Cependant, les DEAs ont généralement besoin de plusieurs kilovolts pour fonctionner. La tension de fonctionnement élevée implique un système électronique de commande encombrant et peut limiter l'acceptation du consommateur.

Dans cette thèse, nous avons diminué la tension de fonctionnement du DEAs jusqu'à moins de 450 V et développé des applications appropriées pour les DEAs fonctionant à basse tension.

L'approche que nous utilisons pour diminuer la tension de commande de la DEA consiste à réduire l'épaisseur des membranes d'élastomère diélectrique (DE). Lorsque la membrane DE devient mince, les propriétés des électrodes utilisées pour les membranes minces deviennent plus critiques que celles des membranes épaisses. Les électrodes étirables doivent être minces et souples pour obtenir une faible rigidité afin de ne pas limiter l'actionnement, et ils doivent présenter une bonne conductivité électrique pour permettre aux DEA de charger et de décharger rapidement.

Nous avons développé deux types d'électrodes dans cette thèse. La première est une électrode ionogel qui est mince, transparente et extrêmement douce, que nous avons configurée pour servir de grille optique. L'ionogel sert simultanément d'électrode transparente pour le DEA et d'élément de grille optique. Sous des champs électriques élevés, les ions de l'ionogel ont migré dans le diélectrique, limitant leur durée de vie, en particulier pour les diélectriques minces.

Par conséquent, nous avons développé des conducteurs étirables ultra-minces non ioniques à base de CNT, utilisant la technologie Langmuir pour l'assemblage en 2D.

Les conducteurs étirables nanométriques sont suffisamment souples pour permettre par la suite à nos DEA monocouches avec une couche diélectrique en silicone d'épaisseur 1,4 µm de générer une déformation surfacique de 8% en dessous de 100 V. Pour augmenter la force de la DEAs, nous avons augmenté l'épaisseur de la membrane diélectrique à 6 µm et avons développé des DEAs empilés. Les DEA atteignent une déformation surfacique d'actionnement maximale de 25% à 450 V et sont capables de fonctionner à plus de 200 Hz.

Résumé

La tension de fonctionnement inférieure à 500 V permet une électronique de commande inférieure à 1 gramme, batterie comprise, ce qui permet l'intégration de tous les éléments de puissance et de commande avec le DEA pour des appareils compacts non attachés. La vitesse de fonctionnement rapide permet une large gamme d'applications. Nous avons développé un robot non-attaché de 1 g, 4 cm de long, qui est capable de porter sa propre alimentation et de naviguer de manière autonome sur des chemins complexes. Nous rapportons l'utilisation de DEA de 18 µm d'épaisseur comme dispositifs haptiques portables, qui est capable de générer des signaux de notification de 1 Hz à 500 Hz au bout des doigts.

Nous avons réduit la tension de fonctionnement du DEA d'un ordre de grandeur, ce qui a permis une utilisation plus large des DEA dans la robotique molle et les dispositifs portables.

Mots-clés: DEA, DEA de basse tension, DEA empilé, robot mou, non-attaché, haptique portable, électrode transparente, électrodes étirables et ultraminces.

Contents

Content

List of Figures

List of Figures

List of Tables

Chapter 1   Introduction

1.1   Background and motivation

Autonomous systems play an important role in industry automation, vehicles, medical surgical robot, and even household appliances such as robotic vacuum cleaners. One key element in these systems is the actuator, which is generally made from rigid materials. Rigid actuators are powerful, can output large mechanical power, maintain stable performance under extreme conditions, and are capable of precise positioning and displacement. However, with increased requirements from applications, actuators need to be capable to generate actuation even when deformed or stretched and should offer multi degree of freedom to adapt the complex and uncontrolled environments. Examples of these applications can be found in on-body actuation, actuation in uncontrolled space (exploration), and actuation on irregular deformable objects (living organs). To meet these requirements, compliance needs to be integrated with actuators. For these reasons, soft actuation technologies have been developed (*1*).

Soft actuation technologies have some advantages over traditional rigid actuation, such as deformability, lower cost, and low mass (*2–4*). They have shown promising applications in the fields of biomimetic, human machine interface, soft robotics and medical application. Nevertheless, soft matter presents several drawbacks compared with the rigid systems, such as much lower output force, less precision, and slower speed. Especially for small size (several cm^3) untethered systems, the low output power of the soft actuators cannot even carry their own power and control systems to achieve untethered soft robots. Research activities are ongoing to develop and improving the performance of the soft actuators, and trying to push the soft actuation technologies for untethered applications.

Dielectric Elastomer Actuators (DEAs) are one type of promising soft actuators. DEAs can achieve fast operation with kHz frequency (*5*). DEAs can output giant actuation deformation (*6, 7*) and are highly efficient. DEAs can be miniaturized to an active volume down to the range of 10^{-11} m^3 (*8*). Giving the above-mentioned features, DEAs are focused in this thesis work.

One major drawback for DEAs is that they need typically several kilovolts to tens of kilovolts to operate. The high operating voltage limits the adoption of DEAs. The electronics for generating high voltage are heavy and bulky compared to the actuators themselves which limits the miniaturization of the whole integrated systems, and high voltage can limit consumer acceptance. Decreasing the DEA operating voltage is really necessary to expand the potential of DEAs.

1.2   Research objective and challenges

The aim of this thesis is to decrease the operating voltage of DEAs and to improve their performance. It addresses challenges in the field of DEAs regarding materials, fabrication technology, and applications.

Decreasing the operating voltage of DEAs is extremely challenging. Different approaches have been investigated in recent years. However all the developed low-voltage DEAs present much degraded performances. In this thesis, the approach chosen for decreasing the DEA operating voltage is to decrease the DE membrane thickness. To develop high performance low-voltage DEAs using this approach, the following works need to be done:

- New materials should be investigated as the DEA electrodes. High performance electrodes should be ultrathin (nm-thick), soft (Young's modulus less than 10 MPa), stretchable (without significant degradation of conductivity until 20% stretch) and have good surface resistance (less than 2 MΩ/sq) at the same time. This is the main objective of this thesis and serves as the basis for further steps. The electrode properties set the DEA performance.

- New fabrication technologies need to be developed using sub-μm-thick dielectric elastomer membrane for DEA construction. Methods to handle sub-μm-thick elastomer membranes should be developed. Suitable electrode patterning method should be investigated.

- Technologies for making stacked DEAs (driving voltage below 500V) should be developed. The electrode interconnection methods should be developed. The interlayer lamination should be investigated.

- Novel applications must be developed with the freshly developed low-voltage DEAs. Small scale untethered smart devices must be invented based on the developed high performance DEAs with low actuation voltage.

1.3   Thesis contributions and outline

This thesis contributes to the field of low-voltage DEAs. The actuation voltage of the DEA is decreased by one order of magnitude compared with the typical ones. The developed DEA materials and fabrication method allow the construction of high performance DEAs, which are fast (operating over 200 Hz), and capable of output more than 20% area strain with a driving voltage below 450V. The developed multilayer fabrication process allows to improve the DEA output force. The main contribution is the development of ultrathin stretchable electrodes using Langmuir monolayer method. The low stiffness and good surface resistance are the key elements which allow the fabricated DEA to output the excellent performance.

The thesis is structured as follows:

State-of-the-art:

Chapter 2 summarizes the current soft actuation technologies used for soft robots and wearable devices. Examples are given for the corresponding untethered devices. DEAs show overall advantages regarding to the actuator speed, strain and efficiency compared with other soft actuation technologies.

Chapter 3 summarizes the working principles, current materials and fabrication technologies for DEAs. The limitation of DEAs and proposed improvements are discussed. Then we explained the key elements to build high-performance low-voltage DEAs and highlighted the importance of the role of the stretchable electrodes.

Work done during this thesis:

Chapter 4 presents thin and soft electrodes based on ionogel. The ionogel-based stretchable conductors present excellent optical transparency. As the dielectric layers of DEAs are transparent as well, we have fabricated fully transparent tunable grating devices driven by DEAs (Figure 1.1). With micro-patterned ionogel surface, the transparent soft ionogel serves both as the electrodes for the DEAs, and as the transparent optical grating elements.
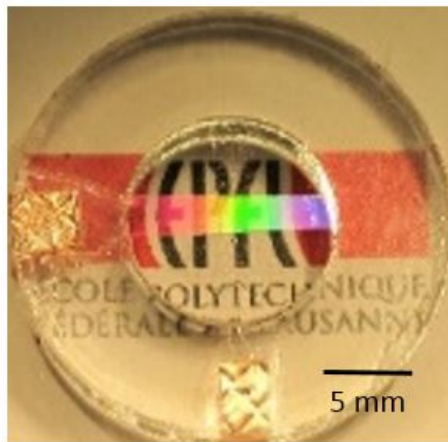
Figure 1.1 Tunable grating with ionogel electrodes driven by DEA.

Chapter 5 presents ultrathin stretchable electrodes based on Carbon Nanotubes (CNT), which are the key elements for the fabrication of the low-voltage DEAs. We use the Langmuir monolayer technology to assemble amphiphilic composite materials in 2 dimensions (2D). Based on the nm-thick 2D assembled stretchable electrodes, we have fabricated single layer 1 µm-thick DEAs generating 4% linear strain with just 100 V as driving voltage, an order of magnitude lower than the typical DEA driving voltage. This serves as the basic element of a stacked actuator. Stacking allows the increase of the actuation force while maintaining the low actuation voltage. To further improve the global actuator output force, we increased the single layer DEA thickness to 6 µm-thick and developed low-voltage stacked DEAs (LVS-DEA) reaching full actuation strain at only 450 V, and capable to operate over 200 Hz.
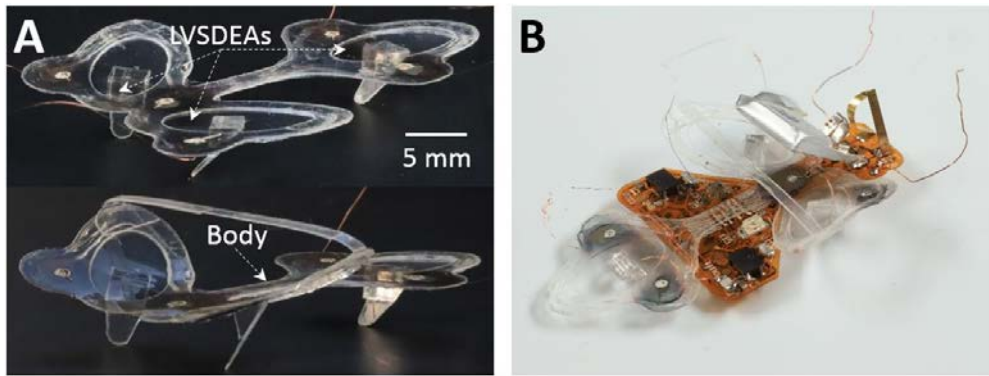
Figure 1.2 Photo of soft robot driven by LVSDEAs. (A) Photo of soft robot with flat (up) and deformed (down) body. (B) Photo of untethered autonomous soft robot.
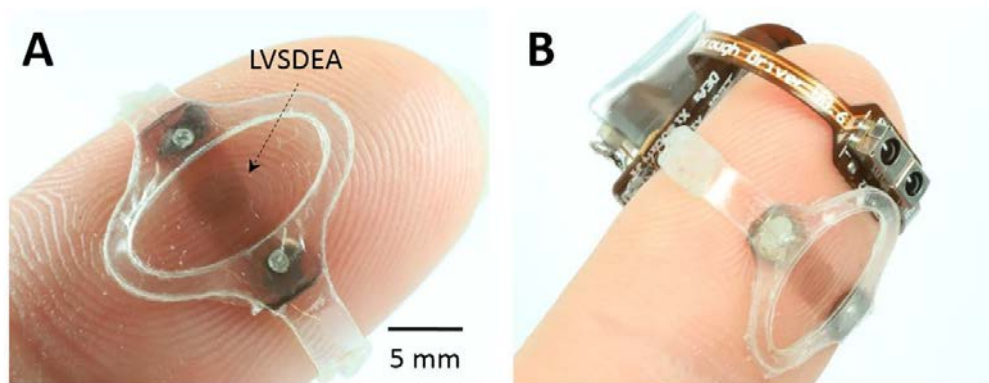
Figure 1.3 Photo of "feel-through" haptic device driven by LVSDEA. (A) Photo of the haptic device on fingertip. (B) Photo of the untethered haptic device.

Chapter 6 demonstrates applications based on the developed LVSDEAs. We first use our LVSDEAs to drive a soft robot. Our soft robot is fast (speed 18 mm/s), ultralight (190 mg), robust (can be crushed and then resume its activities), strong (can move with carrying 5 times its body weight) and steerable (Figure 1.2A). With 800 mg integrated control and power elements (including battery) (Figure 1.2B), our robot can autonomously perform tasks, such as navigate a complex path. This is the first autonomous untethered soft robot in small scale (4 cm-long). We then present wearable "feel-through" haptic devices using our LVSDEA as miniaturized human-machine interface (Figure 1.3A). By mounting the LVSDEA directly on the fingertip, the wearer can feel notification signals from 1 Hz to 500 Hz generated from the actuation of the stacked DEAs. Wearing the untethered "feel-through" (Figure 1.3B), with the help of the received notifications, the user with eyes shielded can use his finger to "see" the color and read randomly placed and oriented letters covered by plastic plate.

In Chapter 7, we conclude this thesis work, and propose corresponding possible future development.

Chapter 2   Soft actuation technologies

Current soft actuation technologies include fluidic elastomer actuators (*2*, *9–29*), thermally induced soft actuation (*30–49*), magnetic elastomer actuators (*50–55*), and electroactive polymers-based soft actuators (*5*, *56–66*). Selected examples of untethered devices are given in Figure 2.1, corresponding to the above-mentioned soft actuation technologies. The chosen examples represent the advances in the related fields, including: integration with auxiliary systems; robustness; excellent demonstration for exploration capability; miniaturized and lightweight devices.

Other soft actuation technologies have been reported such as Liquid Crystal Elastomers (LCE) (*67*), gels driven by swelling/deswelling process (*68*), PVC gels driven by electrostatic force (*69*), and gels using Belouzov-Zhabotinsky chemical reactions (*70*) to generate motion.

2.1   Fluidic elastomer actuators

Fluidic elastomer actuators (FEAs) were developed under the name of McKibben artificial muscle in the 1950s (*71*). The FEAs need a closed elastomer-based chamber (typically silicone elastomer) with fluid (air/water) inlet. The actuation principle is based on the pressure change inside the elastomer chamber (*2*). Depending on the fluid materials for generating the pressure difference, FEAs can be classified into two categories, Pneumatic Soft Actuators (PSA) and Hydraulic Soft Actuator (HSA). PSAs use gas as fluid, and are driven pneumatically (*11*, *12*, *17*, *19–24*, *28*, *29*). HSAs use liquid as fluid, and are driven hydraulically (*25–27*). Some devices can be driven both pneumatically or hydraulically (*10*). By using different designs, they can usually generate bending (*11*, *17–19*, *24*, *28*), extension (*12*, *21*), contraction (*29*) and twisting (*10*). Pumps, compressors, and compressed air with regulators are generally used as pressure sources, combined with valves for the controlling. There are also electro-thermal (*20*), chemical reaction (*13*) and combustion (*14*, *72*) technologies for generating the air pressure difference. FEAs have been primarily used for soft robotics such as moving robots (*12*, *14*, *17*, *27*, *72*) and grippers (*22*, *28*), and for wearables such as haptic devices (*15*, *16*, *23*) and soft exoskeletons (*18*, *26*). High output force of more than 300N (*21*) has been reported based on FEAs.

Figure 2.1A shows an untethered crawling robot powered with on-board integrated air compressor (*19*). This example is chosen because it shows that soft robots can remain functional under a variety of adverse environmental conditions with excellent robustness. This robot is

about 65 cm-long. It is driven by 6 PSAs with Pneumatic Network (*11*) architecture. The PSAs are actuated by two on-board miniaturized air compressors, using solenoid valves as switches, controlled by microcontroller and powered by battery. The untethered robot moves with a speed of about 5 mm/s.
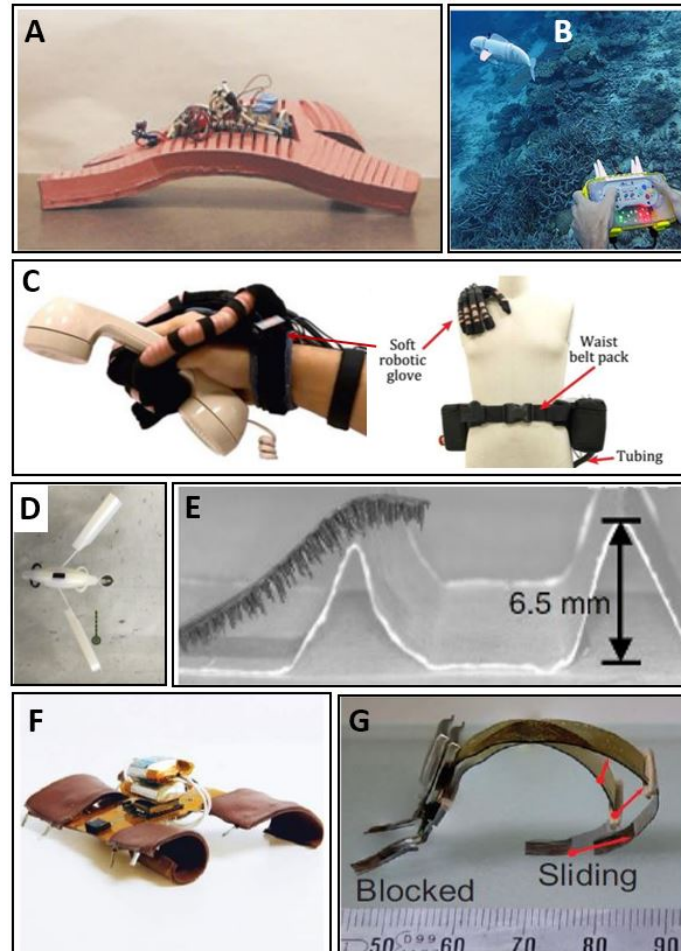
Figure 2.1 Examples of untethered robots driven by different soft actuation technologies. (A) Untethered soft pneumatic actuators driven robot (adapted from (*19*)). (B) Untethered robotic fish driven by hydraulic soft actuator (adapted from (*27*)). (C) Untethered hydraulic soft actuator driven soft robotic glove for hand rehabilitation (adapted from (*26*)). (D) Untethered swimming robot driven by shape memory polymer (adapted from (*30*)). (E) Untethered soft robot driven by magnetic elastomer actuator (adapted from (*50*)). (F) Untethered quadruped robot driven by shape memory alloy embedded in elastomer matrix (adapted from (*40*)). (G) Untethered robot driven by ionic polymer-metal composite (adapted from (*56*)).

A swimming untethered soft robot termed as "SoFi" is shown in Figure 2.1B (*27*). This example is chosen to represent the soft robots driven by HSAs, because it demonstrates a new approach for underwater exploration using biomimetic soft robots. Using HSAs enables the exchange of liquid in close-loop between the two inner cavities by using a custom-designed gear pump. Therefore SoFi does not need to carry a reservoir for the source to generate actuation pressure. SoFi is capable of agile swimming, integrated with on-board camera and can be remote-controlled by operators. We give also an example for wearable devices driven by HSAs. Polygerinos et al. (*26*) have developed soft exoskeleton for hand rehabilitation driven by hydraulic soft actuators (Figure 2.1C). We chose this example because the glove can achieve fully untethered operating by integrating all the auxiliary elements inside the waist which can be

worn by the user, including the water reservoir. Other soft robot and wearable devices driven by FEAs can be seen in the following references (*11–18*, *22–25*, *28*, *72*, *73*).FEAs can output higher force compared with other soft actuation technologies. FEAs are generally noisy due to the onboard pumps or compressors, which also make the miniaturization of the integrated system difficult.

2.2   Shape memory polymers

Shape memory polymers (SMP) are one type of polymer material which is capable to return from a deformed shape to its original shape through a stimulus (*31*). Most SMPs are thermally triggered. When the temperature is below the glass transition temperature T_g, the SMP is in its permanent state. When the SMP is heated above the T_g, the polymer switching segments behave like an elastomer. Once the switching segments are deformed by external force, the temperature needs to be cooled down to below its T_g to store the deformation by switching the segments into a crystalline phase. This step is called SMP programming. With the stored deformation, SMP stays in the temporary shape. When the temperature is increased above its T_g, the polymer returns to its permanent state. Using this "memory" process, SMPs have been developed as actuators. SMPs are generally slow and the output power density is small (*74*).

SMPs have been employed for developing soft robots. Using SMPs with different T_g can generate cyclic actuation triggered at different temperatures. Figure 2.1D shows an example representing the robots driven by SMPs. This example is chosen because it shows the possibility for making untethered soft robot driven by SMPs by controlling the environmental conditions. Two SMPs with different T_g (*30*) have been used to drive this soft robot. The swimming robot use SMPs to trigger bistable elements connected with the fins. With the fins moving between the bistable positions, the robot can swim forward and backward. Other robots driven by SMPs can be seen in the following references (*32*, *35*, *37*).

The controlling of SMPs in the chosen example, has been performed by controlling the environment temperature. Changing the environmental conditions is difficult for general cases. In addition, the robots should be capable to resist to the environment changes (including temperature), and keep performing the asked tasks. Therefore, the SMPs are not suitable for untethered operating in general cases.

2.3   Magnetically-driven soft actuators

Soft actuators controlled by magnetic field have also been reported (*50–55*), termed here magnetically-driven soft actuators (MSAs). MSAs are generally made by embedding ferromagnetic or permanent magnetic particles inside elastomer matrix (typically silicone rubber). Variation of magnetization needs to be predefined along the soft actuator, so that when external

magnetic field is applied, the soft material itself can deform to generate actuation. To apply the external driving magnetic field, either workspace covered by fixed coils in different directions (*51*, *55*), or permanent magnets can be employed (*50*, *52*, *53*).

Figure 2.1E gives an example of multi-legged soft robot (*50*). This example is chosen to represent the soft robots driven by MSAs, because it shows the capability of fast moving, and high carrying capacity for small size soft robot (2 cm body-length). The MSA used in this work consists of iron micro-particles embedded inside silicone elastomer. Before the curing of the silicone elastomer, external magnetic field is applied near the spin-coated flat mixture to form the magnetic peaks, which are the robot legs afterwards. Driven by programmable external magnetic field, both the robot legs and the robot body can bend to generate locomotion. The legged robot is directly driven by a variable magnetic field obtained through the displacement of a permanent magnet. Indirect control of the MSA has been reported using light (*53*). Other soft robots driven by MSAs can be seen in these references (*51*, *52*, *55*).

The MSAs are very promising to be used in closed environment covered by magnetic field. They show remote-driven of the magnetic materials by using programmable magnetic field. Therefore the MSAs are not connected with any wires. The totally soft actuators can be miniaturized with simple materials and simple fabrication processes. However, it is extremely challenging to integrate the MSAs with their auxiliary control systems (bulk system for generating magnetic field). From its operating principle, MSAs have to be remotely/externally driven. Therefore the MSAs are not suitable for making fully integrated independent autonomous devices.

2.4   Shape memory alloys

Shape memory alloys (SMAs) have also been developed to drive soft materials (*40–46*). SMAs mostly use nickel-titanium (NiTi) alloy (Nitinol), which can change its crystal structure in response to temperature stimuli. The lattice structure depends on the applied load and temperature on the SMA (*45*). At low temperature, the SMA is in the twinned Martensite phase. When applied load, the SMA is deformed and its lattice phase changes to deformed/detwinned Martensite phase. Through heating, the SMA changes to the austenite structure. During the cooling process, the SMA returns to the twinned Martensite structure for the next cycle. The step of heating generates the deformation, therefore the SMA can be used as actuator. For making actuation cycles, the SMA should be always reloaded to change the lattice phase from twinned to deformed Martensite structure. The SMAs are not intrinsically soft, but when combined with a soft matrix (typically silicone elastomer), they can be used to drive the SMA/elastomer hybrid system. SMAs are driven by the voltage-induced resistive heating. As they are metals and thus are quite good conductors, the driving voltages are very low (typically 2-7 volts), corresponding a current of 0.5- 4 A. As the actuation of SMAs is generated by heating and cooling process, their actuation speed are generally slow.

SMAs have been employed for making soft actuators to drive soft robots and wearable devices. Figure 2.1F presents a quadruped untethered soft robot (*40*) to represent the untethered soft robots driven by SMAs. This example is chosen because it improves the actuation speed for the SMAs. The soft robot is driven by four SMA actuators, each of them consisting of SMA wires embedded inside thermally conductive elastomer layers. This elastomer can improve the heat dissipation, therefore allowing faster (0.3 Hz) dynamic actuation than typical SMA actuators. The untethered SMA actuators can be powered with 3.7 V onboard Lithium Polymer battery. Other SMA driven robots can be seen here (*41*, *43–46*).

2.5   Electroactive polymers

The electroactive polymers focused here include Ionic polymer−metal composite (IPMC), and dielectric elastomer actuators (DEAs).

Ionic polymer−metal composite (IPMC) is another type of soft actuator used for driving soft robots (*56*, *60*, *63*, *64*). IPMC needs electrolyte to actuate, which contains cations and anions with different size or mobility. The principle for the actuation of IPMC is the movement of ions under electrostatic force between the electrodes (*60*). The movement of ions causes volume variations. IPMCs need low voltage to operate, typically less than 4V. Regarding to the speed of actuators, IPMCs are usually slow.

Soft robots driven by IPMCs have been reported (*56*, *63*, *64*). Figure 2.1G gives an example of an untethered crawling robot driven by IPMCs. The robot is powered by onboard integrated battery, and controlled with microcontroller. Due to the slow speed of IPMC actuators, the robot can only move with a speed of 0.4 mm/s.

Compared to IPMC actuators, DEAs can produce higher speeds, and larger strains. Versatile soft robots and wearable haptic devices driven by DEAs have been reported, which will be further discussed in detail in Chapter 3.

2.6   Concluding remarks on soft actuator review

Among all the soft actuation technologies, electrically driven actuators are particularly well suited for autonomous untethered operation, or for quiet on-body wearable applications, as they allow for ready integration with many sensors and control circuitry. The above mentioned electrically powered actuators include: SMA, IPMC, and DEA.

Zhang et al, (*74*) have compared the actuator performances in terms of their power density, bandwidth, strain, stress, linearity, and efficiency. The power density is the output work generated during actuation normalized to its mass and period. The bandwidth is the maximum operating frequency of the actuators. The strain is the change in length during actuation over

the initial length. The stress is the output force normalized to the cross-section area of the actuator. The linearity is the accuracy of using a linear model to predict the actuators performance. The efficiency is the ratio between the output and input power. Here, we adapt the comparison figures for the electrically driven soft actuators SMA, IPMC and DEA in Figure 2.2. The thermally actuating devices (SMA) offer high stress and power density. But they are slow and low efficient (Figure 2.2A). IPMC actuators output slow speed, low power density and stress, even though their operating voltage is low (Figure 2.2B).

DEAs present the best combination regarding all the above mentioned aspects, especially in view of high speed (*5*), high strain (*6*, *7*), and high efficiency (Figure 2.2C). DEAs have drawbacks such as low output stress, and need high operating voltage. Recent research activities offer solutions regarding to these problems. In the following chapter, the materials, fabrication methods and corresponding efforts to improve the DEA performances are discussed.
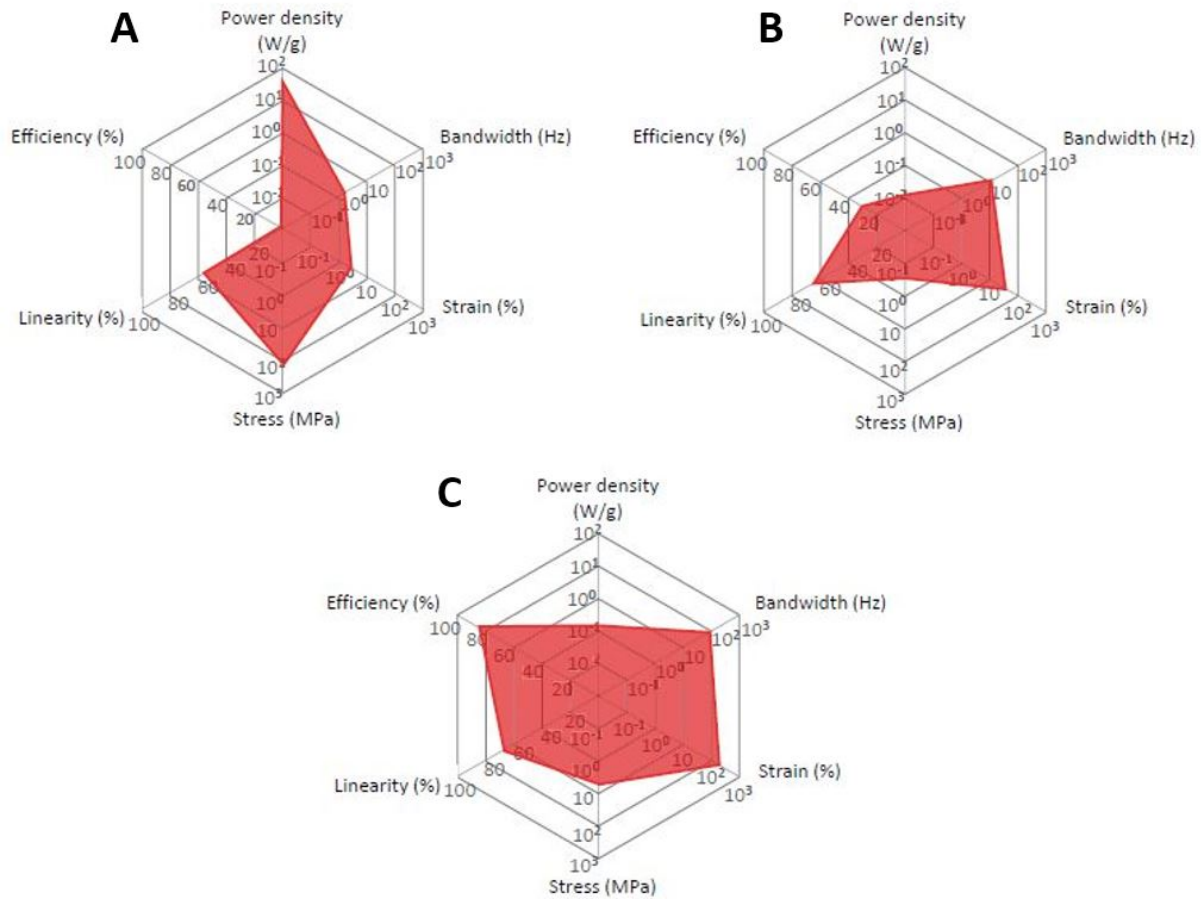
Figure 2.2 Comparison of electrically driven soft actuators. Adapted from (*74*). The comparison is based on overall related actuator performance in terms of their power density, bandwidth, strain, stress, linearity, and energy efficiency. The related figures correspond respectively to (A) SMA; (B) IPMC; (C) DEA.

Chapter 3 Dielectric Elastomer Actuators

3.1 Summary

Dielectric elastomer actuators (DEAs) are electrostatically driven soft actuators. DEAs can produce high operating speed (kHz) (*5*), large actuation strain (highest reported value of 1692% in area) (*7*) and high output force (10 N) (*57*, *75*). DEA-based applications have been demonstrated in many fields such as tunable optics (*5*, *76*, *77*), biological cell stretchers (*78–81*), transparent loud-speaker (*82*), soft robots (*83–111*) and wearable devices (*112–118*).

This Chapter focuses on DEA-based soft robotics and wearable applications. In these two fields, the high DEA driving voltage can especially limit the device practicality. DEA-based soft robots need to get rid of the tethering wires and move in larger space. The on-board integrated control elements need to be made light for agile movement, and tiny volume for miniaturization. For wearable devices, the high driving voltage needs to be decreased for safety and consumer acceptance. The entire integrated system should be miniaturized for practical on-body wearing to meet more use cases in daily-life.

Structure of this chapter:

First, the DEA fundamentals are reviewed as following:

- Working principle;

- Failure modes;

- Dielectric materials;

- Electrode materials and corresponding fabrication methods;

- DEA fabrication methods;

Then, the applications of using DEAs for soft robotics and wearables are reviewed.

Finally, the limitations of the DEAs and corresponding proposed improvements are discussed.

3.2   DEA working principle

DEAs consist of dielectric elastomer layers sandwiched by stretchable electrodes. (Figure 3.1) When the voltage (typically several kV) is applied between the electrodes, the elastomer membrane is squeezed in thickness due to the electrostatic force and therefore expands in area. An example of DEA with giant strain is given in Figure 3.2, with the photos corresponding to the DEA at rest and active states. With similar sandwich structure, applications as energy generators (*119–123*) and sensors (*124–127*) have also been reported.
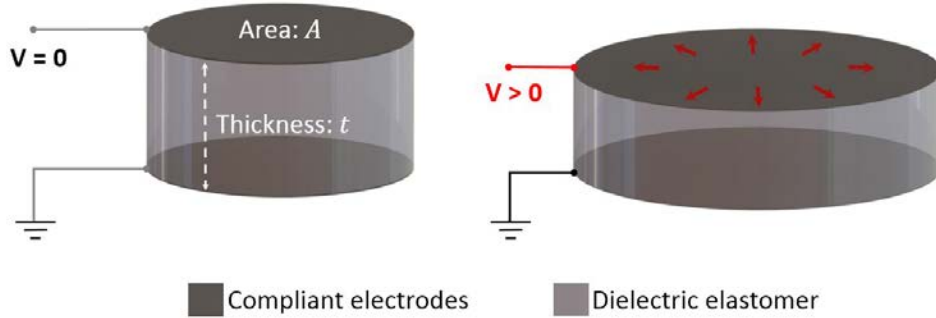
Figure 3.1 DEA working principle. DEAs consist of a dielectric elastomer membrane sandwiched by two compliant electrodes. When a voltage is applied between the two compliant electrodes, the dielectric elastomer is squeezed in thickness, therefore expands in area.
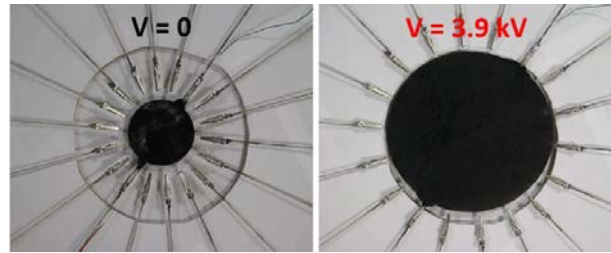
Figure 3.2 Photos of big strain DEA at rest and active states. Adapted from (*6*).

The theory for DEA actuation principle has been reported by Pelrine et al. (*128*) in the late 1990s. The structure of DEAs is similar to parallel plate capacitors, but their electrodes and dielectrics are compliant (Figure 3.1).

The DEA working principle is illustrated in the following section by estimating its thickness strain from the applied voltage. We assume that the DEA consists of ideal electrodes, which serve only to distribute electric charges and do not add stiffness on the elastomer. The dielectric elastomer (DE) in the DEA is assumed to be incompressible, which means the volume is constant (Poisson's ration equals to 0.5). We assume that A is the area of the DE and t its thickness (Figure 3.1), so due to the incompressibility:

$$A * t = \text{Constant} \quad \text{Eq. (3.1)}$$

When the voltage V is applied between the two electrodes of DEA, the energy U stored in the capacitor is:

$$U = \frac{1}{2} V^2 C \quad \text{Eq. (3.2)}$$

Where V is the voltage applied on the electrodes of the capacitor; C is the capacitance.

$$C = \frac{\varepsilon_0 \varepsilon_r A}{t} \quad \text{Eq. (3.3)}$$

Where ε_0 is the vacuum permittivity; ε_r is the relative dielectric constant.

Put Eq. (3.3) into Eq. (3.2):

$$U = \frac{\varepsilon_0 \varepsilon_r A V^2}{2\,t} \quad \text{Eq. (3.4)}$$

When the driving voltage V is applied, both A and t change due to the Maxwell pressure P. The change of electrical energy in the capacitor corresponds to the work done by P, therefore:

$$P A\,dt = dU = \frac{\partial U}{\partial t} dt + \frac{\partial U}{\partial A} dA \quad \text{Eq. (3.5)}$$

From Eq. (3.1)

$$\frac{\partial A}{A} = -\frac{\partial t}{t} \quad \text{Eq. (3.6)}$$

Put Eq. (3.6) into Eq. (3.5),

$$P A\,dt = dU = \frac{\partial U}{\partial t} dt + \frac{\partial U}{\partial A} * \frac{\partial A}{\partial t} dt = -\frac{\varepsilon_0 \varepsilon_r A V^2}{t^2} dt \quad \text{Eq. (3.7)}$$

So, the Maxwell pressure is:

$$P = -\frac{\varepsilon_0 \varepsilon_r V^2}{t^2} = -\varepsilon_0\,\varepsilon_r\,E^2 \quad \text{Eq. (3.8)}$$

Where E is the electric field.

The Maxwell stress squeezes the elastomer in thickness, and arrives at the balanced state when the mechanical stress in the elastomer equals the Maxwell stress. At this equilibrium state,

$$P = -\varepsilon_0\,\varepsilon_r\,E^2 = Y s_z \quad \text{Eq. (3.9)}$$

$$s_z = -\frac{\varepsilon_0 \varepsilon_r E^2}{Y} = -\frac{\varepsilon_0 \varepsilon_r V^2}{Y\,t^2} \quad \text{Eq. (3.10)}$$

where s_z is the strain in the thickness direction; Y is the Young's modulus of the dielectric elastomer;

For small strains, the final thickness t can be approximated to the initial thickness t_0, therefore:

$$s_z = -\frac{\varepsilon_0 \varepsilon_r V^2}{Y\,{t_0}^2} \quad \text{Eq. (3.11)}$$

For larger strain over 10%, the final thickness of the dielectric layer in the Eq. (3.10), is $t = t_0(1 + s_z)$. The thickness strain is then:

$$s_z = -\frac{2}{3} + \frac{1}{3}\{f(s_{z0}) + \frac{1}{f(s_{z0})}\} \quad \text{Eq. (3.12)}$$

where $f(s_{z0}) = \left[2 + 27\,s_{z0} + \frac{\{-4+(2+27s_{z0})^2\}^{\frac{1}{2}}}{2}\right]^{\frac{1}{3}}$, and $s_{z0} = -\frac{\varepsilon_0\varepsilon_r V^2}{Yt_0^2}$ (solution adapted from (*128*)).

Measuring the expansion strain is easier than measuring the thickness strain. From Eq. (3.1),

$$(1+s_x)\,(1+s_y)\,(1+s_z) = 1 \quad \text{Eq. (3.13)}$$

Where s_x and s_y are the lateral strains. For DEAs with the same lateral strain:

$$s_z = \frac{1}{(1+s_x)^2} - 1 \quad \text{Eq. (3.14)}$$

3.3 DEA failure modes

Dielectric breakdown

Dielectric breakdown (DB) (*129–131*) is the main failure mode for DEAs. DB happens when the applied electric field is higher than the dielectric strength of the dielectric material. Partial discharge happens through the dielectric elastomer, and chars a channel inside the dielectric elastomer and carbonize the channel. The carbonized channel conducts current across the gap between the two electrodes of the DEA, and causes irreversible damage of the DEA.

Electromechanical instability

At the DEA active state, the dielectric elastomer membrane achieve at the equilibrium state between the electrostatic force and the restoring stress on the elastomer (typically elastic stress of the elastomer). When the restoring stress cannot balance the electrostatic force, the thickness of the elastomer membrane will contract. This corresponds to the electromechanical instability (EMI) of the dielectric elastomers.

The EMI thins the elastomer and results in a high electric field which is often higher than the DB field of the dielectric elastomer, causing the DEA to breakdown.

EMI can be avoided by applying pre-stretch on the dielectric membrane (*132*, *133*). The pre-stretch can shift the onset point of the snap-through point caused by the EMI, therefore the dielectric elastomer gets dielectric breakdown before the EMI starts.

Other failure modes

The mechanical cracking of the dielectric elastomer can cause the DEA to fail, especially when the elastomer is pre-stretched. The crack initiate, and propagate, which breaks the elastomer. This corresponds to a common failure mode of elastomers.

The electrode detachment or cracking can cause the DEA to fail. Without electrodes, the charges cannot be distributed on the dielectric elastomer, which prevents the formation Maxwell pressure cross the elastomer. The cracking of electrode can stop the charging and discharging of the capacitor, which stops the DEA actuation.

The working environment can also cause the DEA to fail, such as the humidity (*134*) and ions presence in the DEA working environment (*79*), which may change the properties of the dielectric membrane (e.g. dielectric breakdown strength).

3.4   Dielectric elastomer materials

There are several types of dielectric elastomers (DE) reported for DEAs, including silicone elastomer (*135*, *136*), acrylic elastomer (*137*, *138*), polyurethane (*75*, *128*), isoprene (*128*), fluoroelastomer (*139*), ethylene propylene (*128*), polybutadiene (*128*), acrylonitrile butadiene rubber (NBR) (*140*), thermoplastics (*141*) and interpenetrating polymer networks (IPNs) (*142*, *143*). The mostly commonly used DE materials in reported works are silicone-based and acrylic-based elastomers.

Silicone elastomer membrane sheets with fixed thickness can be ordered directly from Wacker Chemie AG and from Parker Hannifin Corporation. Most silicone elastomers are fabricated by mixing two commercially available precursors, followed by a curing step (*144*). By using different membrane casting parameters, silicone elastomer membranes with different final thicknesses can be obtained.

Acrylic-based elastomers are mostly from commercially available VHB adhesive tapes (VHB4905). Therefore the thickness of the elastomer is pre-fixed. Recently, DEAs with desirable acrylic elastomers thickness have been reported by using spin-coating (*57*, *66*). VHB is extremely easy to use, because it is commercially available. In addition, its sticky property helps the electrodes deposition.

DEAs with VHB elastomers can generate huge area strain up to 1692% (*7*). However, as the VHB is highly viscoelastic, the related DEAs cannot achieve fast operation. With the viscous elastomer, the strain is difficult to be controlled. Compared with VHB-based devices, silicone elastomers show much lower viscoelasticity than VHB, which enables the DEA for fast operating with actuation frequency up to kHz (*5*). In addition, the performance of the silicone-based DEA is more reproducible. The lifetime of the device is also much more improved compared with VHB-based devices (millions of actuation cycles) (*145*).

Silicone-based dielectric materials have been used during this thesis work, regarding to their low viscoelasticity and high cyclic actuation performance.

3.5 Stretchable electrodes

The DEA electrodes serve to distribute electrical charges on the surface of the DE layer to generate required electric field for actuation. Therefore, they must be electrically conductive. For fast operation, the electrodes should be highly conductive to not limit the charging and discharging time by the RC time constant. To distribute the charges during the actuation, the electrodes should be stretchable. The mechanical properties play also an important role for the DEA performance. The electrode should not add significant stiffness to the DE for not limiting its actuation. Therefore the electrodes should be as thin and soft as possible for generating large strain.

In general, one material cannot be thin, soft, stretchable and highly conductive the same time. Indeed, conductive materials are usually stiff and not stretchable, and soft materials are generally not electrically conductive. In addition, the stretchable electrodes should be easy to pattern for the design of the DEAs.

The reported compliant electrodes used for DEAs include carbon-based electrodes, metal-based electrodes, stretchable ionic conductors, and electric conductive polymers. Carbon and metal based stretchable conductors are the most widely used DEAs electrode materials. In the following context, the materials, and fabrication methods of the DEA stretchable electrodes are reviewed.

Carbon-based electrodes

Carbon-based electrodes are the most widely used stretchable electrodes for DEAs (*146*, *147*). There are mainly three types of materials, carbon particles in viscous matrix (carbon black in grease/oil) (*148–152*), carbon particles in polymer matrix (carbon black/silicone composite) (*5*, *113*, *153–158*), and carbon particles (carbon black powder, graphite powder, carbon nanotubes) (*8*, *57*, *66*, *159–163*). The active conductive medium in all these materials are the carbon particles.

Figure 3.3 gives several examples of the DEAs with carbon-based electrodes. Loose carbon powder is difficult to handle due to its high sensitivity to static charges. This problem can be solved by dispersing carbon powders in a matrix.

An example of using grease as viscous matrix (carbon grease) is given in Figure 3.3A (*150*). Compared with carbon powder, carbon grease is much easier to handle, and is usually applied on the DE membrane by directly brushing. Inkjet printing has been reported for carbon black/oil electrode system (*152*). Carbon grease can remain conductive with large deformation. The disadvantage of carbon grease is the diffusion of the grease into the DE material, which gives the electrode lifetime issue (*146*). In addition, carbon grease is also suspected as one type of carcinogens.

Using a polymer elastomer matrix can avoid this diffusion problem. This corresponds to the second type of stretchable carbon-based electrode, with an example given in Figure 3.3B (*5*).

Carbon particles blended inside a curable polymer can be applied onto the DE membrane, and subsequently be cured to form conductive elastomer electrodes. The elastomer composite can be applied onto the DE membrane by spray (*157*), or by stamping (*5, 153*). By using the elastomer as matrix, the electrode performances are much more stable, enabling DEAs to perform millions of actuation cycles (*145*). However, as the matrix is elastomer-based, the electrode stiffness increases compared with carbon grease. The electrodes can thus stiffen the DE membrane especially when the DE membrane is made thin (*153*).

To avoid the stiffness caused by using a matrix, carbon particles have been used as electrode directly. As mentioned earlier, directly applying carbon particles is difficult due to their sensitivity to static charges. Therefore, different methods have been reported to apply carbon particles on the DE membrane.

Figure 3.3C shows a DEA array with patterned carbon black electrodes applied by stamping (*8*). The corresponding DE material is an adhesive acrylic elastomer. A silicone stamp is used for transferring the carbon black. Due to the adhesion difference on these two materials, the carbon black on the silicone stamp can be transferred onto the acrylic DE layer. This method is limited to adhesive DE materials.
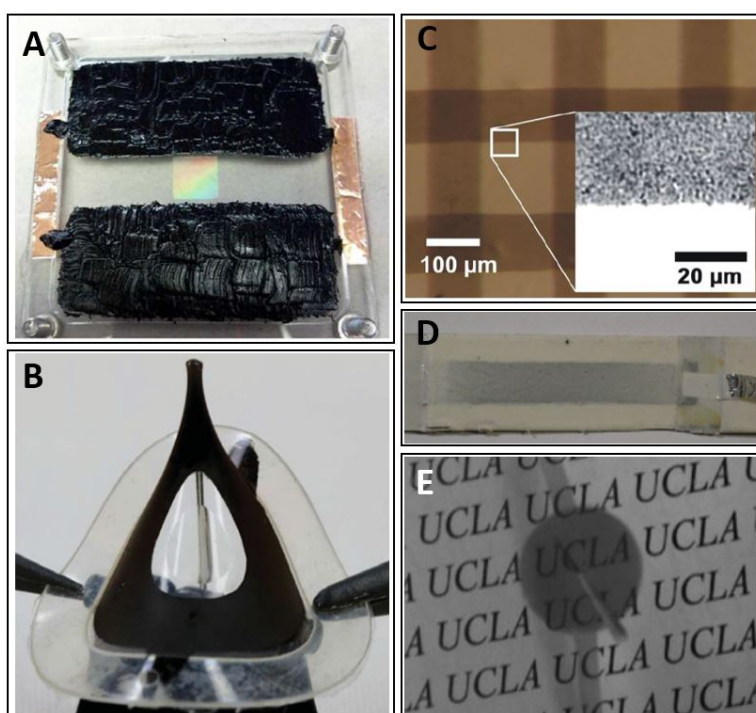
Figure 3.3 Examples of carbon-based electrode materials for DEAs. (A) DEAs with carbon grease electrodes (adapted from (*150*)). (B) DEA with carbon powder/silicone elastomer composite electrodes (adapted from (*5*)). (C) DEA with carbon black electrodes (adapted from (*8*)). (D) DEA with graphite powder electrodes (adapted from (*159*)). (E) DEA with carbon nanotube electrodes (adapted from (*162*)).

Figure 3.3D shows a multilayer stacked DEA with graphite powder electrodes (*159*), the graphite powder is applied on the silicone DE membrane by spraying a graphite solution at constant air pressure.

Figure 3.3E shows a DEA with carbon nanotube (CNT) electrodes (*162*). The electrode is deposited onto acrylic DE elastomer by spraying the CNT dispersed solution. These electrodes also present self-clearing property, which allows the DEA to operate close to the dielectric breakdown field with an increased lifetime.

Metal-based electrodes

Metal-based electrodes are the second most widely used electrodes for DEAs (*146, 147*). Metals are well known for their excellent electrical conductivity. However, metals are stiff and generally not intrinsically stretchable. Different approaches have been developed for using metals as DEA electrodes. Figure 3.4 gives several examples of using metal-based materials as DEA electrodes. One way to reduce the stiffness is to make extremely thin layers.
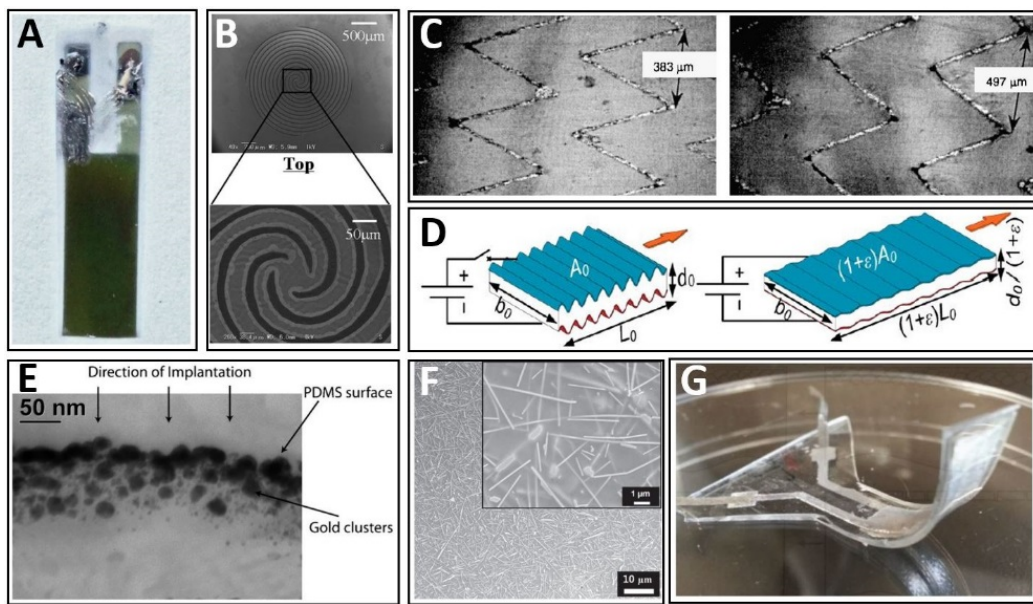
Figure 3.4 Examples of metal-based DEA electrodes. (A) Gold layer deposited by sputtering (adapted from (*164*)). (B) Patterned metal layer giving out-of-plane deformation (adapted from (*165*)). (C) Zig-zag patterned gold trace for adding the stretchability (adapted from (*139*)). (D) Corrugated pattern for adding the stretchability to thin metal layer (adapted from (*166*)). (E) Stretchable metal/elastomer composite electrodes obtained by metal ion implantation (adapted from (*167*)). (F) Silver nanowire stretchable electrode (adapted from (*168*)). (G) DEA with encapsulated liquid metal as electrodes (adapted from (*169*)).

Figure 3.4A reports a DEA with only 10 nm-thick gold electrodes deposited by sputtering (*164*). But the DEA strain is extremely tiny, which is due to the stiffness from the 10 nm-thick gold electrodes. To decrease the stiffness of metal layers, and add the stretchability, metal layers are patterned.

Figure 3.4B shows a patterned metal electrode deposited by electron beam evaporator and patterned with etching (*165*). With this spiral patterned metal electrode, the DEA gives out-of-plane deformation.

Figure 3.4C reports a DEA with zig-zag patterned gold electrodes by photolithography (*139*). The patterned electrodes remain conductive up to 80% strain. However, DEAs need the electrodes to distribute charges not only on the electrode trace, but on the whole active surface. A

second conductive electrode layer is therefore needed to cover the space in between the zig-zag gold traces.

Figure 3.4D presents a metal patterned method to avoid this problem (*166*). Instead of doing planar patterning, the gold layer electrode is processed to form an out-of-plane corrugated electrode. By depositing gold layer on pre-stretched DE membrane, the corrugated pattern is formed when the stretch is released.

The above mentioned methods thus apply special patterns on non-intrinsically stretchable materials to add them the stretchability. However, this process induces complexity in the DEA fabrication, and limits the DEA strain only in the designed direction.

Using metal particles embedded in polymer matrix can form intrinsically stretchable conductive composite (*167*, *170*, *171*). Figure 3.4E presents a metal/silicone composite stretchable conductor used as DEA electrodes fabricated with Metal ion implantation (*167*). The metal/silicone composite is fabricated by implanting metal particles into the elastomer matrix. The nanoclusters implanted inside the elastomer matrix move relatively to each other, and remain conductive even when the elastomer is stretched (*146*). The metal ion implantation process needs the formation of plasma (*167*, *170*) (*171*), which requires a complex setup and process. In addition, the implantation of metals inside the elastomer increases the Young's modulus of the composites (*170*).

Metal nanoparticles have also been used as stretchable electrodes (*115*, *117*, *168*). Figure 3.4F shows an example for stretchable metal-based DEA electrodes using silver nanowires (AgNWs) (*168*) embedded inside the DE layer by in-situ polymerization. Depending on the AgNW density, the AgNW electrode shows good transmittance of up to 80%.

Another class of metal-based electrode for DEAs is liquid metal alloy (*172*, *173*) with an example given in Figure 3.4G. The liquid form electrode is intrinsically compliant (*173*). Nevertheless, the liquid needs to be encapsulated to stay on the DE membrane surface. The encapsulation adds additional structures to the DEA, which increases DEA design complexity and impacts the DEA strain.

Other types of electrodes

In addition to the carbon and metal based electrodes, ionic conductors (*82*, *174*) have also been employed as DEA electrodes.

Ionic conductors include hydrogels and ionogels. For both hydrogels and ionogels, the conductivity is due to the mobile ions inside the gel, instead of the electrons for carbon and metal based conductors.

Ionic conductors can be highly transparent. An example of DEA with transparent hydrogel electrodes is show in Figure 3.5 (*174*). Adding transparency to the DEA can add additional functionalities to the devices. An example is show in Figure 3.5B, which use hydrogel electrodes to make a transparent loud speaker based on DEA (*82*).

For ionic conductors, their conductivity and mechanical properties are tunable by changing their chemical composition. For hydrogel, to keep the ions moveable, the gel must keep water inside. However, water can generally evaporate with time, which changes the hydrogel properties. For ionogels, they do not have this evaporation problem, as they are based on ionic liquid, which does not evaporate.

For DEAs with ionic electrodes, their lifetime is possible to be shortened. If the ions inside the electrodes migrate into the dielectric membranes under the applied high electric field, the DEA will lose its functionality.
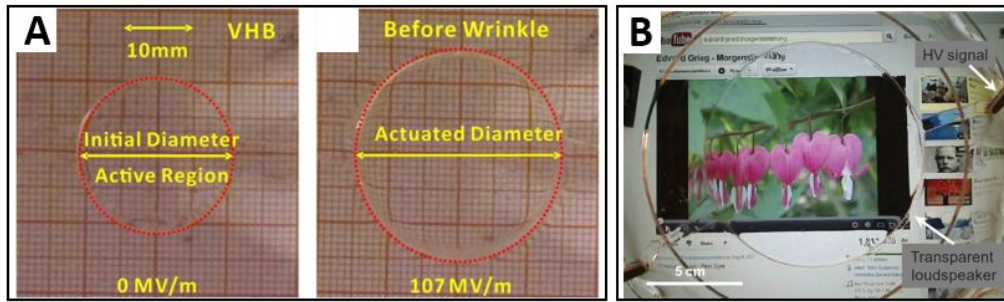
Figure 3.5 Ionic conductors as DEA stretchable electrodes. (A) Photos of DEA with hydrogel electrodes, at rest and active states (adapted from (*174*)); (B) Photo of a transparent loud speaker based on DEA with hydrogel electrodes (adapted from (*82*)).

Electronically conductive polymers (ECPs) (*175*, *176*) can also be used as DEA electrodes. ECPs generally need doping process to transform them into electrical conductors. Only few DEAs have been fabricated using ECPs as electrodes.

Concluding and remarks for stretchable electrodes

In the above section, the materials and corresponding fabrication methods are summarized regarding to the DEA stretchable electrodes. Most of the DEAs fabricated with these stretchable electrodes, need driving voltage above 600V. For the 200 nm-thick DEA with 10 nm-thick gold electrodes (*164*), a driving voltage of 12V has been used. However, the DEA generates extremely tiny actuation strain (from the reported bending radius at 12V, the corresponding estimated elongation strain is in the order of 10^{-4} %). The tiny elongation strain is limited by the stiff gold electrodes. For thin DEAs (below 5µm), the electrodes properties are more critical than for the thick ones (above 10 µm). The electrode stiffness is the determinant property for thin DEAs, because it will decide if the DEA can actually actuate. If the electrodes are much stiffer than the dielectric elastomer membrane, the DEA cannot generate acceptable actuation strain until dielectric breakdown. The stiffness of the electrode can be described by its thickness (t) and Young's modulus (Y). The product of these two parameters (Y*t) should be much less than the one of the dielectric material.

To select the suitable electrode materials for thin DEAs, in Table 3.1, the above summarized electrode materials are compared regarding their thickness and Young's modulus. We assume that a thin DEA is made by 1 µm-thick PDMS membrane with the corresponding listed electrodes. The PDMS layer gives a Young's modulus of 1 MPa, corresponding to a $Y_{PDMS}*t_{PDMS}$

value of 1 N/m. Therefore, to generate actuation, the Y*t value of the electrodes should be much less than 1 N/m.

Table 3.1 shows that the Y*t values of all the non-ionic electrodes are either bigger or comparable with the one of the PDMS membrane (1 N/m). For the micro-particles conductors, the related work did not give their corresponding Young's modulus. In spite of this, the particles-based materials are promising to be developed for low-voltage DEAs. One hypothesis can be made: these electrodes may not present significant stiffness due to the mobility of individual particles. Especially nanotube and nanowires are good candidate. Their high length/diameter ratio makes them promising. By depositing the conductive nanotubes on an elastomer substrate, one can make the following hypothesis: when the substrate is stretched, the nanotubes can slide against each other while remaining in contact, and thus remain conductive during stretching (*66*).

The ionic conductors are also promising candidates due to the extremely low Young's modulus. If the thickness of the reported hydrogel in Table 3.1 is decreased to 1 µm-thick, a Y*t value of only 0.002 N/m is possible to be obtained, which is promising regarding to the electrode stiffness.

Materials		Fabrication method	t (µm)	Y (MPa)	Y*t (N/m)
Carbon - based conductors	Carbon black/oil (*152*)	Inkjet printing	0.38	1.2	0.5
	Carbon/silicone (*177*)	Pad-printing	1 (estimated)	1 (estimated)	1
	Carbon black (*8*)	Stamp transfer	0.2	-	-
	Graphite Powder (*160*)	Spray	4.2	-	-
	CNTs (*66*)	Matte transfer	0.1 (estimated)	-	-
	CNTs (*163*)	Spray	0.1	-	-
Metal-based conductors	Gold (*164*)	Sputter	0.01	70000	700
	Gold clusters (*170*)	Metal ion implantation	0.018	1000	18
	AgNWs (*168*)	Drop casting	0.2	-	-
Hydrogel (*174*)		Molding	300	0.002	0.6

Table 3.1 Stiffness comparison of the reported DEA electrodes.

To conclude, the stretchable electrodes based on extremely soft ionic conductors are suitable candidates to be used for low-voltage thin DEAs. Non-ionic micro-particles are also promising

for making ultrathin (nm) stretchable electrode. In addition, these materials should be fabricated as thin as possible to present a low Y*t value.

3.6   DEA fabrication

From the DEA sandwich structure (Figure 3.1), a single layer DEA fabrication process consists of two basic steps: a) the preparation of the DE layer; b) applying of the compliant electrodes on the DE layer to form the sandwich structure. To achieve increased output force, single layer DEAs can be stacked to make a multilayer DEA. In the following part, the single layer DEA fabrication process is firstly described. Then the reported methods for fabricating stacked DEAs are reviewed.

Single layer DEA fabrication

DEAs generally need holders to support the soft structure. Depending on the holder shape, DEAs can generate different actuation motions including out-of-plane, bending, and in-plane expansion.

DE membrane can be fabricated using different technologies. Reported methods for DE membrane fabrication include blade-casting (*144*), pad-printing (*153*), inkjet printing (*178*), spray (*159*), spin-coating (*160*), and molecular beam evaporation (*164*). The DE membranes are generally constructed on a substrate covered with sacrificial layers, so that to get suspended DE membrane afterwards if necessary (*144*).

The fabrication methods for stretchable electrode include inkjet printing (*152*), spray coating (*157*), or stamping (*5, 153*) (see section 3.5). Electrodes should be patterned to achieve the desired DEA active area and for the electrical connections with voltage source.

One important step in the DEA fabrication is the pre-stretch step, which means stretching the DE membranes prior to applying the driving voltage. Pre-stretch can change the DE membrane properties including the mechanical loss tan δ (*179*), dielectric breakdown field (*180, 181*) , and electromechanical behavior (*132*). Suitable pre-stretch can help the dielectric elastomer to get rid of the "snap-through" process caused by the EMI. Pre-stretch can also take advantage of the EMI to get huge strain (*6, 7*) by tuning the dielectric breakdown to happen after the "snap-through" process. Directional pre-stretch can be used to define the DEA strain direction (*79*). During the construction of DEAs, the pre-stretch step can be performed either by stretching the suspended DE membrane before applying the electrodes, or by stretching the whole sandwich structure after the application of electrodes. The DEA holders can keep the constrain on the elastomer membranes resulted by pre-stretch.

For some special DE materials, pre-stretch is not necessary (*66*), which can simplify the DEA fabrication process. These DE materials present a rapid stiffening behavior above a certain stretch value, suppressing the onset of electromechanical instability.

To actuate the sandwich structure, voltage should be applied by connecting the electrodes with voltage source. Rosset et al, have reported the whole basic fabrication process for silicone-based single layer DEAs (*144*).

Until here, we summarize the necessary consideration for a single layer DEA fabrication process:

> ➢ Suitable construction methods for the DE and electrode layers;

> ➢ Electrode patterning;

> ➢ Pre-stretch of DE membrane;

> ➢ Holders;

> ➢ Electrode connection with voltage source;

The single layer DEA fabrication process serves as basic elements for making multilayer DEAs. Their fabrication process becomes more complicated compared with the single layer DEA. Additional processes should be performed, including: the electrode interlayer connection, the lamination of each layer, and the adhesion between each layer. The reported fabrication processes of stacked DEAs are summarized in the next section.

Review of stacked DEA fabrication process

Single layer DEAs may output low force due to the relatively thin dielectric layer. A stacked structure can improve the output force. Stacked DEAs present also much more robustness compared with single layer ones, by sustaining higher stretching force. Several approaches have been reported to construct the stacked structure. In the following context, multilayer DEAs are reviewed with their stacking methodologies, materials and construction methods. The performances of the related stacked DEAs are discussed regarding to the actuation voltage, output force and operation frequency.

The most direct way for making a stacked structure is to laminate individual single layer DEAs (*182*) as shown in Figure 3.6A. The single layer DEA uses carbon powder as electrodes and acrylic-based interpenetrating polymer networks (IPN) as DE layers (see section 3.4). The fabricated individual single layer DEAs have been laminated together. 400 layers have been stacked to make the multilayer DEA (Figure 3.6B), with a final dimension of 26 mm as height and 20 mm as diameter. With the stacked structure, the DEA is capable of lifting 2.6 kg weight with 18% contraction strain driven by 4 kV.

Another method to obtain stacked DEA from single layer DEAs is by folding (*154*). Figure 3.7A shows the folding principle. 1 mm-thick silicone-based dielectric membrane is coated with 0.5 mm-thick silicone/carbon black electrodes to make a single layer DEA strip. Different DEA shapes can be obtained by patterning the electrode strips. Then the patterned single layer DEA is folded to make a stacked structure in such a way that the electrodes in the opposite sides do not contact to each other to avoid short circuit. The folded stacked structure is then

encapsulated in a 0.1 mm-thick silicone membrane. Figure 3.7B gives the folded multilayer DEA. With a dimension of 85 mm-long (about 50 stacked DE layers), and a diameter of 25 mm, the stacked DEA can output 6 kPa axial stress (about 3N output force) with a driving voltage of about 10 kV.
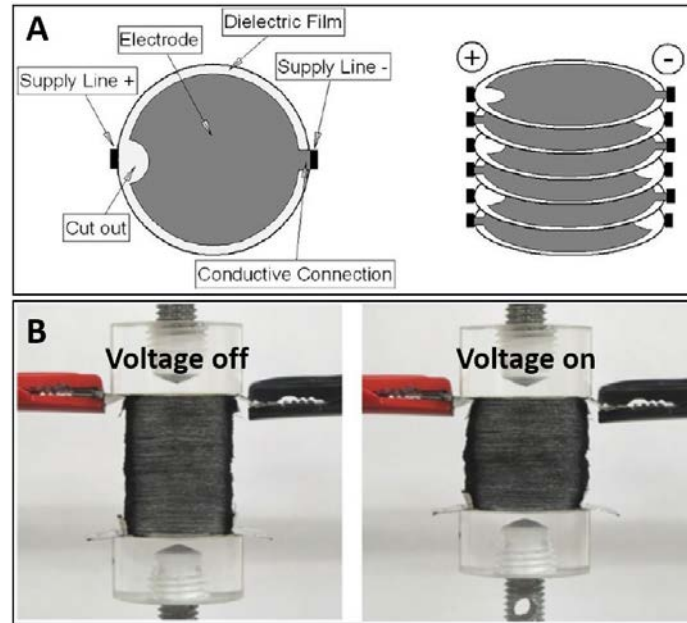
Figure 3.6 Fabrication of a multilayer DEA by single layer DEA lamination. Adapted from (*182*). (A) Stacking principle. (B) Photo of the stacked DEA at rest and active state.
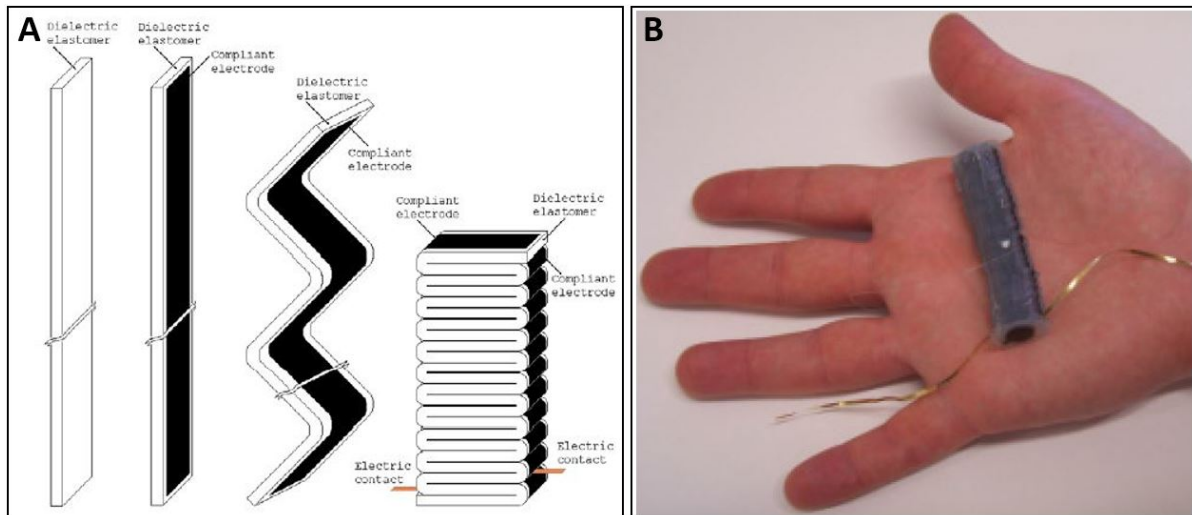
Figure 3.7 Multilayer DEA fabricated by folding a single layer DEA. Adapted from (*154*). (A) The folding principle. (B) A prototype of the folded multilayer DEA.

Stacked DEAs can also be obtained by firstly folding the single layer DEA into multilayer units, then laminating these multilayer units to increase the stacking number (Figure 3.8) (*75*, *158*, *183*).
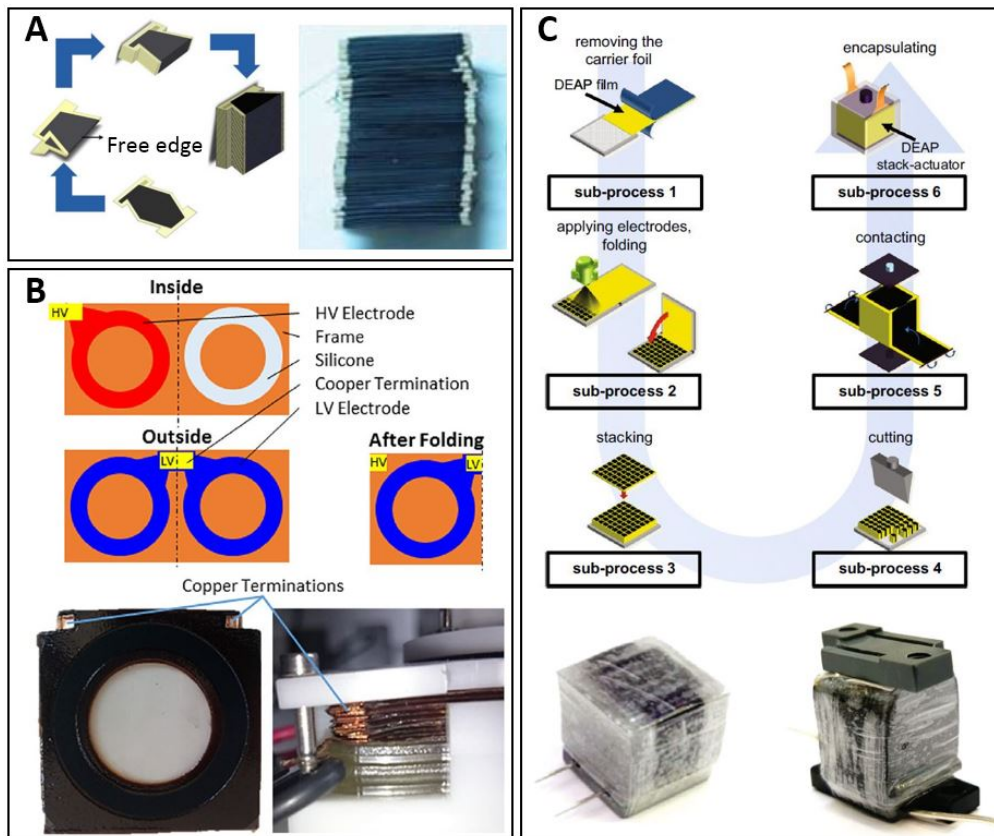
Figure 3.8 Stacked DEA obtained by laminating multilayer DEA obtained by folding. (A) Stacked DEA obtained by stacking bilayer DEA units folded from single layer DEA (adapted from (*158*)). (B) Using folding to fabricate bilayer DEA units directly from electrode and DE layers, then constructing the stacked DEA by laminating bilayer DEA units (adapted from (*183*)). (C) Automated multilayer DEA construction with roll-to-sheet process (adapted from (*75*)). Multilayer DEA units are firstly constructed by folding a two-layer structure of DE membrane with spray coated electrode. Then the multilayer DEA units are stacked.

Figure 3.8A shows a stacked DEA using acrylonitrile butadiene rubber (NBR) as dielectric materials, and carbon powder/NBR composite as compliant electrodes (*158*). Trapezoid shape can be obtained by folding a single layer DEA into a bilayer. The obtained bilayers are then stacked together to obtain a multilayer DEA with a height of about 6 cm. With 4 kV as driving voltage and 10 Hz as driving frequency, the stacked DEA can output 2% compression strain while carrying 2 kg weight.

Figure 3.8B shows a stacked DEA obtained by laminating bilayer DEAs fabricated directly by folding electrode and DE layers (*183*). The carbon black/silicone composite is firstly screen printed on a silicone film as the high voltage (HV) electrode. The other part of the silicone film is folded to cover the screen printed electrode to form a three-layer structure, with HV electrode sandwiched by silicone membranes. Then, two electrodes are screen printed as ground electrodes, and the three-layer structure is sandwiched by the two ground electrodes to form a bilayer DEA unit. By stacking the bilayer units, a multilayer DEA with a dimension of 86 mm x 86 mm x 25 mm is obtained. The multilayer cone DEA is used to trigger a bistable mechanical system. Using a structure combined with linear bias spring (LBS) and negative-rate bias spring (NBS), the system can lift a weight of 10 kg for 3 mm, with 2.5 kV as the DEA driving voltage to trigger the bistable system.

Figure 3.8C shows an multilayer DEA constructed by automated roll-to-sheet process (*75*). Multilayer DEA units are firstly constructed by folding a two layer structure of DE membrane with spray coated electrode. Then the folded multilayer DEA are cut into individual units and are further stacked to achieve more stacked layers. The stacked DEA prototype shown in Figure 3.8C consists of 200 layers with estimated dimension about 10 mm x 10 mm x 10 mm. It outputs 10 N tensile forces with a contraction strain of 3.5% under a driving voltage of about 2.5 kV.

The above mentioned approaches result in DEAs with much higher output force in the area expansion direction and more displacement in the thickness direction than single layer DEAs. During the stacking, these methods can lead to the overlapping of the top and bottom electrode layers in between the successive units, where actually one electrode layer is necessary to distribute the electrical charges in between the successive units. Alternative deposition of electrode layers and DE layers can avoid the unnecessary electrode overlapping. The corresponding multilayer construction methods are reviewed in Figure 3.9.

Figure 3.9A shows the multilayer structure of the stacked DEA constructed using alternatively electrode layer and DE layer deposition (*159*). No electrode overlapping occurs in this stacked structure.

Figure 3.9B reports stacked DEA strip, constructed using spray deposition for both the graphite-based electrodes and the silicone-based DE materials (*159*). Single spray path can give an inhomogeneous layer, of which the thickness profile follows a Gaussian distribution. Using multi-spray with offsets of the airbrush can balance the variation of each spray path. The fabricated DEA with 4 active layers can output 3.4% contraction strain, with a driving voltage of 4 kV.

Figure 3.9C presents a 5-layer stacked DEA fabricated with silicone-based DE membrane obtained with blade casting, and AgNW-based electrode applied with spray-coating (*115*). With 3 kV and 1Hz driving signal, the 5-layer stacked DEA outputs about 0.3 mm out-of-plane displacement and about 10 mN output force. Both the displacement and output force decrease with the driving frequency increase. But at the resonance frequency of 191 Hz, the output force is amplified to 55 mN by resonance.

Figure 3.9D presents a 12-layer stacked DEA based on spin-coated silicone elastomer as DE layers and carbon-based electrodes (*84*). The stacked DEA generates out-of-plane deformation. With 2.5 kV DC driving voltage, the stacked DEA can output a displacement of 0.55 mm, and a force of 16 mN. With 2.5 kV AC signal, the stacked DEA can produce similar performance as with DC signals until 100 Hz.

Figure 3.9E shows a multilayer DEA array which can generate bending motion (*66*). The stacked structure is constructed with spin-coated acrylic-based DE layers and CNT-based electrode applied by matte transferring. Unimorph based on 12-layer stacked DEA with a dimension of 5mm x 20mm x 0.5mm, has been characterized in the work. With 4kV driving voltage,

the unimorph can output block force of 11 mN, with a tip displacement of 12.6 mm and frequency bandwidth of 30 Hz.
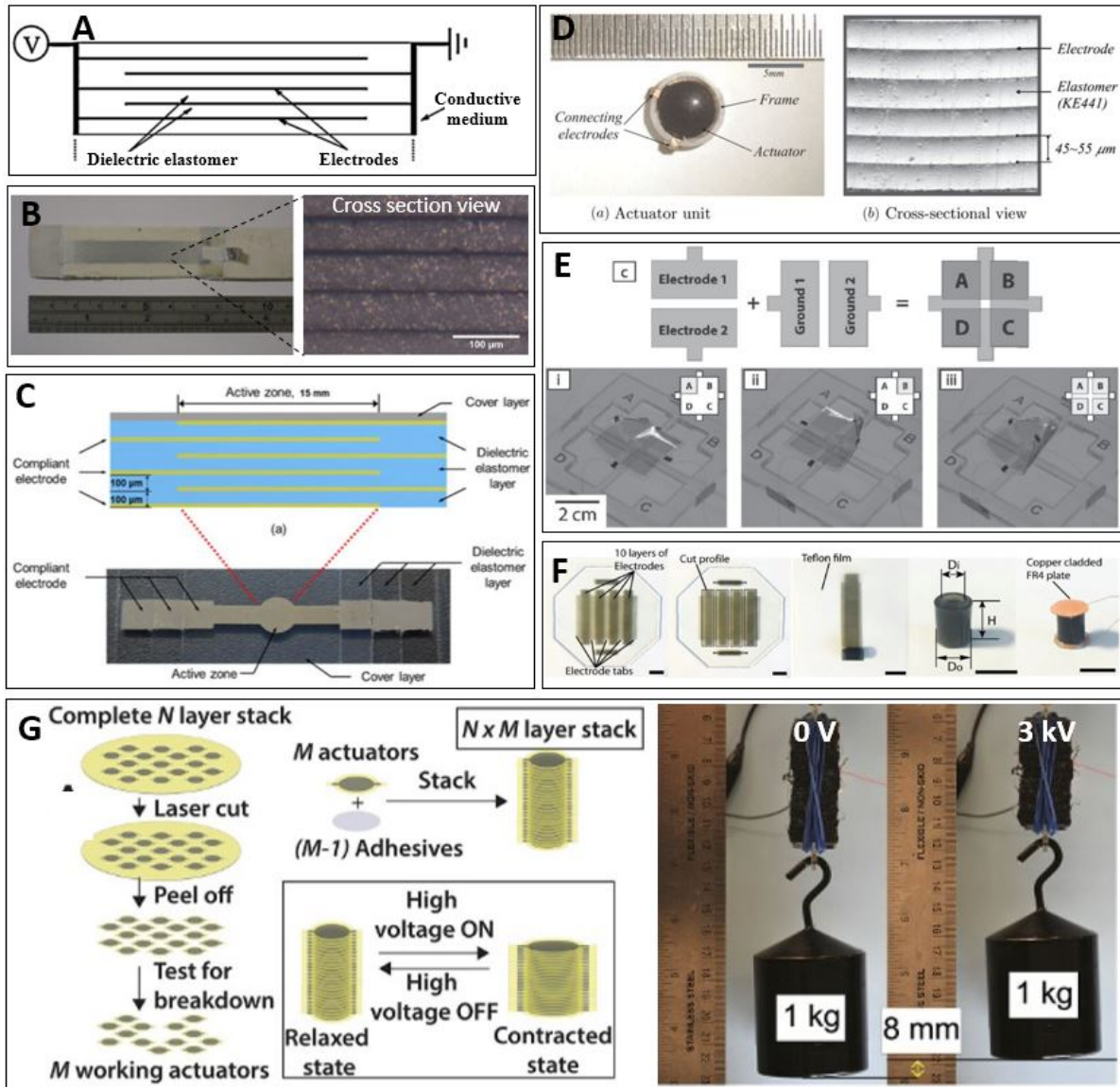
Figure 3.9 Multilayer DEA constructed by alternative deposition of electrode and DE layers. (A) Multilayer profile structure (adapted from (*159*)). (B-E) Examples of fabricated multilayer DEAs (B is adapted from (*159*), C is adapted from (*115*)); D is adapted from (*84*)); E is adapted from (*66*)). (F) Multilayer DEA with firstly alternative electrode and DE layer deposition, then rolled up as a cylinder actuator (adapted from (*184*)). (G) Stacked DEA consisting of 1170 layers (adapted from (*57*)).

Figure 3.9F shows a stacked DEA fabricated with a similar process as in Figure 3.9E, but with an additional rolling up step after the multilayer is constructed (*184*). Silicone-based DE layers have been used in this work, and CNT-based electrodes have been applied using matte transferring. With 1 kV driving voltage, the rolled stacked DEA can output 0.8 mm displacement, and 600 mN output force. Using silicone-based DE materials, the stacked DEA is capable to operate over 100 Hz.

Figure 3.9G shows a method for making multilayer DEAs with more than 1000 stacked layers (*57*). This process combines the two methods mentioned above. First, multilayer DEA units

have been fabricated by alternative deposition of electrode layers with CNT matte transferring, and DE layers by spin-coating acrylic-based elastomer (as show in Figure 3.9E). Second, the individually fabricated multilayer DEA units have been stacked (as shown in Figure 3.6 with stacked DEA units instead of single layer DEAs). With a driving voltage of 3 kV, the fabricated stacked DEA (1170 layers) can lift a 1 kg weight for 8 mm.
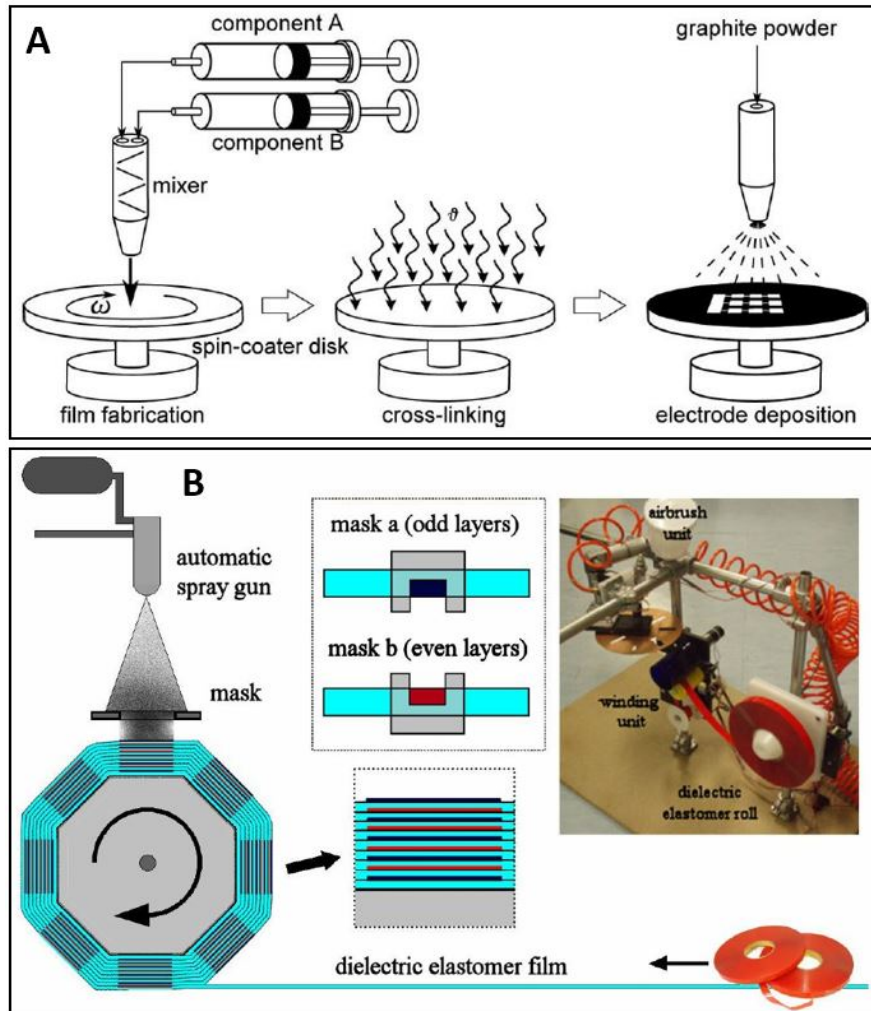
Figure 3.10 Automated multilayer DEA fabrication process. (A) Example of automated fabrication using alternatively spray deposition for electrode layers and spin-coating deposition for DE layers (adapted from (*160*)). (B) Demi-automated system for multilayer DEA fabrication using commercial VHB tape and spray coating for electrodes deposition (adapted from (*185*)).

The displacement of stacked DEAs in the thickness direction increases with the stacking number. To achieve high stacking number, automated process are necessary to increase the working efficiency. Automated multilayer fabrication processes for the alternative electrode layer and DE layer deposition have been reported. Two examples are given in Figure 3.10.

Figure 3.10A shows an automated multilayer construction process by spin-coating the DE materials and spray of the graphite powder electrodes (*160*). Stacked DEAs consisting of 50 thin (20-μm thick) silicone elastomer membranes have been developed with this automated process. The stacked DEAs operate with 600V driving voltage, and can achieve fast actuation of 125

Hz. This work presents the stacked DEAs with lowest driving voltage among all the reported multilayer devices. However, the strain of this device is small, with an estimated thickness strain of ~6%, which corresponds to linear expanding strain of ~3% in the area direction. The driving voltage and corresponding output strain are promising to be further increased by using thinner electrode layers for the stacked DEA.

Figure 3.10B shows a multilayer fabrication process using roll-to-roll process (*185*). Commercial DE membrane rolls have been used (VHB tape). The electrode is deposited by spraying carbon black/elastomer solution directly on the VHB tape without applying pre-stretch. The process shows an efficient way for making stacked DEAs by commercially DE membrane rolls.

Concluding and remarks for DEA fabrication process

We have summarized the DEA fabrication methods regarding to stacking methodologies, materials and construction methods. Compared with single layer DEA, multilayer DEAs can output bigger displacement in the stacking direction, and output higher force in the expanding direction. But the fabrication process of stacked DEAs is much more complex. Especially for the case of low-voltage thin DEAs, multilayer structure should be used to improve the DEA global characteristics and reinforce the robustness of the devices. No stacked DEAs with driving voltage below 500V has been reported to date.

Stacking method	Electrode materials and fabrication method	t_e	t_{DE}	Driving voltage	Ref
Stacking of single layer DEAs	Carbon-black applied on acrylic DE membrane by coating	Several hundred nm	~80 μm	4.2 kV	(*182*)
Folding single layer DEA	Carbon-black/silicone electrode coated on DE membrane	0.5 - 0.8 mm	1 mm	10 kV	(*154*)
Alternative electrode and DE layer deposition	SWCNT applied on acrylic DE layers by matte transferring	Less than 100 nm	25 μm	1-2 kV	(*66*)
	Graphite powder applied on silicone DE layer by spray	4.2 μm	20 μm	600 V	(*160*)

Table 3.2 Comparison of reported multilayer construction method regarding to the suitability for low-voltage stacked DEA with driving voltage below 500 V.

For making low-voltage stacked DEAs, dielectric elastomers should be made thin and with high quality. When the dielectric membrane is made thinner, the corresponding driving voltage becomes lower (Eq. 3.11). When the thickness of the dielectric membrane decreased, the membrane quality should be guaranteed. Indeed, membrane defects will give unpredictable dielectric breakdown voltage for the thin membrane. The stretchable electrodes used for stacked DEAs also play an important role in the DEA performance. The electrodes should be made as thin and soft as possible to avoid the stiffening effect of the electrodes on the DE membrane. In addition, the electrodes should present low roughness. In a stacked DEA structure, not only the DE membranes are sandwiched by the electrodes, but also the electrodes are sandwiched by the DE membranes. Rough electrodes present the risk of resulting unpredictable dielectric breakdown voltage due to the uncertain thickness at the rough electrode area.

To investigate the suitability for the fabrication of stacked DEAs with driving voltage below 500V, the previously reviewed stacking methods are compared in Table 3.2, regarding to the electrode fabrication method, multilayer construction method, DE membrane thickness (t_{DE}), electrode thickness (t_e) and the operating voltage of the stacked DEAs.

From Table 3.2, we can conclude that the alternative electrode and DE layer deposition method can produce stacked DEAs with lower operating voltage than other stacking methods. However, the lowest operating voltage for the stacked DEA is still above 600 V. The voltage is limited by the thickness of both the dielectric elastomer layers and the electrode layers.

In conclusion, the reported stacking method did not produce reliable stacked DEAs with driving voltage below 500 V. Fabrication process which combines thin dielectric elastomer membranes (several µm-thick) with thin (nm) electrodes should be developed to achieve sub-500V operating stacked DEAs.

3.7   DEA-based soft robots

Robotic applications are focused in this part due to the promising advantage of using DEAs as robot muscles. Robots need to be capable of fast motion, which requires fast and powerful muscles. Robot can be miniaturized to meet small-scale (cm or less) functionality. Soft robots need to be able to remain functional even when being deformed/stretched due to the environmental conditions. With all the above listed requirements from the robotic field, DEAs meet all the needs by being fast (kHz actuation) (*5*), capable of generate high force density (3.12 10^6 N/m^3) (*182*), capable of miniaturization (*8*), and intrinsically soft.

DEA driven soft robots operating on-land, underwater and in the air have been widely developed. On-land operating robots include, crawling(*84–93*, *95*), rolling (*97*, *100*, *101*) and hopping robots (*94*, *96*). Underwater robots include swimming robots (*102–104*, *107*) and floating robots (*104*, *105*). To operate in the air, floating robots have been reported (*106*, *111*). Flapping wings have been designed (*148*, *186*), but not yet a system powered by DEA has shown a lift-off. DEAs have also been developed to drive soft motors (*98*, *99*) and grippers (*108–110*).

In the following section, DEA-based soft robots are reviewed by classifying them into three categories based on the medium in or on which they move: on-land, underwater, and in the air.

Crawling robots

Figure 3.11 gives examples of on-land crawling robots driven by DEAs. These examples are chosen as each of them shows a different DEA configuration to generate the corresponding robot motion. These actuation configurations include: rolled DEAs for extension, rolled DEAs for bending, stacked DEAs for extension in the stacking direction, DEA with out-of-plane actuation, flat DEA for bending, and DEAs with dielectric elastomer minimum energy structure (DEMES).
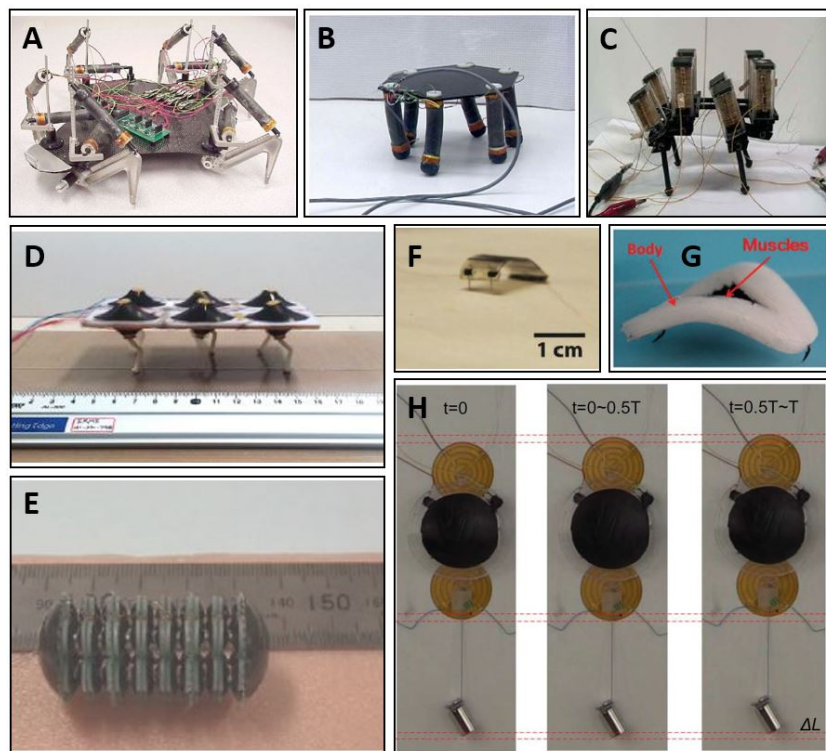
Figure 3.11 Examples of crawling robots driven by DEAs. (A) Robot with legs driven by rolled DEAs (adapted from (*92*)). (B) MERbot with legs driven by 2 DOF DEAs and mimicking animal walking gait (adapted from (*91*)). (C) Robot with legs driven by stacked DEAs (adapted from (*93*)). (D) Robot with legs driven by out-of-plane cone DEAs (adapted from (*88*)). (E) Annelid robot mimicking inchworm motion driven by DEA arrays with out-of-plane deformation (adapted from (*84*)). (F) Bending multilayer DEA driven robot with deformable body and rigid legs (adapted from (*89*)). (G) Robot with body driven by DEMES formed DEA and rigid directional legs (adapted from (*87*)). (H) Robot with body driven by bending DEA with DEMES, and legs with controlled electroadhesion for generating friction force for moving (adapted from (*85*)).

The earliest DEA driven robot that can be found in literature has been built in the early 2000s. The robots have been designed by using rolled DEA as robot leg muscle. Figure 3.11A gives an example of these robots driven by rolled DEAs which can generate extension/contraction motion (*92*). The robot can generate locomotion with a moving speed of 35 mm/s.

Segmented rolled DEAs have been used for generating bending motion, with 2 degrees of freedom (DOF) (*91*). One corresponding example is given in Figure 3.11B. A robot named MERbot with a dimension of 18cm x18cm x 10cm has been build using 6 bending DEAs with

2DOF. MERbot can walk by mimicking the gait of walking animals with a speed of 13 cm/s using a driving signal of 5.5 kV at 7 Hz.

Figure 3.11C shows a quadruped robot use stacked DEAs as leg muscle, which generate extension and contraction in the stacking direction. The robot is with a dimension of 19.1cm x 10cm x 11.5cm (*93*). By operating the two stacked DEAs (at 5 kV) with a phase difference, the robot can form walking gait.

DEAs with out-of-plane motion have been used as the robot leg muscle. Figure 3.11D presents a hexapod robot with a dimension of 15cm x 10.6cm x 4.8cm (*88*). By using two DEAs arrays to make an out-of-plane cone system, the robot leg can move with 3DOF. With 2 Hz at 3.5 kV as driving signal, the robot leg can generate walking gait and move with a maximum speed of 30 mm/s.

Instead of using out-of-plane DEA for driving legs, they can also be used to drive the robot body to generate locomotion. Figure 3.11E shows a 2 cm-long annelid robot powered by deformable body consisting of 8 DEA modules (*84*). Each module consists of 12 stacked DEAs to output out-of-plane motion. By operating the robot front and rear sectors sequentially with driving signal of 5 Hz at 2.2 kV, the robot can move with a speed of 1 mm/s by mimicking inchworms.

Bending DEAs have been employed to deform the robot body to generate gait. These robots need directional friction to move. Figure 3.11F presents a crawling robot driven by multilayer bending DEA (*89*). Without using pre-stretch for the DEAs fabrication, the robot body is flat at rest. When voltage is applied, the robot bends its body. The unidirectional bending of the DEA is achieved by using fiber stiffening. With directional rigid legs, the 2 cm-long robot can give a maximum speed of 20 mm/s, with driving signal of 3kV and 10 Hz.

DEAs with the dielectric elastomer minimum energy structure (DEMES) (*109*) have been used to drive robots. The DEMES consists of fixing pre-stretched DE membrane onto flexible substrate. An equilibrium state can be achieved when the constraint for holding the pre-stretched DE membrane is released. When the driving voltage is applied on the DE membrane, the structure achieves another equilibrium state between the DE and the frame. Figure 3.11G shows a robot with bended body formed by the DEMES structure (*87*). Two DEAs muscles are fixed on a silicone frame of 4 cm-length. With driving signal of 9 kV at 16 Hz, the robot can achieve a maximum moving speed of 16.1 cm/s. By controlling 2 different muscle parts, the robot can make turns with a minimum turning radius of 160 mm.

Instead of using patterned shapes to generate directional friction force, electroadhesive force has been employed to create the friction change. Figure 3.11H shows a robot of 8.5 cm length (*85*). This robot is also driven by DEA with DEMES. This example is chosen due to the use of electroadhesion to generate the leg friction, therefore the robot can move both forward and backward. The reported robot module can output maximum speed of 88.5 mm/s with 6 kV and 23 Hz as the DEA driving signal. Due to the strong electroadhesion force, the robot can climb

vertical wood wall while carrying 10 g payload. By combining two of the robot modules, the robot can also achieve turning.

Rolling robots

Rolling is another on-land robot motion. Examples of reported rolling robots are given in Figure 3.12, based on the different DEA configurations, including DEA planar expansion, DEAs with dielectric elastomer minimum energy structure (DEMES) and DEA with out-of-plane motion.
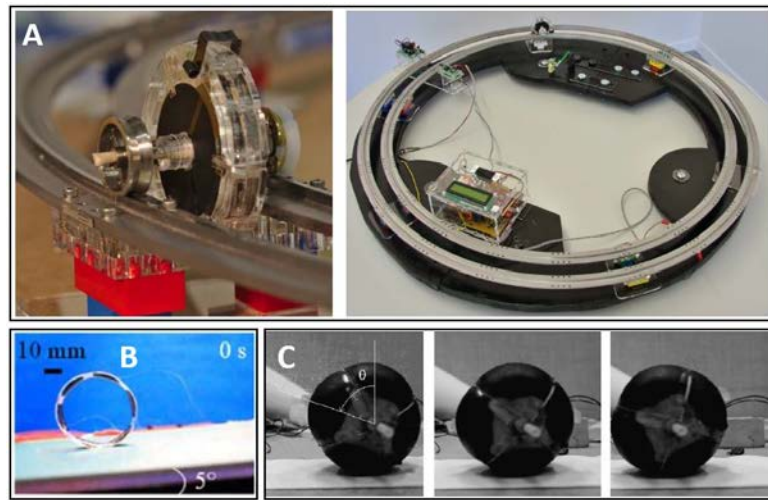
Figure 3.12 Examples of rolling robot. (A) Rupert rolling robot driven by planar DEA segments, which tips the outer frame to give rolling motion (adapted from (*97*)). (B) Rolling robot based on annular segment DEA with DEMES. DEA segments deform the annular shape into oval, tipping it to roll (adapted from (*100*)). (C) Spherical inflated chamber driven by segment DEAs. The DEAS change the sphere shape during actuation, which displaces its gravity center to make it roll (adapted from (*101*)).

Driven by in plane expansion DEA array, a rolling robot termed Rupert (*97*) is show in Figure 3.12A . With the central rolling axis staying on its track, the DEAs array actuates in sequence to displace the circular frame, tipping the robot and making it roll. Depending on the driving voltage, Rupert can output maximum speed of 20 cm/s. Based on the same principle, rotating motors have been developed (*97–99*).

Figure 3.12B presents a rolling robot based on a multi-segment annular DEA with DEMES (*100*). By actuating the 6 segments with programmed orders, the roller can change its shape from circular to oval, which tips the robot for rolling. With 3 kV driving voltage, the robot moves with an average speed of 36.25 mm/s.

Figure 3.12C presents a rolling robot driven by segmented out-of-plane DEAs. The out-of-plane motion is achieved by inflating air into a spherical closed chamber (*101*). In this case, the DEAs can change the sphere shape, which displaces its center of gravity and tips the sphere to roll.

Other on-land moving robots driven by DEAs have been reported, including hopping robot driven by DEA out-of-plane motion (*94*); robot driven by DEAs vibration (*187*).

Swimming robots

Swimming fish controls the buoyancy and uses the hydrodynamic to move vertically in water, and the propulsion generated by its body undulation to move forward (*188*). Swimming robots have been developed based on these principles. Figure 3.13 gives selected examples for swimming robot with the two above mentioned swimming principle. The corresponding DEAs can either be used to generate body undulation or buoyancy difference to drive the underwater robot.
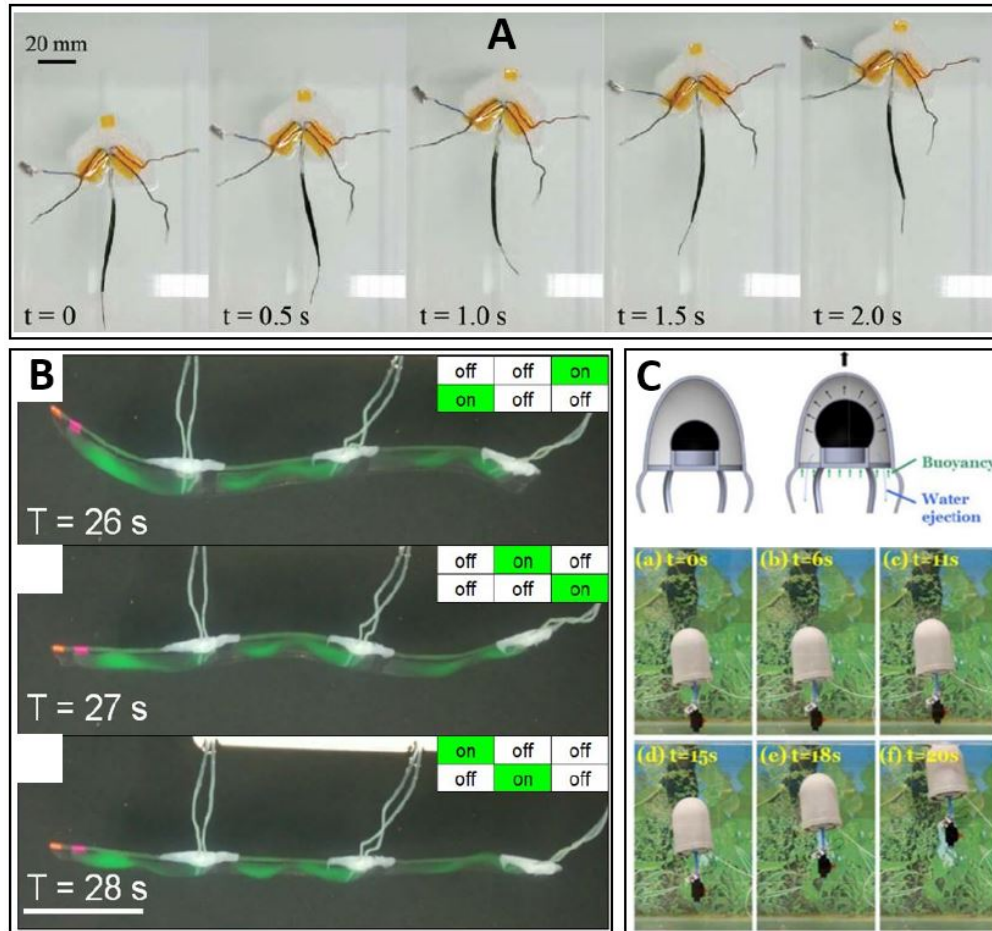
Figure 3.13 Examples of swimming robots driven by DEAs. (A) Swimming fish moves underwater by propulsion generated by body undulation (adapted from (*102*)). (B) Transparent swimming fish driven by DEA segments with water as electrodes (adapted from (*103*)). (C) Robot moving vertically by changing its buoyancy, using inflated DEA chamber to change the volume (adapted from (*104*)).

Bending DEAs have been used to generate undulation for swimming. Figure 3.13A shows a swimming fish with body length of 15 cm, which mimics the fish body undulation for generating propulsion (*102*). The fish is driven by two bending DEA at the two sides of its body. When one side DEA is active, the robot fish bends its body, generating waveform with the caudal fin due to the recoil force. The fish body undulation is generated by DEA sequential actuation, which outputs thrust to push the fish moving forward. The robotic fish gives a swimming speed of 37 mm/s with the driving signal of 5kV at 0.75 Hz. Figure 3.13B shows another swimming fish driven by DEA induced body undulation (*103*). This example is chosen as the

entire swimming robot does not have any hard frame. Therefore the robot is totally soft. The robot body is 22 cm-long. It is driven by 6 transparent DEAs, with water as liquid electrodes encapsulated by VHB tapes, which also serve as DE membranes. With 0.33 Hz at 7.5 kV as driving signal, the robot swims with a speed of 1.9 mm/s.

Driven by an out-of-plane DEA chamber, Figure 3.13C shows a robot which can achieve vertical movement in water (*104*). By actuating the DEA, the inflated DEA chamber changes its volume, therefore the buoyancy changes, which enables the robot to move up and down. Similar principle can be used to make robots moving vertically in the air using lighter gas (*111*).

The robots driven by DEAs operating on-land and underwater have been mentioned above. The DEA driving robots operating in the air, are much less compared with the above mentioned ones. Reported work used similar principle as underwater robots taking advantage of buoyancy by air (*106*, *111*). Robots mimicking the flying creatures using flapping wings have been reported based on piezoelectric actuators (*189*). However no flying robot with flapping wings powered by DEAs has been reported until today, even though DEA driving flapping wings (*148*, *186*) have been reported.

3.8   DEA-based wearable devices

Being intrinsically soft actuators, DEAs are capable to adapt to different shapes. DEAs are also lightweight. The two properties meet the need for on-body actuation. Therefore DEA-based wearable devices have been developed, including soft exoskeletons (*112*) and wearable tactile displays (*113–117*). Examples are given in Figure 3.14. These examples are given based on the different DEA actuation configurations used in the each case. The DEAs configurations used in wearable devices include: stacked DEA for extension and contraction; planar DEA for expansion; and DEA with out-of-plane motion.

Figure 3.14A shows a hand rehabilitation splint driven by stacked DEAs (*112*). The stacked DEA is connected to the finger by wires via a pulley. By actuating the stacked DEAs at 6kV, it can extend and contract by 8 mm to pull up and put down the finger.

Figure 3.14B shows a tactile display outputting shear force driven by a planar DEA array (*116*). Rigid pins with fixed spherical joints are employed in this work to transfer the deformation from DEAs to fingertip. One side of the pin is situated beside the planar DEAs, while the other side is in contact with finger skin. When the DEAs actuate, the pins in contact with skin move to give the user feedback. By applying 2.75 kV, one pin can output 39 mN blocking force.

DEA out-of-plane actuation can be used to generate feedback signals for haptic devices. The out-of-plane motion can be achieved in different ways, among which three different methods are given respectively in Figure 3.14 C, D and E.

Figure 3.14C shows a transparent haptic interface driven by electrostatic force with principle similar to a DEA (*117*). The haptic pattern is generated from the DEA out-of-plane actuation.

The device uses AgNWs as stretchable electrode and a non stretchable graphene electrode. The DE membrane is molded with void region as shown in Figure 3.14C. When applied voltage. the 3D pattern of the DE layer induces a 3D haptic pattern that can be felt by the user. When no voltage is applied, the DE membrane remains flat. From the user test, the users can feel the rough surface with 3D pattern when 5 kV driving voltage is applied.
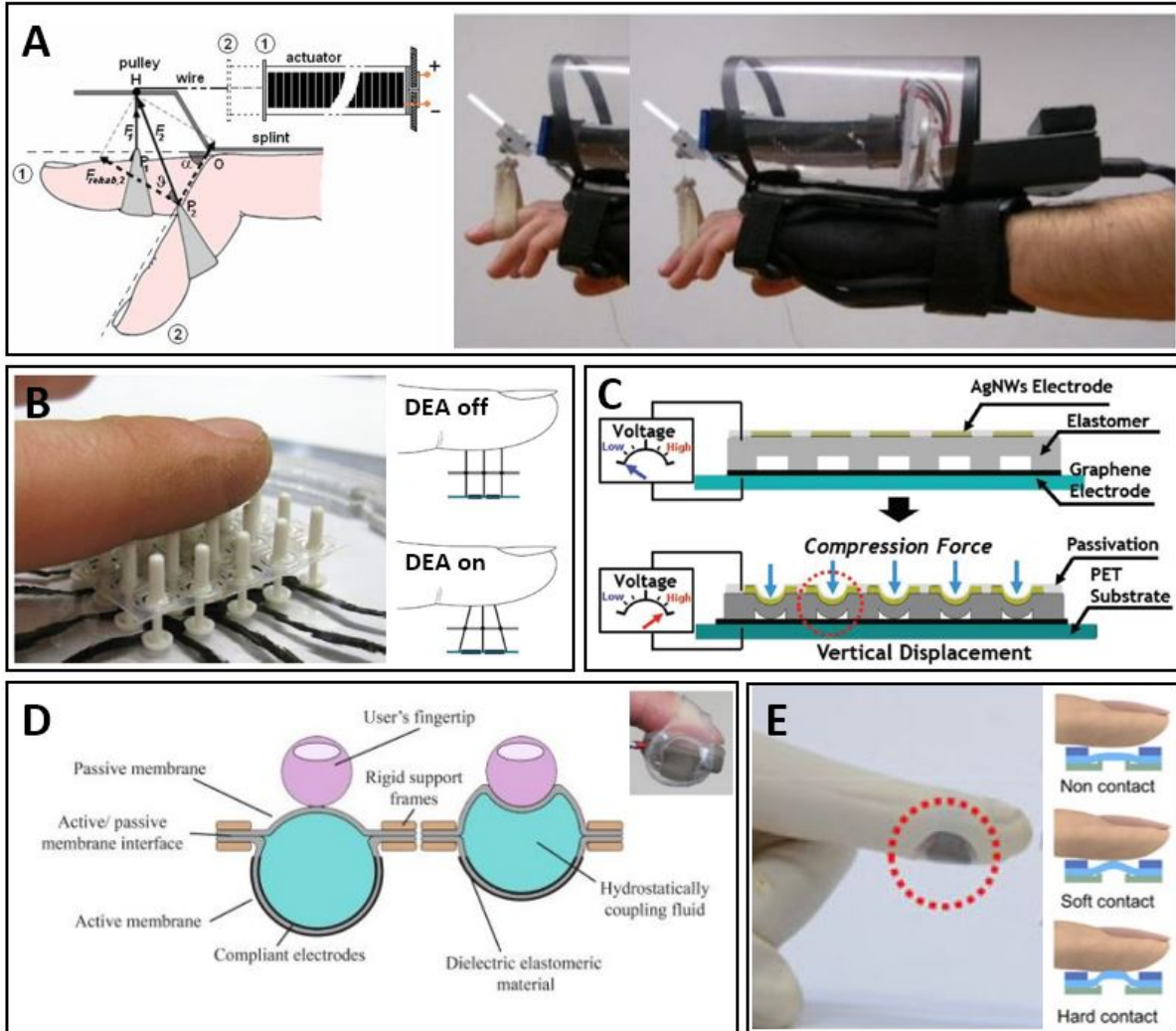
Figure 3.14 DEA-based wearable devices. (A) Device for finger rehabilitation driven by stacked contracting DEAs (adapted from (*112*)). (B) Tactile display driven by planar DEA array, using pins to transform DEA deformation to the finger skin (adapted from (*116*)). (C) Transparent tactile display with similar principle as DEA (adapted from (*117*)). The device use void patterned DE membrane, which is deformed when a voltage is applied between the electrodes. (D) Tactile interface on fingertip driven by DEA bubble combined with passive layer, where the finger is in contact with the passive layer (adapted from (*113*)). (E) Tactile interface driven by stacked DEA which buckles to give user feedback (adapted from (*115*)).

Figure 3.14D shows a tactile display mounted on fingertip (*113*). The haptic feedback is generated from DEA out-of-plane actuation by using a bubble chamber encapsulated with liquid. One part of the bubble chamber is DEA and the other part, which is in contact with finger, is the passive membrane. When the DEA actuates, the bubble shifts due to the DEA expansion. The passive membrane therefore contracts and retracts the pressure applied on the skin before. The device applies a force of 0.8N when the DEA is off, and the force changes to almost 0N

when 4kV is applied. The corresponding passive membrane displacement is 3.5 mm. Other tactile displays based on similar principle can be seen in (*114*).

Figure 3.14E shows a tactile interface driven by DEA with out-of-plane deformation (buckling) (*115*). The multilayer DEA is mounted on the fingertip. When the DEA is off, it does not contact the finger due to the used gap. When voltage is applied, the DEA buckles to contact the finger skin, which gives user feedback. A protection layer has been used to avoid direct contact between the DEA electrodes with the skin. The device is capable to output 0.6 mm displacement with 4kV as driving voltage. With 4kV, the device gives 10 mN output force at 1 Hz and 250 mN at the resonance frequency of 191 Hz. In addition, by controlling the actuation voltage at 191 Hz, the device can output 6 levels of signals.

3.9　DEA-based untethered devices

Untethered robots and wearable devices show much more potential than tethered ones. Most robots need to be untethered to perform tasks with not limited space, and humans need mobile wearable devices to adapt the daily life. DEA driving untethered robots and wearable devices are summarized in Figure 3.15.

Figure 3.15A shows the untethered robot termed FLEX1 driven by DEAs (*92*). According to the literature, FLEX 1 is the first robot driven by electroactive polymers. It is driven by acrylic-based DEAs, its speed is limited by the weight of the onboard control elements, and also by the slow speed of acrylic-based DEAs.

Figure 3.15B shows an untethered hopping robot termed Microbot (*96*), which uses DEA as a mechanical energy pump. The motion of the hopping is due to the energy release from the spring leg. To reload the deformation to the spring leg, the energy generated from the actuation of the cone DEAs bistable system, is stored into the spring leg by a ratcheting transmission system. With all the power and control system, Microbot can jump up to 38 cm. The Microbot shows a smart way to accumulate the mechanical energy generated from several DEA actuation cycles. However, Microbot is not directly driven by DEAs.

Figure 3.15C shows an untethered crawling robot driven by DEA (*95*). The robot moves by DEA expansion and the sequentially controlled electroadhesion force at the legs. The moving principle is similar to the robot in Figure 3.11H. The robot moves with a speed of 4 mm/s, which corresponds to a gait speed of 0.02 body length/s. The slow speed is due to the heavy electronics for generating the high voltage.

Figure 3.15D shows an untethered underwater swimming robot (*107*). The swimming robot is 93 mm-long, and can output fast swimming speed of 13.5 cm/s with the driving signal of 10 kV and 5 Hz. In addition, the robot can make turns with the electro-magnet controlled tail. Underwater, the mass of the bulky electronics for generating high voltage can be balanced by buoyancy, which helps the movement of the untethered robots.
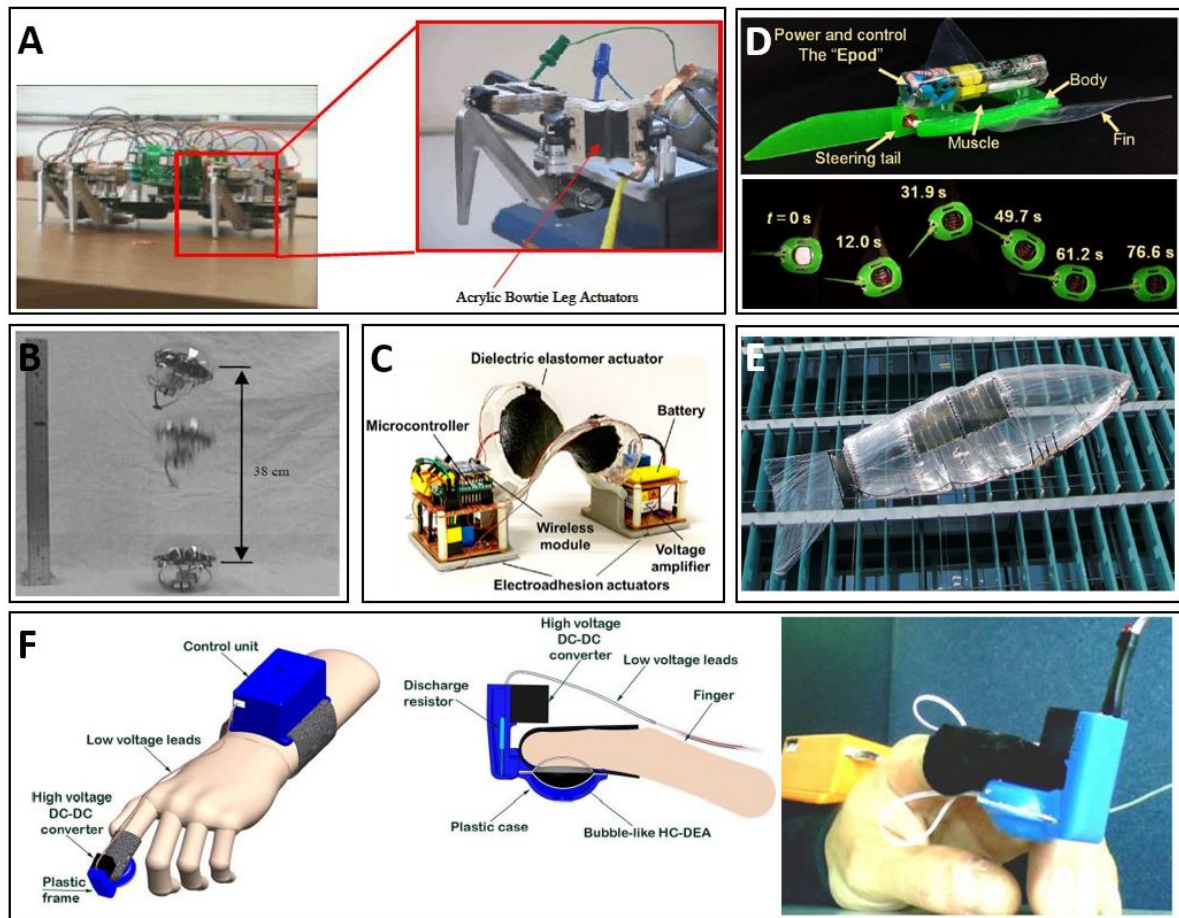
Figure 3.15 Untethered devices driven by DEAs. (A) First untethered crawling robot driven by DEAs termed as FLEX1 (adapted from (*92*)). (B) Hopping robot termed as Microbot, using DEA as mechanical energy pump (adapted from (*96*)). (C) Untethered DEA driven by DEA with DEMES and electroadhesion (adapted from (*95*)). (D) Fast untethered underwater swimming fish (adapted from (*107*)). (E) 8 m long airship use DEA to generate undulation to swim in the air (adapted from (*106*)). (F) Untethered haptic device for mimicking contact with soft surface (adapted from (*118*)). The device can communicate with external environment via Bluetooth.

Figure 3.15E shows an untethered swimming airship (*106*). The untethered airship is 8 m-long. By actuating the DEA on its body, it can generate propulsion from the body undulation. With the driving voltage of 4 kV and 0.25 Hz, the airship can swim with a speed of 45 cm/s. In this robot scale, the volume of control and power electronics is negligible compared with the robot itself. Therefore, the robot can generate motion much easily than the small scale (cm) devices. In addition, taking advantage of buoyancy from air with its big volume, the robot can improve its loading capacity.

Untethered haptic devices have also been developed. The example shown in Figure 3.15F is a DEA driving untethered haptic device (*118*) operating with the same principle as the device in Figure 3.14D. The device can interact with external devices via Bluetooth. However its big volume makes it unpractical. Wearing the device, the user is limited to use the corresponding fingertip for performing other tasks at the same time.

Remarks on DEA-based untethered devices

From the above review, DEAs show potential to drive untethered devices. Developing big size (meter scale) untethered devices is much less challenging compared to small size devices. In addition, untethered swimming robot (in the air or underwater) can take the advantage of buoyancy to balance the mass of the high voltage electronics. To develop untethered DEA driving robot capable of carrying its own auxiliary systems, the key points are to increase the DEAs output forces and to decrease the mass and volume of the auxiliary system.

The key limiting point for untethered DEAs devices is the bulky high voltage power supply. To meet more applications, robot needs to be made light for agile movement, and tiny volume for miniaturization. For wearable haptics, the high voltage limits consumer acceptance, and the big volume makes the integration of the device on body unpractical. As the case shown in Figure 3.15F, where the haptic device is worn on the fingertip, the user cannot use his finger anymore due to the big device volume. Therefore, the DEA operating voltage must be decreased to release more potential for untethered operation.

In this thesis, low-voltage fast DEAs have been developed. Further, the fast DEAs have been integrated with their power supply for making Untethered Artificial Muscle (UnArM) modules. The UnArM modules have then been used to power autonomous crawling soft robot and wearable haptic devices. The detailed work is discussed in Chapter 6.

3.10   DEA existing limitations and related improvements

In this chapter, we have reviewed the DEA fundamentals including the DEA working principle, failure modes, DE and electrode materials, DEAs construction methods, and DEA related applications in robotics and wearable devices. To address future development, the DEA existing limitations are listed below, including:

- high drive voltage;

- low output power;

- lifetime issue;

- performance repeatability;

In the following discussion, the corresponding improvements for decreasing the high drive voltage are expanded regarding to the DEA materials and fabrication methods. We focus on the first limitation in this thesis. The high driving voltage is the main limitation in the entire DEA field. Detailed work has been done during this thesis to decrease the DEA driving voltage. For the other three limitations, suggestions are given based on the author's knowledge.

High driving voltage

The high drive voltage is the major limitation to DEA-based applications. The typical thickness of dielectric elastomers is in the range of 20-50 µm, the corresponding driving voltages are generally around 1-10 kV to generate more than 10% thickness strain, regarding all the previously reviewed DEA-based applications.

There are mainly two approaches to decrease the DEA operating voltage. The first one is to decrease the DE membrane thickness (*153*). When the membrane is thin, the electrodes should add extremely low stiffness to not limit the actuation of the DE membrane. As we discussed in the section 3.5, the reported electrode materials and fabrication methods do not meet the needs for a DEA to generate acceptable strain at 100V. The electrodes should be as thin and soft as possible for a single layer low-voltage DEA. The electrodes conditions are even more critical when a stacked low-voltage DEA is desired. The electrodes should also be highly homogeneous to avoid unpredictable breakdown (as discussed in section 3.6). Reported electrode fabrication methods are all based on construction from 3 dimensions (3D), which means that the electrodes are applied by depositing the primary material units from the thickness direction. When the thickness of electrodes is comparable with the primary component (e.g. conductive carbon particles for carbon-based electrodes), using 3D construction is difficult to obtain homogenous layers in the thickness direction. Therefore, 2D construction of the electrodes shows a good advantage from this point of view, which means that the electrodes primary materials are assembled in-plane to ensure that the electrode thickness is comparable with its primary component. The electrode should also present high electrical conductivity for fast DEA charging and discharging. In addition to the quality of the thin electrode, the electrical connection

with extremely thin (nm) conductors is difficult. Handling thin membranes is also challenging, such as for the pre-stretch process.

In this thesis, we decreased the DEA operating voltage by one order of magnitude with the approach of decreasing the DE thickness, and developed low-voltage stacked DEAs with good performances. Our key elements for achieving this low-voltage DEA, is the fabrication of the thin DEA electrodes by the Langmuir monolayer method, which allows the fabrication of ultrathin layers (nm-thick). Using SWCNTs as the primary conductive materials also enables the ultrathin layers to have good surface resistance. The corresponding work is described in Chapter 5. We also present two approaches to pre-stretch sub-micron-thick elastomer membranes. The corresponding methods are described in Annex A and Chapter 5 respectively.

The second approach to decrease the DEA driving voltage is to increase the dielectric constant of the DE (*135*, *136*). Increasing the dielectric constant can usually sacrifice the properties of the DE membrane (i.e. decreased breakdown strength, and decreased strain at rupture). Good performance DE materials should be developed which have both high dielectric constant and good mechanical properties. Recently, Pan et al, (*190*) have reported that by blending liquid-metal inside elastomer, the dielectric constant can be increased without significantly sacrificing other properties of the DE material. This is a promising materials to be use for low-voltage DEAs.

The DEAs actuation voltage is promising to be further decreased by using high performance (high dielectric constant and good mechanical properties) dielectric elastomer membranes with thickness less than 5 µm, and by using the 2D assembled electrodes (constructed in-plane) developed in this thesis work.

Low output power

The power of DEAs depends on their force, strain and speed. To increase the DEAs output force, multilayer should be fabricate, especially for low-voltage thin DEAs.

The stacking process of thin DEAs needs to be performed more times compared with thick ones to achieve the same final thickness. Automated multilayer construction process is necessary for low-voltage DEAs. The previously reported multilayer fabrication processes do not involve an electrode fabrication method which allows the stacked DEA to operate below 500V. In Chapter 7, we have proposed a multilayer roll-to-roll fabrication process using the Langmuir method for the electrode fabrication. This remains an illustration of idea, where a large amount of detailed work is needed to realize this process.

With improved stacking layers, the output force in the expansion direction can be increased. To quantify the increased force for the stacked DEAs in the area expansion direction, we suppose a single layer DEA consisting of PDMS as dielectric membrane with dimension of 10 mm-long, 100 mm-wide, and 10 µm-thick, and with Young's modulus of 1 MPa. We suppose that the DEA consists of perfect electrodes which do not add any stiffening effect on the structure. The force corresponding to 10% extension strain (in linear expanding direction) is around

10 mN for the single layer DEA. Making a stack of 100 single layer DEAs, the dimension of the stacked DEA becomes 10 mm-long, 100 mm-wide, and 1 mm-thick. Therefore the output force corresponding to 10% extension strain (in linear expanding direction) is increased to 1 N. Using highly conductive electrodes (resistance less 1 MΩ) can enable the DEA fast charging and discharging (RC time constant less than 0.01 ms). Using highly elastic elastomers can improve the mechanical response time (kHz). Combination of all these aspect can therefore improve the DEA output power.

Lifetime issue

The main failure mode of DEA is the dielectric breakdown. (see section 3.3) There is a trade-off between the DEA lifetime and its performance. To output high actuation strain, DEAs should operate near the breakdown field, which results short lifetime. Theoretically, improving the breakdown strength is one approach to increase the DEA lifetime.

Self-healing properties can help the DEA to tolerate the dielectric breakdown and improve its lifetime. Self-clearing electrodes (*162*) and DE membranes capable of tolerate dielectric breakdown (*191*) have been reported. However, these reported works do not really show the capability of self-repair for the related materials. DE and electrode materials which can self-repair, are ideal to increase the DEA lifetime, as the case for using liquid dielectrics (*59*).

One hypothesis to achieve this goal is to use DE membranes which are thermally reversible. The polymer network can return to no cross-linked oligomers with the heat generated from breakdown. Further cross-linking of the DE membrane can therefore repair the DE membrane.

Performance repeatability

The DEA performance repeatability may be influenced from two aspects: (1) the viscoelasticity of the DE material; (2) the conditions of working environment.

Elastomers are generally viscoelastic. Therefore the strain corresponding to the same applied voltage can drift with time. Due to the viscoelasticity, the DEA output strain depends also on the operating frequency.

Regarding to the environment, the humidity can change the DEA performances (changed dielectric properties), where lower humidity can raise the dielectric strength of many DE materials (*134*).

To improve the DEA repeatability, the tan δ of the DE materials (ratio between the elastic loss modulus and elastic storage modulus) should be as small as possible so that the materials should be mainly elastic. To avoid the influence of humidity on the DEA performance, the DE materials could be made super-hydrophobic. The corresponding proposed approaches are described in the future work part in Chapter 7.

Chapter 4 Multifunctional Ionogel electrodes for DEA

4.1 Summary

Soft ionic conductors show potential to be used as electrodes for low-voltage DEAs (see section 3.5). In this chapter, we develop an extremely soft stretchable ionogel electrode. An imidazolium-based ionic liquid is used as the plasticizer for Poly(methyl methacrylate) to form a soft ionogel with Young's modulus of 190 kPa.

By configuring the ionogel electrode into an optical grating, we present a transparent stretchable tunable transmission grating driven by DEA. The ionogel electrode serves simultaneously as the optical surface and as the electrode for electrostatic actuation. The grating/electrode consists of a 750 nm-thick ionogel, which is bonded on both sides of a 13 µm-thick silicone membrane. The top ionogel electrode is corrugated (2 µm pitch) and serves as the diffraction grating. The bottom electrode is planar. Applying a voltage between the electrodes generates a Maxwell pressure, leading to in-plane expansion of the elastomer and electrodes. Linear actuation strain of 12.8% is obtained at 1300 V. The ionogel grating maintains accurately its shape after 500 cycles and after one month of storage. The ionogel electrodes present self-clearing properties, allowing for operation of the actuator close to the breakdown voltage.

The developed tunable grating presents an unprecedented level of integration by making accurate grating structure directly on a transparent soft ionogel conductor, which opens new possibilities for making tunable optics.

We also notice that ionic conductors show the risk of ion migration under electric field. This is disadvantageous for low-voltage DEAs because the ion migration reduces the DEA lifetime.

4.2   Introduction

Soft but accurately deformable optical elements such as tunable lenses and gratings enable dynamically changing optical properties without requiring the translation of rigid elements. Examples of flexible tunable optics in biology include the human eye where the crystalline lens is deformed by the annular ciliary muscle and the grating structures on butterfly wings (*192*).

Man-made soft tunable optics generally consist of a deformable optical element, often based on an elastomer, and an external actuator. We develop a novel way to integrate a compliant electrostatic actuator and a stretchable grating into a single multifunctional elastomer material by accurately molding a transparent soft conductive ionogel into an optical grating (or any diffractive optics)

Tunable gratings find applications today in many fields, including spectroscopy (*193*), projection displays (*194*), and telecommunication applications (*195*). Integrating the actuator with the optical elements allows for much greater compactness, higher performance and higher efficiency than using an external actuator.

Of the many miniaturized actuation mechanisms suitable for tunable optics (e.g. piezoelectric (*196*), electrostatic (*197*), thermal (*198*), electromagnetic (*199*), pneumatic (*200*)), dielectric elastomer actuators (DEAs) are particularly appealing for tunable optics in view of their compliance, very high strain, and high energy density (*65*). We present here a method to use the DEA as the transparent grating, thus creating a tunable grating where the actuator adds negligible complexity or mass to the device. As DEAs are stretchable and soft, using them to drive elastomer-based optics can allow integrating or embedding of tunable gratings into complex shapes or flexible systems.
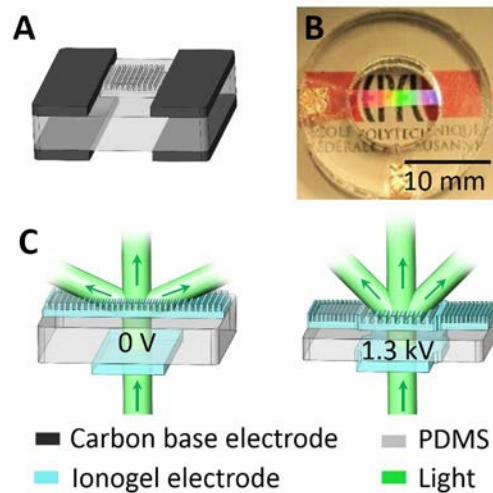
Figure 4.1 Tunable grating configuration and principle. (A) Conventional configuration of a DEA-based tunable grating consisting of a central grating bonded on a membrane compressed by the expansion of the DEA placed on the periphery; (B) Photograph of our tunable grating in which a central DEA electrode also serves as the stretchable grating; (C) Operating principle of our tunable grating: The transparent central grating is molded directly in the top ionogel electrode of a DEA. The transparent bottom ionogel electrode is on the other side of a 13 µm-thick PDMS membrane. When a voltage is applied between the two electrodes, the membrane expands in plane, increasing the grating period.

DEAs have been used to drive tunable lenses (*5*, *201*, *202*) as well as to tune the period of optical gratings (*156*, *203*, *204*). DEA-based tunable gratings generally consist of two components: a) a DEA composed of a thin elastomer membrane stretched on a frame with patterned compliant electrodes. b) a soft grating replicated in silicone, bonded on the stretched membrane and deformed by the expansion of the DEA electrodes (see Figure 4.1A). Adding the grating on the DEA reduces the maximum achievable strain, since the device becomes stiffer. The stiffening effect is even more pronounced if the grating is metallized to increase reflectivity.

One solution to improve the tuning range of a DEA-driven grating is to avoid adding the grating layer. Fang et al, (*205*) reported a tunable grating controlled by DEAs with one electrode patterned as a grating. However the electrodes are opaque so the grating must be used in reflection, which limits applications (*206*). While transparent compliant electrodes for DEAs based on hydrogels, ionogels, CNT and silver nanowires have been reported (see Chapter 3), these electrodes have not been patterned into gratings.

In this Chapter, we present a tunable transmission grating that is an integral part of a DEA using transparent ionogel electrodes of a novel formulation. The upper DEA electrode has a corrugated surface and acts both as a soft tunable grating and as the electrode of the actuator (Figure 4.1 B and C). No additional layer is therefore required on or next to the DEA, i.e. there is no additional layer that increases stiffness. The entire device is transparent, so that it can be used in transmission. The fabrication process of the tunable grating is simplified thanks to a reduced number of fabrication steps. Importantly, this work is the first time that a transparent deformable electrode has been used as a diffractive element with µm-scale periodic features, which means that we combine the intrinsic electric and optical function on one same transparent material. This opens new possibilities for tunable optics.

Our complete device (shown in Figure 4.1B) has a circular shape, with a diameter of 10 mm. The outline dimensions of the ionogel electrodes are 2 mm x 10 mm. The two electrodes are placed orthogonally on each side of the membrane (Figure 4.1C). The active grating zone of dimension 2 mm x 2 mm is therefore at the center of the PDMS membrane, where the top and bottom electrodes overlap. The overall DEA active zone dimensions are chosen such that the passive zone is large enough to not negatively impact the strain of the DEAs (*207*). The unactuated pitch of the grating-shaped electrode is 2 µm, designed for use with visible light.

4.3   Materials and fabrication

Materials

The ionogel solution is formed by adding 0.4 g of PMMA, 1.2 g ionic liquid EMITCM ((1-Ethyi-3methylimidazolium tricyanomethanide), io-li-tec, IL-0316-HP-0050) and 10 g of acetone into a 25 ml glass bottle with cover, and stirred for 5 h at 45 ℃. The solution is cooled to room temperature, and is then ready for casting transparent ionogel electrodes.

Ionogel and tunable grating fabrication

For the electrode used as the grating, the solution is applied by blade casting on a commercial plastic grating mold purchased from Edmund Optics (6 x 12 inches, 500 grooves/mm), using an applicator gap of 25 µm. For the smooth bottom electrode, the solution is blade casted on flat Polyethylene terephthalate (PET) substrate (Melinex ST-506, DuPont Teijin Films), using a gap of 25 µm to obtain a final thickness of 750 nm after solvent evaporation. After casting, the ionogel sheets are placed in an oven at 80 ℃ for 2 hours. Once dry, they are cut into 2 mm x 40 mm strips.

The PDMS membrane is fabricated following the process described by Rosset et al. (*144*) A PDMS solution consisting of Sylgard 186 (Dow Corning) part A (45.5% wt) and part B (4.5% wt) diluted in the siloxane solvent OS-2 (Dow Corning) (50% wt) is blade casted on a PET substrate coated with a poly(acrylic acid) (PAA) sacrificial layer, and then cured at 100 ℃ for 1h (Figure 4.2A). By dissolving the PAA sacrificial layer, a suspended PDMS membrane is obtained. The PDMS membrane is equi-biaxially pre-stretched with a lateral ratio of $\lambda = 1.3$, and fixed to a circular PMMA membrane holder with an adhesive layer. The pre-stretched PDMS membrane has a thickness of 13 µm (Figure 4.2B).

The corrugated grating electrode is applied on the PDMS membrane (Figure 4.2C) (the ionogel sticks to PDMS), and the grating mold is then carefully peeled off (Figure 4.2D). Next, the flat bottom electrode is applied on the other side of the PDMS membrane, oriented perpendicular to the corrugated grating electrode (Figure 4.2E). The PET substrate of the bottom ionogel electrode is peeled off (Figure 4.2F). Finally, the device is fixed on a PMMA circular holder with copper contacts.
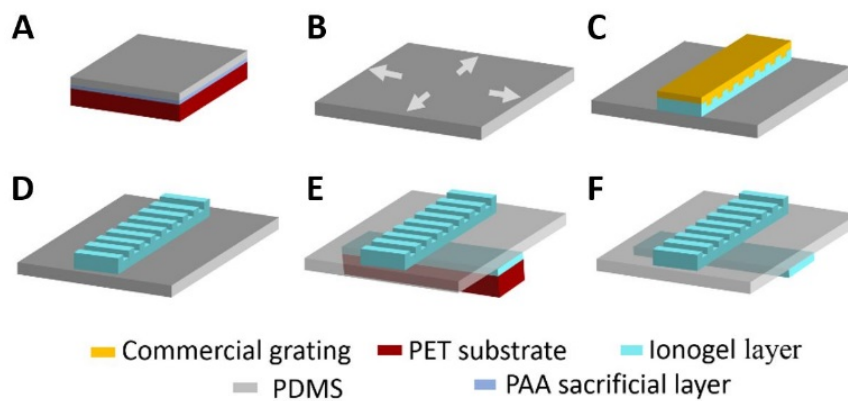
Figure 4.2 Transparent DEAs fabrication process flow. (A) Casting PAA sacrificial layer and PDMS layer on a PET substrate. (B) Release of the PDMS layer by dissolving the PAA sacrificial layer in hot water. Followed by pre-stretching of the suspended PDMS membrane with a stretch ratio of 1.3. (C) Application of the top ionogel electrode, which has been casted on a commercial plastic grating mold. (D) Peeling off the grating mold from the ionogel electrode. (E) Application of the flat bottom electrode. (F) Peeling off the PET substrate from the flat electrode, then attach the device to a PMMA holder.

4.4   Ionogel electrode properties

An imidazolium-based ionic liquid is used as the plasticizer (*208*) for Poly(methyl methacrylate), (PMMA) thus allowing the formation of a soft ionogel. The PMMA-based iono-gel is chosen for the electrode as it combines high optical transparency (93% transmittance), very low haze, good surface resistance (700 kΩ/sq for a 700 nm thick layer), low stiffness (Young's modulus 190 kPa), the ability to be molded into a grating structure with nm-accuracy, and provides good adhesion to silicone membranes.

In the following section, the ionogel is characterized regarding to its transparency, mechanical Young's modulus, thickness, electrical surface resistance, and the stability of the grating structure made by this soft ionogel.

To investigate the ionogel transparency, we performed the transmittance and haze measurement for the ionogel using an UV/Vis/NIR Spectrophotometer (Lambda 950, PerkinElmer). We measured over 93.0% transmittance for wavelengths between 500 nm and 1600 nm for a 700 nm thick ionogel film on a 20 µm-thick PDMS membrane (Figure 4.3), compared with over 94.1% transmittance for the PDMS membrane alone. The scattered light intensity is 1.2% and 1.0% in the same wavelength range for the two samples. The ionogel electrodes thus introduce negligible haze and show excellent transparency.
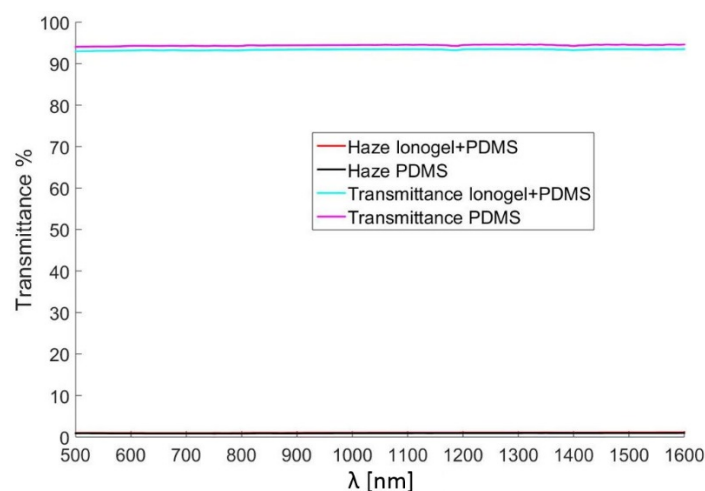
Figure 4.3 Ionogel transmittance measurement.

To study the electrode stiffness, the Young's modulus of the ionogel has been measured using Pull-tester (Instron 3340) with three suspended 6 µm-thick ionogel membranes. The stretch speed was fixed at 2 mm/min. Only the stretch-up part of the stress vs. strain curve has been used to calculate the Young's modulus. The stress vs. strain plot behaves almost linearly within the tested 20% strain. Using a linear fit, the Young's modulus of the ionogel is extracted, which is 192 ± 4 kPa. An example is shown in Figure 4.4.

The thickness of the smooth bottom electrode is 750 nm, measured by white light interferometry (Veeco Wyko NT1100). The sheet resistance of this electrode is approximately 700 kΩ/sq, measured using a 4-probe resistance measurement configuration (Keithley 2000). The grating-

shaped electrode has a maximum thickness of 750 nm and an approximately 400 nm deep grooves.
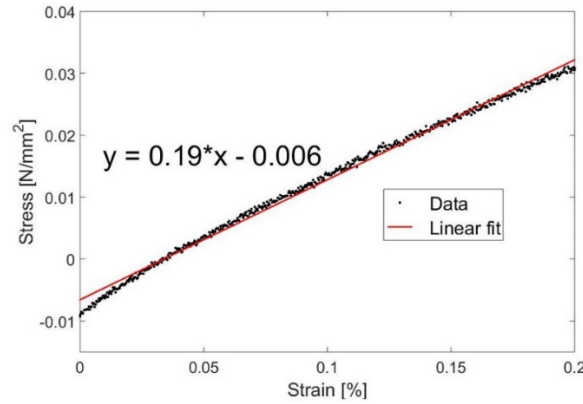
Figure 4.4 Example for Stress vs. strain plot of the ionogel electrode.

Because the grating/electrode is made of a soft ionogel material, we considered the possibility that the ionogel might flow with time, reducing the amplitude and accuracy of the grating. To investigate this, the profile of the grating electrode is measured as a function of time and of actuation cycles (Figure 4.5) using the white light interferometry (Veeco Wyko NT1100) measurement. The period of the grating electrode presents an initial period value of 1.92 µm. The soft ionogel grating period remains extremely stable over the two weeks and 500 actuation cycles. The grating height does not significantly change within 500 actuation cycles. The height decreases however by about 90 nm after one week, and by another 40 nm in the second week of storage.
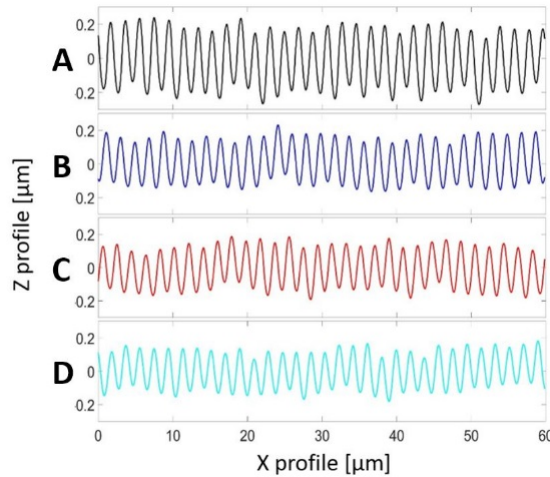
Figure 4.5 Height profile of the ionogel grating. (A) after fabrication. (B) after one week of storage. (C) after one week of storage followed by 500 actuation cycles. (D) After one additional week of storage. The grating period is unchanged, though the grating height decreases slightly.

To directly see the effect of change in grating profile on optical performance, images of the diffraction patterns are recorded immediately after fabrication, after one week of storage and after two weeks of storage (Figure 4.6). We used two samples for this experiment. The two samples were fabricated the same time and with the same fabrication conditions. The grating

patterns of the first sample were recorded as function of time. The other sample was used as reference. We firstly compare the grating patterns obtained from the first sample with different time after fabrication. A decrease in grating efficiency over time is observed because the diffraction patterns become more blurry. The second diffraction pattern even disappeared with the different experiences of the same sample. Just after the ionogel grating is fabricated, the first and second diffraction pattern can be seen clearly in Figure 4.6A. After one week of storage, we see that the intensity of the second diffraction pattern decreased compared with the one just after fabrication (Figure 4.6B). After two weeks storage, the efficiency of the grating is further decreased (Figure 4.6C). The decrease of the grating efficiency is related with the decrease of the grating high profile, as shown in Figure 4.5. We also found that, the degradation of the grating efficiency is accelerated by exposure to laser light. The grating pattern of the second reference sample was taken after two weeks of storage (Figure 4.6D). The reference sample has not been exposed to laser before. The grating pattern of the reference sample is much better than the one exposed to laser after the same storage time. This degradation of grating efficiency may due to the laser heating.
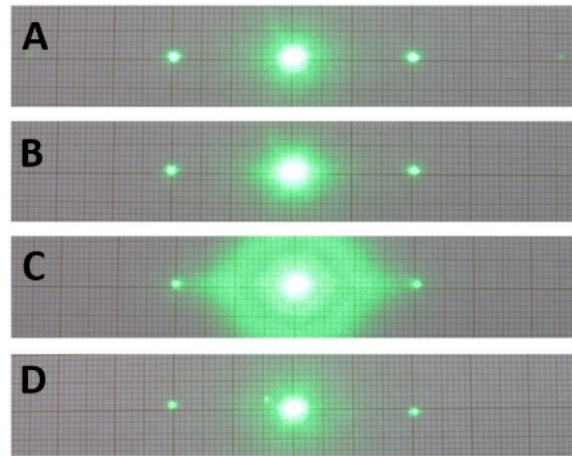
Figure 4.6 Diffraction patterns of an ionogel grating. (A) immediately after grating fabrication, (B) one week later, and (C) two weeks later. (D) Diffraction pattern after 2 weeks storage of an ionogel grating made at the same time as the one in (A) but that did not experience daily exposure to the laser. The diffraction efficiency decreased with time, and does so much more rapidly when exposed to the laser.

4.5   Performance of tunable grating driven by transparent DEA

The first-order diffraction angle θ_1 of the tunable grating is given by the well-known equation (*209*):

$$\sin(\theta_1) = \frac{\lambda}{d} \quad \text{Eq (4.1)}$$

where λ the wavelength of the incident light and d the period of the grating.

For DEAs with small deformation, the lateral strain S_x is (*128*):

$$S_x = \frac{1}{2} \frac{\varepsilon}{Y t^2} V^2 = b V^2 \quad \text{Eq. (4.2)}$$

where ε is the permittivity, Y the Young's modulus, and t the thickness of the dielectric membrane; V is the applied voltage. The grating period thus depends on the applied voltage as:

$$d = d_0 (1 + b V^2) \quad \text{Eq. (4.3)}$$

where d_0 the initial period of the grating (nominally 2 μm in our case). The first diffraction angle can be calculated by combining Eq. (4.1) and Eq. (4.3):

$$\theta_1 = \arcsin\left(\frac{\lambda}{d_0(1 + b V^2)}\right) \quad \text{Eq. (4.4)}$$

We assume that the electrodes are perfectly compliant and have no impact on the actuator strain. This is an acceptable hypothesis in this case (*153*), given that the Young's modulus and thickness product Y*t value of the electrode (~0.2 N/m) is much less than the one of the dielectric layer (~13N/m).
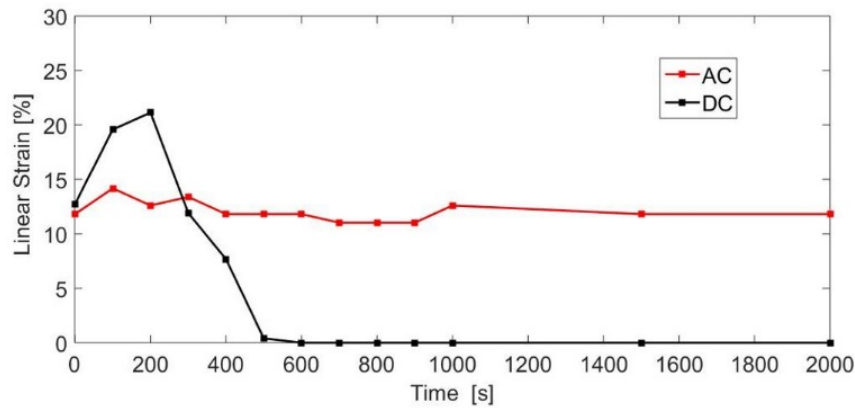
Figure 4.7 Strain comparison between AC (bipolar driving signal of +/- 650 V with changing frequency of 100 Hz) and DC (1.3 kV) driving signal, for DEA with Ionogel electrodes.

We characterized the electromechanical behavior of the fabricated transparent DEAs with ionogel electrodes (based on two samples), and compared the strain behavior with AC (bipolar driving signal of +/- 650 V with changing frequency of 100 Hz) and DC (1.3 kV) driving voltage signal (Figure 4.7) with one sample for each driving signal. With DC driving voltage signal, the strain of DEA firstly increases in a short time, then the strain decreases to zero with time further increasing. Our explanation for this strain behavior under DC signal is the ion migration. With ions migrating into the PDMS membrane, the distance between the two ionic electrode decreases. Therefore the effective electric field increases, which results the strain increases. However, when the ions migrate deeper inside the PDMS, a conductive path is therefore formed between the two DEA electrodes. The PDMS membrane with inside blended ions becomes an ionic conductor. Therefore, the strain becomes 0, because there is no more electrostatic actuation. Compared with DC driving signal, the strain of DEAs driven by AC voltage signal (100 Hz) is much more stable (with time increasing until more than 2000s where we

stopped the experiment). So AC driving signal (100 Hz) is chosen to drive the DEA with ionogel electrodes.
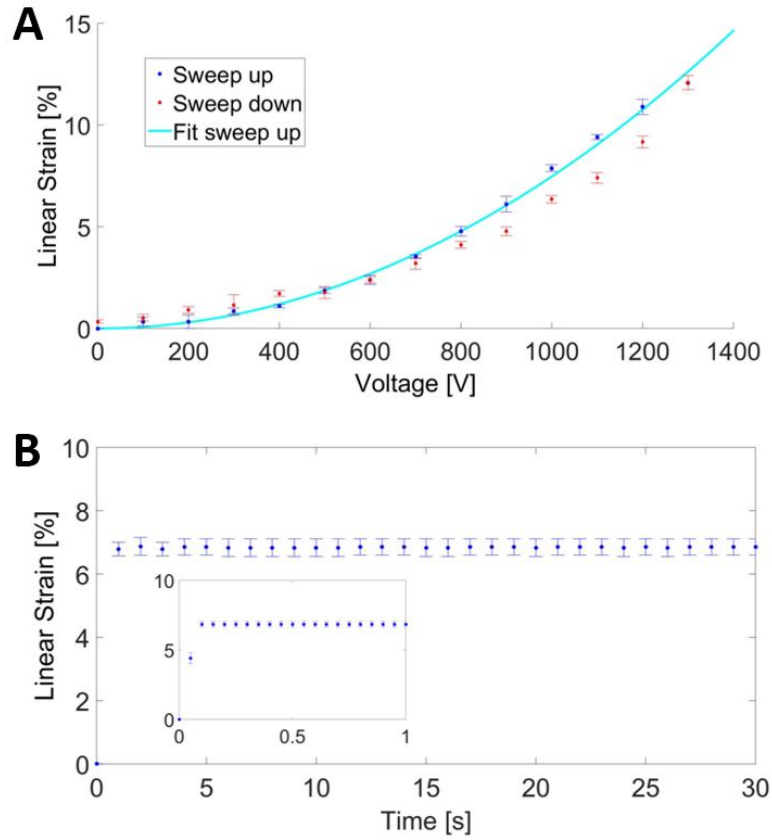
Figure 4.8 Performance of DEA with ionogel electrodes. (A) Actuation strain generated as a function of the AC voltage (at 100 Hz) applied to the DEAs device. Strain is measured during loading and unloading, with 20 s interval between points. (B) Strain as a function of time for a fixed AC signal (bipolar voltage signal of +/-500V with frequency of 100 Hz). Inset: zoom between 0 and 1 showing stabilization within 100 ms.

Based on the same tunable grating sample, the DEA strain vs. voltage and time has been characterized. The grating strain vs. voltage curves are plotted in Figure 4.8A. The strain data points are taken during the loading and unloading of the voltages, with 20s interval in between. The loading data shows the typical V^2 strain dependence expected for DEA in the small displacement case. At 1.3 kV actuation voltage, 12.8% linear strain is obtained. Figure 4.8B plots the strain vs. time with a bipolar driving signal (+/- 500V with changing frequency of 100 Hz). 7% strain is reached within 1 s, and then remains constant thereafter for over 1000 s (when we stopped the experiment).

Dielectric breakdown is a major failure mode for DEAs (see chapter 3). With our ionogel electrodes, when dielectric breakdown occurs, the heat generated by the leakage current locally vaporizes the electrode around the failure point, thus stopping the current flow and allowing the DEA to continue operating. DEAs with these ionogel electrodes present the property of self-clearing, allowing extended operation very close to the breakdown voltage.

The change of the first diffraction angle is recorded as a function of the drive voltage (AC, bipolar 100 Hz). The tunable grating is placed 79.5 mm from a screen. Laser light (200 mW) with a wavelength of 532 nm is shone through the center of the tunable grating actuators. Several diffraction orders are recorded with a camera as the voltage is swept. The distance between the first diffraction laser spot and the principle one, noted as D (mm), is measured by using ImageJ software [ImageJ-win64, http://imagej.net/Fiji]. The first diffraction angle, θ1 (degree), can then easily be calculated by Eq. (4.5):

$$\theta_1 = \arctan\left(\frac{D}{79.5}\right) \quad \text{Eq. (4.5)}$$

The evolution of θ_1 vs. applied voltages is plotted on Figure 4.9, together with the simple theoretical model, Eq. (4.4). The first diffraction angle changes from 15.67° at 0 V to 14.25° at 1.3 kV, leading to a tuning range of 1.42°. A fit of the experimental data using Eq. (4.4) leads to a d_0 value of 1.97 µm, which is very close to the measured value (1.92 µm). An excellent agreement is found between the theoretical model and the figure based on the experimental data points.
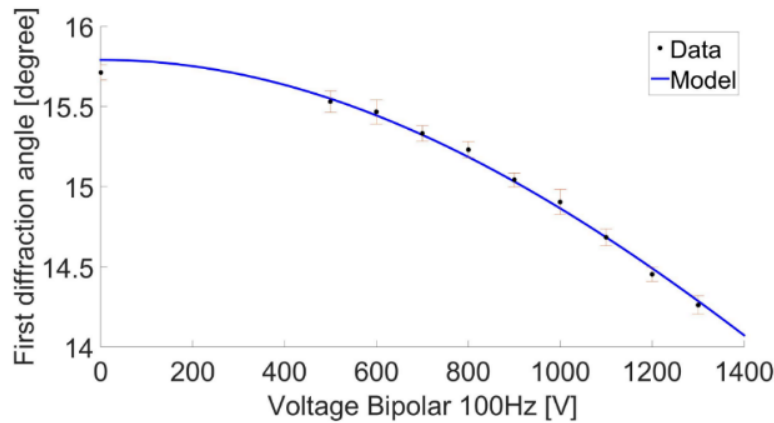
Figure 4.9 First diffraction angle as a function of the drive voltage. The model of Eq. (4.4) shows very good agreement with the data using an initial grating pitch of 1.97 µm.

4.6   Conclusion

In this chapter, the related work has shown that soft ionogels can be integrated into DEA-based optical devices to play the dual role of transparent electrode and tunable diffractive optical element. DEAs usually have black light-absorbing electrodes (see Chapter 3), which greatly limits their use for optical devices. Our soft transparent electrodes enable new configurations in which light passes through the deformable actuators, which can be accurately patterned as diffractive optical elements. The self-clearing properties of the ionogel electrodes can increase the lifetime of the actuator, as it makes dielectric breakdown events non-destructive for the device. In addition to gratings, these ionogel electrodes can be applied to other optical

applications actuated by DEAs, such as tunable lenses in configurations where the electrodes are in the light path, molding the electrodes to provide combined optical and electrical function.

The ionogel is extremely soft, which is an advantage to be used for low voltage operating thin DEAs. Nevertheless, with the presence of ions, they may migrate, or get injected into DE membrane under high electric field with DC drive signal. This leads to a short lifetime for the DEA. Therefore other non-ionic ultrathin conductors fabricated using Langmuir technology are developed in the following chapter to be used as stretchable electrodes for low voltage ultrathin DEAs.

Chapter 5 Low voltage DEAs based on ultrathin electrodes fabricated using Langmuir-based technology

5.1 Summary

We remind here that the basic goal of this thesis is to decrease the DEA driving voltage. The corresponding approach is to decrease the DE membrane thickness. This approach requires the electrode to be ultrathin (nm), soft (Young's modulus less than 10 MPa), highly homogenous, and highly conductive for fast DEA actuation (see section 3.5).

In this chapter, Langmuir-Schaefer (LS) method is used to fabricate ultrathin electrode for low-voltage driving DEAs.

Firstly, a Multiwalled Carbon Nanotube/alkyl-polythiophene (MWCNT/PT) composite is developed as the ultra-thin stretchable electrodes. These composites form stable composite monolayers at the air-water interface that can then be LS transferred onto a Poly(dimethylsiloxane) (PDMS) elastomer membrane. The composite monolayer electrode shows a surface resistance of ~20 MΩ/sq, and remains conductive up to 100% uniaxial strain. We present a method to fabricate low-voltage DEAs using the LS transferred electrodes. By using a mask during the transfer step, the electrodes can be patterned on both sides of a 1.4 µm-thick prestretched PDMS membrane. Due to the low stiffness of the electrode. The DEA generates 4% linear strain, correspond to 8% area strain, at an actuation voltage of 100 V, an order of magnitude lower than the typical DEA operating voltage.

However, the fabricated DEA is slow (~1 Hz), which is limited by the resistance of the MWCNT/PT electrode. Therefore, electrode system with much better surface resistance has been developed for faster DEA operation. In addition, we increased the PDMS membrane thickness to 6 µm, and fabricated stacked DEA to improve the output force.

To improve the electrode surface resistance, we changed the conductive materials to Single walled carbon nanotubes (SWCNTs). We used octadecylamine functionalized SWCNTs so that the SWCNTs could form stable monolayer at the air-water interface. By transferring the SWCNTs onto PDMS substrate with LS method, we developed novel ultra-thin stretchable electrodes. Compared with the MWCNT/PT system, we improved the electrode surface resistance to 0.2 MΩ/sq, 2 orders of magnitude smaller. These electrodes are also stretchable: at 125% linear stretch, the surface resistance is still less than 1 MΩ/sq. The good conductivity enables fast DEA actuation over 200 Hz. The low roughness of the ultrathin electrode allows

the fabricated stacked DEA to present predictable dielectric breakdown field. With a driving voltage below 450V, the stacked DEA generates more than 20% area strain.

5.2   Introduction

The electrodes used for DEAs are generally assumed not to contribute to the stiffness of the devices (*128, 139*). This has been the case for many DEAs fabricated using carbon grease electrodes on acrylic films of thickness several tens of µm. The electrode stiffness can only be ignored when the following inequality is respected (*147*) (see Annex B):

$$Y_e * t_e << Y_m * t_m \quad \text{Eq. (5.1)}$$

where Y_e is the Young's modulus of the electrode, t_e is the electrode thickness, Y_m is the Young's modulus of the DE, and t_m is the DE membrane thickness.

If Eq. 5.1 is not satisfied (eg, for very thin elastomer membranes, or stiff metallic electrodes), the DEA strain/voltage relation (Eq. 3.10) must be corrected to account for the stiffening impact of the electrodes. This highlights the role of the electrode mechanical properties on the performance of DEAs. Given that the electrodes are generally stiffer than the elastomer ($Y_e > Y_m$ for nearly all non-ionic materials used in DEAs), when the membrane is made thinner, then the electrode thickness t_e or the electrodes stiffness Y_e must also be further decreased to maintain actuation strain, as summarized in Eq. 5.1.

For the sake of discussion, let us assume a DEA made from 1 µm-thick PDMS sandwiched between two 10 nm-thick gold electrodes. The bulk Young's modulus for gold is 75 GPa, which gives an $Y_e * t_e$ value of 750 N/m. Assuming 1 MPa for the PDMS dielectric layer, the $Y_m * t_m$ value for the DE is 1 N/m. The $Y_e * t_e$ value of the two gold electrodes is 1500 times of the DE layer, 5 orders of magnitude more than the required low stiffness condition. Therefore, for this thin DEA using only 10 nm-thick gold electrodes, no measurable actuation would be observed as the gold electrodes would effectively block motion.

Fabrication technologies for the stretchable electrodes of DEAs have been reviewed in Chapter 3. We have concluded that among the reported electrode materials, the nanotube-based conductors and soft ionic conductors are promising to be used as low-voltage DEA electrodes (see section 3.5). In the Chapter 4, we discovered that ionic conductors have the ion migration problem, which influences the DEA lifetime. Therefore, the nanotube-based materials are developed in this part.

The reported DEA electrode construction methods for nanotubes/nanowires are all based on construction from 3D (deposition of primary conductive materials from the thickness direction, see section 3.10), including spray, drop casting and matte transferring. 3D construction methods are not suitable anymore for fabricating ultrathin electrodes. Because the electrodes fabricated with these methods cannot achieve homogeneous layer, especially when its thickness needs to be comparable with the diameter of the primary nanotubes/nanowires materials (see section 3.5).

To achieve thin and homogenous thin electrodes, we chose the Langmuir monolayer method for the electrode fabrication. The Langmuir monolayer method is introduced in the following

content regarding to the materials, working principle, working process, and advantages compared with the reported methods for low-voltage DEAs electrodes fabrication.

5.3 Langmuir monolayer method introduction
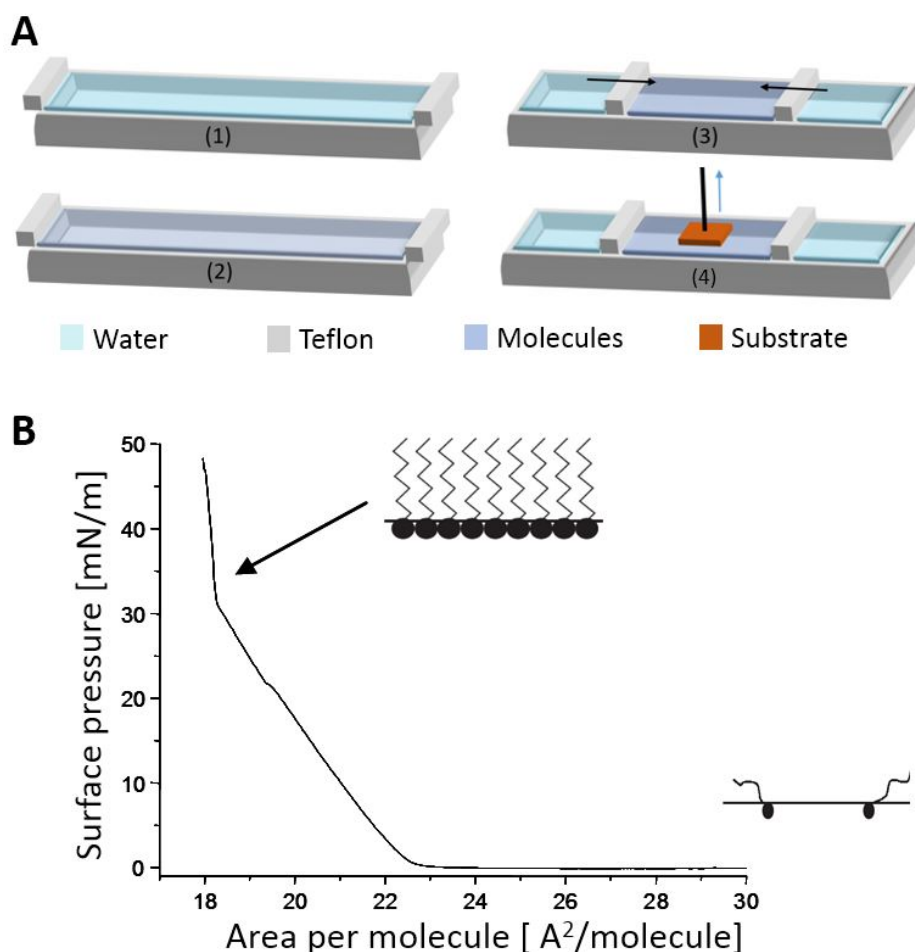
Figure 5.1 Langmuir method working principle. (A) Cartoon illustration of monolayer formation and transfer process: (1) Ultrapure water filled into the LB trough. (2) Solution deposited at the air-water interface. (3) Monolayer compressed by the barriers. (4) Transfer of monolayer onto substrate by LS method; (B) Example of Langmuir compression isotherm with cartoon illustration of phases. The isotherm shows the evolution of the surface pressure as a function of the mean molecular area.

Principle and surface pressure-area isotherms

Insoluble amphiphilic molecules, such as typically fatty acids, can form monomolecular layers at the air-water interface due to the presence of hydrophilic and hydrophobic parts in their structure. A simple example of this phenomenon is the floating of oil on water surface. Some polymers (*210*, *211*) or functionalized CNT (*212*, *213*) also form stable monolayers at the air-water interface.

Thus, by first spreading and then compressing amphiphilic molecules at the air-water interface, one can fabricate monomolecular films with controlled density, called Langmuir monolayers. Such monolayers can be highly ordered over areas of several hundreds of cm^2 (*211*). The process is shown in Figure 5.1A by cartoon illustration. When the Langmuir trough is filled with ultrapure water, an air-water interface is generated (Figure 5.1A (1)). Amphiphilic molecules (possessing both hydrophilic and hydrophobic groups in their chemical structure) can be spread on the air-water interface, by depositing the corresponding diluted solution dropwise using a micro-syringe (Figure 5.1A (2)). The monolayer density can then be increased using the compression barriers of the Langmuir trough, as shown in Figure 5.1A (3). During the compression, the surface pressure, defined as the decrease of the ultrapure water surface tension (72 mN/m) in the presence of the monolayer, is measured simultaneously by the corresponding sensor system. The Langmuir compression isotherm corresponds to the surface pressure change as function of the mean area per molecule A defined as the trough area divided by the number of spread molecules. In cases where the exact number of molecules is unknown (for example when CNT are used), the surface pressure is plotted as function of the trough area. As an example, the isotherm of a fatty acid monolayer is reported in Figure 5.1B. Slope changes corresponding to phase transitions are detected. The description of the different phases, whose structures depend on the molecule and temperature, will not be detailed here. Generally, at the initial molecular area corresponding to zero surface pressure, the monolayer displays a phases coexistence between a 2D gaseous phase and a 2D liquid or condensed phase. Upon compression, the surface pressure lift-off is observed when the gaseous phase disappears. Then through further compression, the surface pressure increases until it reaches the collapse pressure corresponding to the appearance of 3D structures.

Transfer of the Langmuir monolayer onto substrate

These Langmuir monolayers can be transferred onto solid substrate using the vertical Langmuir-Blodgett (LB) or horizontal Langmuir-Schaefer (LS) method (*214*). A cartoon illustration corresponding to the LS transfer used in this work is given in Figure 5.1A (4). The monolayer is first compressed to a desired surface pressure corresponding to a condensed phase. The substrate is then horizontally moved towards the monolayer using a stepper motor. Once substrate/monolayer contact is established, the substrate is raised and thus covered by one monolayer. Depending on the molecules and the affinity between layers, this process can be repeated or not to transfer subsequent monolayers.

Advantages of using Langmuir method for DEA electrode fabrication

Langmuir monolayer technology is an appealing alternative to commonly used electrode fabrication methods as it allows the formation of nm-thick films by assembling molecules or nanoparticles in 2 dimensions (2D). It is a powerful method to transfer molecular monolayers from an air-water interface to a solid substrate. In addition to producing films one single molecule thick, this technique has the advantage of controlling the density of molecules in the

monolayer. Due to the 2D fabrication process, the electrodes fabricated by Langmuir technology can achieve a high homogeneity.

Langmuir method have been used to fabricate molecular sensors (*215*), photo-electrochemical devices (*216*), organic semi-conductor devices (*217*), and field effect transistors (*210*). DEA electrodes based on stretchable monolayer conductors obtained by Langmuir monolayer deposition method have not yet been investigated.

With the above discussed advantages, Langmuir monolayer method is developed to fabricate the stretchable electrodes for DEAs in the following parts.

5.4   MWCNT-based electrode fabricated using Langmuir method
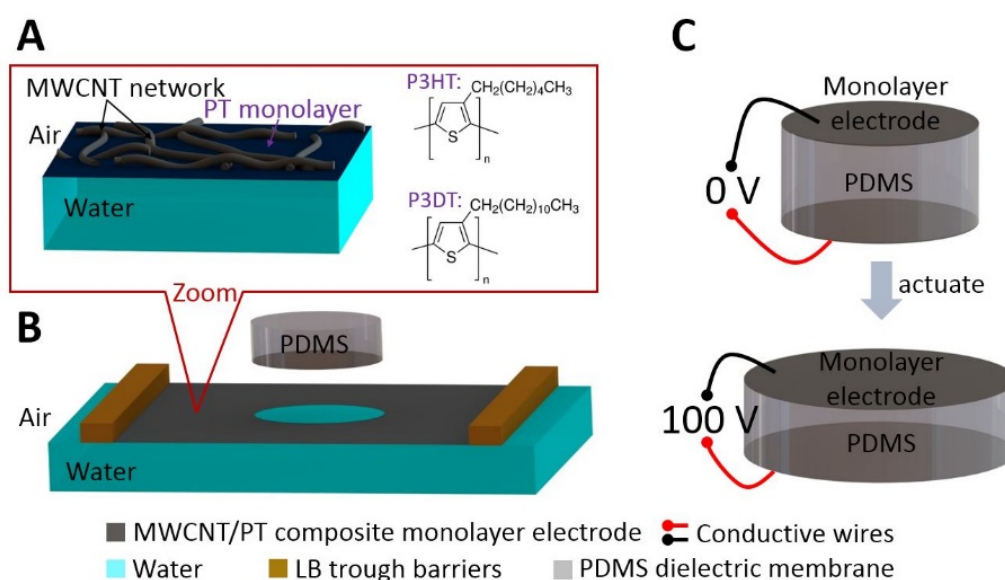
Figure 5.2 Low-voltage DEAs made using Langmuir-Schaefer transferred monolayer electrodes. (A) Monolayer composite electrode formed at the air-water interface: interconnected MWCNT network embedded inside an alkyl-polythiophene (PT) monolayer. The insets correspond to the chemical formula of the two PT with different side chain length. (B) Langmuir-Schaefer (LS) transfer of the composite monolayer from the air-water interface onto the pre-stretched PDMS dielectric membrane to make one electrode of the DEA. (C) The DEA consists of a 1.4 µm-thick pre-stretched silicone membrane sandwiched between two sub-100 nm thick composite monolayer electrodes.

In this section, hydrophobic alkyl-polythiophenes (PT) and hydrophilic Multiwalled Carbon Nanotubes (MWCNT) are developed to form the monolayer stretchable conductor. By mixing in a solvent, the two component can form a stable amphiphilic composite by pi-interaction (*218*). This stable dispersion of the composite can be spread on the air-water interface using Langmuir method. In the formed composite electrode, the MWCNT network is embedded in a PT monolayer (Figure 5.2A). PT, as conducting polymer, should contribute to the electronic conductivity and stabilize non-functionalized hydrophilic MWCNT at the air-water interface. Two types of PT with different linear alkyl side chains are studied (poly-3-hexylthiophene (P3HT) and poly-3-decylthiophene (P3DT), with chemical formula inserted in Figure

5.2A), since it has been shown that the side chain length has a significant effect on the PT material properties. The longer this chain is (up to 12 C for existing commercial products), the smaller the Young's modulus and the electrical conductivity (*219*). The MWCNT/PT composite monolayer is then transferred from the air-water interface to a Poly(dimethylsiloxane) (PDMS) elastomer membrane using the LS method (Figure 5.2B). The adhesion is provided by the hydrophobic affinity between the PDMS substrate and PT from the composite monolayer. The electrodes are evaluated based on their morphological, electrical and mechanical properties with regards to DEA application. Then, 1.4 µm-thick pre-stretched PDMS membrane is sandwiched between two LS transferred composite electrodes to make a 100 V operating DEA (Figure 5.2C, for details see the fabrication process in section 5.4.3). The DEA is characterized regarding its strain and speed.

5.4.1 Materials and method

Materials

Regio-regular poly(-3-hexyl-thiophene-2,5-diyl) (P3HT, CAS 156074-98-5 and purity of 99.995%), and regio-regular poly(-3-decyl-thiophene-2,5-diyl) (P3DT, CAS 110851-65-5 and purity of 99.995%) are ordered from Sigma-Aldrich and used as received. Multi-walled Carbon Nanotubes (MWCNTs; external diameter 15-35 nm, length ≥ 10 µm) are purchased from Nanothinx S.A. (Rio, Greece). Poly(acrylic acid) (PAA, 25% soln. in water, CAS 9003-01-4) is ordered from Chemie Brunschwig. Ethanol (99.9%) and chloroform (99.2%) are ordered from VWR Prolabo Chemicals. PDMS (Sylgard 186, MED-4086) and PDMS solvent (OS-2) are ordered from Dow Corning (Auburn, MI).

Solution preparation

Polythiophene (PT) solutions: PT (P3DT or P3HT) solution (0.167 g/L) is prepared in chloroform-ethanol 9:1 v/v and then sonicated for 30 min.

MWCNT/PT mixed solutions: PT is dissolved in a chloroform solution (0.167 g/L), then sonicated for 30 min. MWCNTs are dispersed in ethanol (20 g/L), then sonicated for 1 h. Both solutions are mixed in a volume fraction of 9 (chloroform)/ 1 (ethanol) and then sonicated for 5 h before being centrifuged for 15 min at 3000 rpm. The supernatant is collected and two additional centrifugations of 15 min each are performed. This process is optimized according to the optical microscopy images and the surface resistance value of the LS transferred composite MWCNT/PT monolayers as outlined in Annex C.

Langmuir assembly

The monolayers are formed in a KIBRON Langmuir-Blodgett (LB) trough (MicroTroughX). An adequate solution volume (depending on the desired monolayer density) is

spread over an ultrapure water surface (18.2 MΩ·cm Millipore Simplicity, Billerica, MA) using a micro-syringe. After solvent evaporation, the monolayer is compressed at a barrier speed of 10 mm/min and the surface pressure recorded. In the following, the isotherms are plotted as a function of the trough area instead of the area per monomer. The monolayer homogeneity at the air-water interface is verified in-situ by Brewster Angle Microscopy; more detail on this technique is given in Annex C. For the LS transfer, the monolayer is kept at a surface pressure of 15 mN/m and the PDMS substrate is horizontally moved towards the monolayer at 2 mm/min using a stepper motor from KIBRON. Once substrate/monolayer contact is established, the PDMS substrate is raised until the transfer is complete.

Atomic Force Microscopy (AFM)

100 µm-thick PDMS membranes are fabricated using the method reported by Rosset et al, (*144*) and used as substrates for the LS transfer of the monolayer electrode (see Annex C). The AFM images are performed using the Peak Force Tapping mode with a Dimension ICON microscope from Brüker. AFM imaging is carried out in air using ScanAsyst-air cantilevers (Brüker) with a spring constant of 0.4 N.m^{-1}. 10 µm x 10 µm images are obtained with the height mode and a 256 x 256 resolution, at a 0.5 Hz scan rate. Data processing is performed with NanoScope software version 1.40 (Brüker).

Surface resistance measurement

The monolayers LS transferred onto 100 µm-thick PDMS substrates are placed against two rectangular copper electrodes enclosing a 1cm x 1cm square as active zone. The resistance is determined from the measured current with 10 V applied between the copper electrodes. A Gamry Instruments potentiostat (reference 600) is used for these measurements.

Surface resistance stability measurement

The effect of PT doping on the surface resistance stability is investigated. The transferred PT monolayers are immersed into a 0.15M FeCl$_3$ in acetonitrile solution for 5 min and then rinsed with acetonitrile (*210*). For each type of monolayer, six individual samples were measured to obtain an average value and standard deviation.

Surface resistance *vs*. strain measurement

The surface resistance of monolayers LS transferred onto suspended 100 µm-thick PDMS substrates is measured for different stretching conditions. Two samples are used in each case and a speed of 0.1 mm/s is applied during stretching. The effect of sample cycling on the surface resistance is also investigated. For that, 10 stretch-release cycles (1 %/s) per sample are used, with 30 s delay between each cycle.

5.4.2 MWCNT/Polythiophene ultrathin electrode characterization

In the following section, the stretchable electrodes based on MWCNT/P3HT and MWCNT/P3DT monolayers are characterized regarding their structure, surface morphology, surface resistance, stretchability and stiffness.

Monolayer structure at the air-water interface and on PDMS substrate

Compression isotherms of the two MWCNT/P3DT and MWCNT/P3HT composite monolayers spread at the air-water interface are shown in Figure 5.3A. The isotherms for both systems have similar shapes, characterized by a steep rise in surface pressure until collapse is detected at around 60 mN/m. This indicates the formation of condensed and stable monolayers at the air-water interface. It should be noted that in the absence of PT, MWCNTs do not form a Langmuir monolayer at the air-water interface. A Brewster Angle Microscopy (BAM) image of the MWCNT/P3DT monolayer compressed at 15 mN/m is shown as inset in Figure 5.3A. 15 mN/m is chosen as the LS surface transfer pressure because the slope of the isotherm plot is almost constant after 15 mN/m until the collapse. By comparison with the pure PT monolayer (see Annex C), MWCNTs embedded in the PT condensed phase can be observed as small brighter spots with a size of a few microns. Some slightly larger bright spots corresponding to MWCNT aggregates can also be observed. Similar behavior is observed for the MWCNT/P3HT monolayer. BAM images thus confirm that PTs are good dispersants for MWCNT (*212*). To gain further insight in the structure of this monolayer, AFM images are taken of the composite monolayers transferred onto 100 µm-thick PDMS substrates at a surface pressure of 15 mN/m (Figure 5.3B). As no significant effect of the PT side chain length has been detected, only the AFM image of the MWCNT/P3DT system is shown. AFM topography reveals a uniform and dense MWCNT carpet. MWCNTs are clearly interconnected forming a network which reflects the successful LS transfer of the composite monolayer from the water surface to the PDMS substrate.
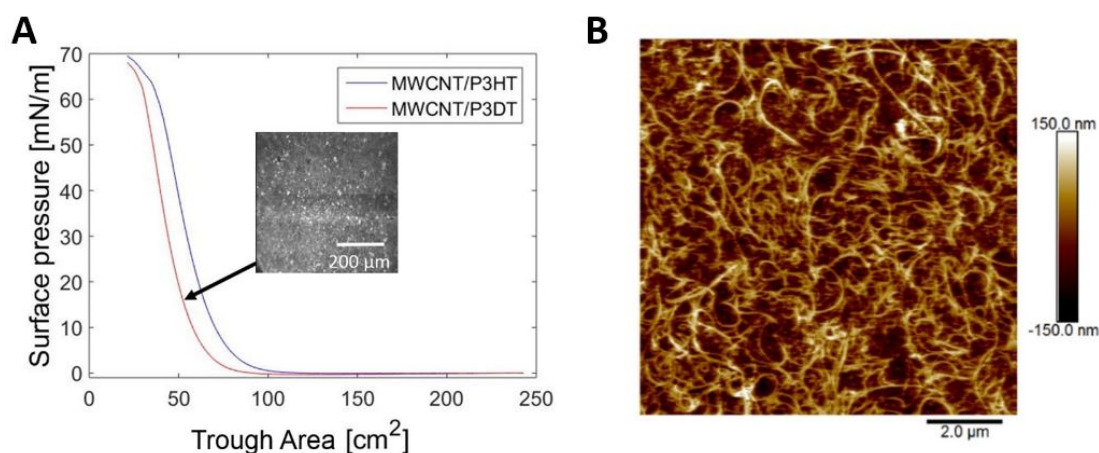
Figure 5.3 MWCNT/PT electrode isotherms and structure. (A) Surface pressure versus trough area isotherms for MWCNT/P3HT and MWCNT/P3DT monolayers with BAM image of MWCNT/P3DT monolayer at 15 mN/m. (B) AFM image of MWCNT/P3DT monolayer transferred at 15 mN/m onto PDMS substrate.

The electrode thickness is obtained from AFM height profiles on a MWCNT/P3DT monolayer electrode transferred onto a smooth glass substrate. The MWCNT network presents an average thickness of about 30 nm, which corresponds to the expected diameter of the MWCNT. As the very thin P3DT continuous phase is not easily detected on these height profiles, its thickness of 2 nm is obtained from LS transferred pure P3DT monolayers onto glass substrate. The thickness of the composite monolayer electrode thus varies between 2 nm and 30 nm, according to the thickness of both components (see Annex C).

Monolayer electrode surface resistance: stability over time

Because doping of electronically conducting polymers can strongly increase their electronic conductivity (*210*), the surface resistances of doped and undoped pure P3DT monolayers have been compared. The role of MWCNTs within the MWCNT/P3DT composite monolayer is then highlighted by comparison with pure P3DT monolayer.

The change in surface resistance as function of time is shown in Figure 5.4 for undoped and doped P3DT monolayers (with no MWCNTs). The surface resistance of doped P3DT monolayer presents a value of ~20MΩ/sq immediately after doping. However, the resistance increases with time due to a progressive de-doping process, reaching a high and stable value of 80 GΩ/sq after 24 h. Since the electrode conductivity must remain stable for DEA applications, this electrode based on a doped P3DT monolayer cannot be used. The undoped P3DT monolayer has an initial surface resistance of order GΩ/sq, increases by about one order of magnitude after a few hours, and finally reaches a stable high value (~ 50 GΩ/sq) after 24 h. Thus, the undoped P3DT monolayer is not stable with time neither, and cannot be used as an electrode for DEAs. The huge resistance will result in extremely slow DEA devices.
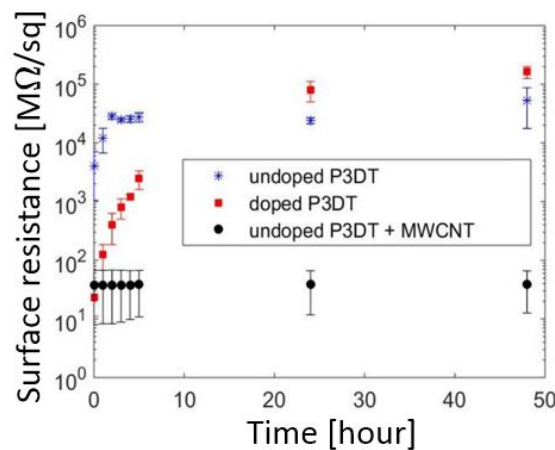
Figure 5.4 Surface resistance as a function of time. For doped P3DT, undoped P3DT and undoped MWCNT/P3DT monolayer electrodes.

For the composite monolayer consisting of undoped P3DT and MWCNTs, an initial surface resistance of about 20 MΩ/sq is measured, two order of magnitude lower than that of undoped P3DT. This value is close to the one measured for freshly doped P3DT, however the surface

resistance stability is greatly improved by the presence of MWCNTs, remaining stable even after 48 h (Figure 5.4) where we stopped the measurement. This result indicates that in the presence of undoped P3DT, the electronic properties of the composite monolayer are dominated by MWCNTs.

The surface resistance as a function of time for the undoped MWCNT/PT electrode is independent of the PT side chain length (see Annex C). Electrodes with both PTs present a stable surface resistance for 48 h, with almost similar values (~ 40MΩ/sq). While side chain length of PT usually has a significant effect on electronic properties of bulk material (*219*), no effect is observed here since the electronic properties of the composite monolayers are mainly governed by the MWCNT network.

Morphology and surface resistance under different conditions

Because the surface resistance and topography are very similar for both MWCNT/P3HT and MWCNT/P3DT systems, the electrode stretchability characterization are carried out only on MWCNT/P3DT monolayers. The morphology of the MWCNT/P3DT composite monolayer for different stretching conditions is investigated. The surface resistance as a function of strain is then characterized.

As mentioned above, the electrode characterization is carried out on MWCNT/P3DT monolayers transferred onto 100 μm-thick PDMS substrate. To study the possible changes in surface topography upon stretching of the PDMS substrate covered by the MWCNT/P3DT electrode, AFM images are taken under different stretching conditions (Figure 5.5).

From Figure 5.5A, taken at 20% uniaxial strain applied to the PDMS substrate, one can see that the MWCNTs are slightly deformed along the stretching direction, but remain interconnected. For device at 0% strain, taken after 100% uniaxial strain or after 10 cycles with 60% uniaxial strain, AFM images show an interconnected MWCNT network, indicating that stretching up to 100% (Figure 5.5B) or after 10 cycles with 60% uniaxial strain (Figure 5.5C) does not break the network. For all stretching conditions, no significant morphology change is detected at this length scale once the sample is relaxed back to 0 % strain, compared with the sample not submitted to any strain (Figure 5.5D). More AFM images under different stretching conditions are in Annex C.
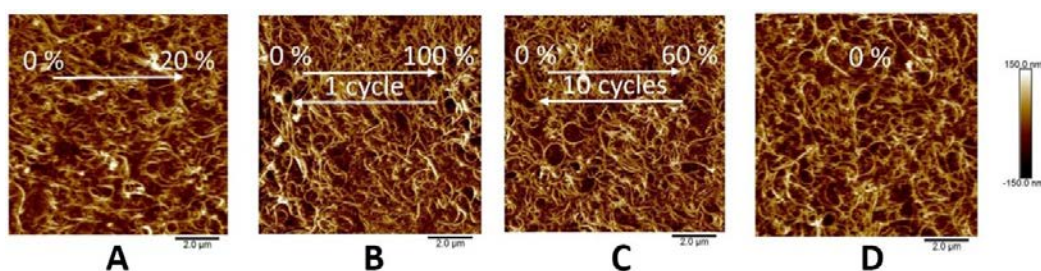
Figure 5.5 AFM images of MWCNT/P3DT monolayer electrode. (A) At 20% uniaxial strain. (B) Returning to 0% strain after 100% uniaxial strain. (C) Returning to 0% strain after 10 cycles with 60% uniaxial strain. (D) At 0% uniaxial strain without applying any strain. The arrows indicate the stretch direction.

Influence of the applied strain on the electrode surface resistance

The evolution of the surface resistance of the MWCNT/P3DT composite monolayer as a function of the applied strain is shown in Figure 5.6, based on two samples (see Section 5.4.1).

Figure 5.6A shows the change of the surface resistance for a sample submitted to different successive cycles of increased maximum strain between 20% and 100%. For clarity, only the stretching up cycles are presented. During the first 20% strain, the resistance increases by about one order of magnitude, indicating a decrease in the interconnection ratio within the MWCNT network. When returning to 0% strain, the resistance does not reach its initial value, but increased by a factor of 6. This highlights an irreversible change in electrical properties due to mechanical deformation. This occurs on every cycle with increasing maximum applied strain. One can however observe that the increase in surface resistance after returning to 0% strain is less pronounced above 60% strain. It is noteworthy that the monolayer electrode remains conductive up to 100 % uniaxial strain.
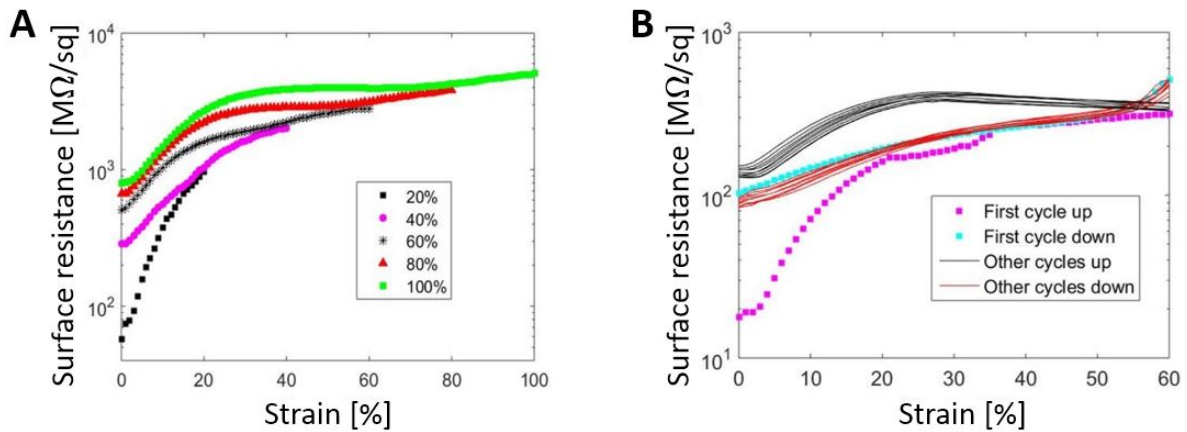
Figure 5.6 Surface resistance *vs.* strain for MWCNT/P3DT monolayer transferred onto 100 µm-thick PDMS substrate. (A) Starting with 20% strain up to 100% with 20% steps on the same sample and with a release to 0% after each stretch. (B) During 10 cycles with 60% uniaxial strain (30 s delay between each cycle).

In order to understand whether this change in resistance is related to cycle number or to the maximum strain, another sample is stretched repeatedly to a constant maximum strain of 60%. The surface resistance variation through each of the 10 stretch cycles is shown in Figure 5.6B. One should mention that the end points of both up and down cycles do not present exactly the same value, which is due to the 30 s delay during each measurement. Upon the first cycle, the surface resistance increases by about one order of magnitude reaching ~ 317 MΩ/sq as the strain varies from 0% to 60%. One can observe that this variation is lower than the one obtained at 60% strain for the sample considered in Figure 5.6A, due to the different history that both samples have experienced. One can also notice that the main evolution is observed during the first 40% strain. After returning to 0% strain, as previously evidenced, the surface resistance does not recover its value before stretching, meaning that the MWCNT network interconnection is changed irreversibly. For the 9 other following cycles to 60 % linear strain, the surface

resistance does not change drastically. Thus, even though monolayer electrical properties degradation occurs during the first stretch cycle, the sample can be submitted to many successive cycles at quite large strain without significant variation of electrode surface resistance. By comparing Fig. 4.5A and B, it can be concluded that the degradation of the monolayer electrode is mainly related to the maximum applied strain.

Stiffness measurement of MWCNT/PT composite monolayers

The stiffness of the monolayer electrode is measured by Pull test using a uniaxial tensile testing setup. By measuring the stiffening impact of the monolayer on a very soft 10 µm-thick PDMS substrate (Young's modulus of 40 kPa), the stiffness of the monolayer can be computed. Uniaxial cyclic stretching (20% strain) is applied to the PDMS membrane using a linear motor (UAL from Saia-Burgess) at a strain rate of 0.67 %/s. The stretching direction is parallel to the 2 mm edge of the PDMS rectangle (2mm x 20mm) so that stretched PDMS membrane is in a pure shear stress state. During the measurement, the force and the sample elongation is simultaneously measured using a force sensor (Futek LSB200, capacity 100 mN) and the encoder of the stepper motor, thus enabling the representation of the stress-strain relationship. A LabVIEW code was written to control the motor and the force sensor for the whole experiment process.

After measuring the Young's modulus of bare PDMS membranes, the monolayer electrodes is LS transferred onto those PDMS membranes. The Young's modulus of the PDMS + electrode bilayer is determined using the same parameters as for the bare PDMS membrane. The PDMS + electrode bilayer is formed by two adherent layers with equal length and width, so the electrode Young's modulus is calculated using (*220*):

$$Y_{bilayer}t_{bilayer} = Y_{PDMS}t_{PDMS} + Y_{electrode}t_{electrode} \qquad \text{Eq. (5.2)}$$

where *Y* is the Young's modulus and *t* is the thickness.
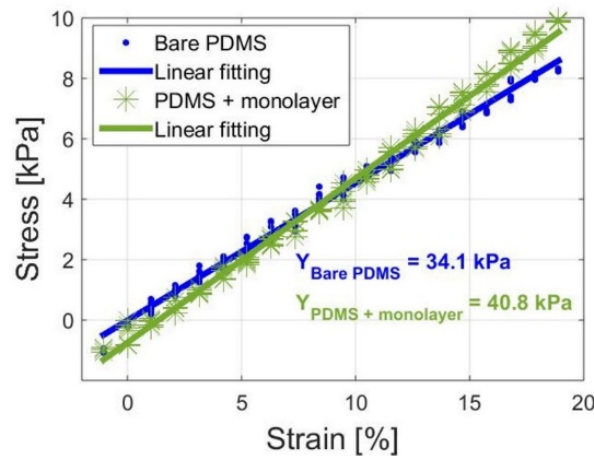
Figure 5.7 Stress-strain curve to determine the electrode stiffness. For a bare PDMS substrate and the same PDMS substrate covered with MWCNT/P3DT monolayer electrode.

An example of stress-strain curves is shown in Figure 5.7 for both the 10 µm-thick bare PDMS substrate and the bilayer consisting of the same PDMS substrate covered by the MWCNT/P3DT monolayer electrode. Young's moduli of 34.1 kPa and 40.8 kPa are extracted for the bare PDMS substrate and the PDMS/electrode bilayer respectively. A $Y_{electrode}*t_{electrode}$ value of 0.08 ± 0.03 N/m is then deduced from Eq. 5.2 based on 6 different samples.

The stiffness of pure P3DT monolayers (without MWCNT) is also measured for comparison. A $Y_{PT}*t_{PT}$ value of 0.07 ± 0.03 N/m is obtained, which is almost the same value as for MWCNT/P3DT monolayers. Therefore, it can be deduced that within the composite monolayer, the P3DT continuous phase plays the dominating role for the Young's modulus. The presence of the MWCNT network embedded inside the P3DT monolayer does not significantly increase the stiffness of the monolayer.

To conclude, the composite MWCNT/ P3DT monolayer electrodes have a surface resistance of about 20 MΩ/sq, remain conductive at 100% linear strain, and show a small Y_e*t_e product (0.08 N/m) in comparison with the $Y_{PMDS}*t_{PDMS}$ product of the 1.4 µm thick PDMS membrane used in the ultrathin DEA (1MPa x $1.4.10^{-6}$ m = 1.4 N/m). All these properties lead to a promising electrode material to fabricate a low voltage operating DEA.

5.4.3   DEA fabrication using MWCNT/PT ultrathin electrode
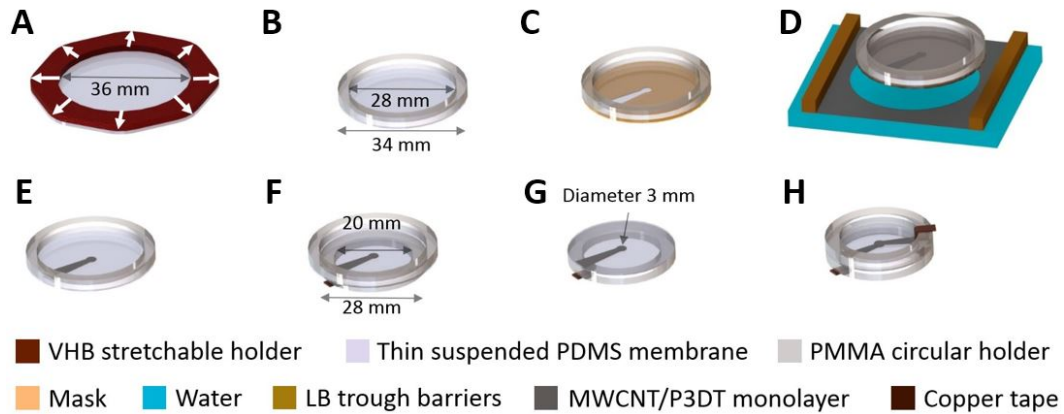
Figure 5.8 Fabrication process of 1.4 µm-thick DEA by using LS technology. (A) Suspended PDMS (Sylgard 186) equi-biaxially pre-stretched (initial thickness: 2.0 µm, after stretch: 1.4 µm). (B) Suspended stretched 1.4 µm-thick PDMS membrane fixed onto a PMMA holder. (C) A mask is placed on the suspended membrane. (D) LS transfer of the monolayer electrode formed at the air-water interface onto the suspended PDMS membrane with mask. (E) Patterned monolayer electrode on the PDMS. (F) Transferring the PDMS membrane covered with the patterned monolayer electrode onto a smaller PMMA holder. (G) Patterned monolayer electrode on the lower side of PDMS with the electrode connected with copper tape, and the upper side of PDMS without electrode. (H) DEA made with LS electrode technology.

A 2.0 µm-thick PDMS membrane (Sylgard 186, Dow Corning) is prepared as the DE membrane of the DEA. To handle and pre-stretch sub-micrometer suspended PDMS membranes, a stretchable holder is developed, made from acrylic adhesive (3M, VHB 4905) covered

with silicone transfer adhesive (Adhesive Research, ARclear 8932). Using the stretchable holder, a suspended 2.0 µm-thick PDMS membrane is released from the PET substrate, and pre-stretched equi-biaxially to 1.4 µm-thick with a linear ratio of 1.2 (Figure 5.8A). The pre-stretched PDMS is fixed onto a Poly(methyl methacrylate) (PMMA) holder (Figure 5.8B) using silicone transfer adhesive. A mask (made from the backing film of the silicon adhesive, ARclear 8932) is placed on the suspended PDMS (Figure 5.8C). The mask served to pattern the monolayer by LS transfer and to keep the suspended PDMS membrane flat (Figure 5.8D). After the LS transfer of monolayer electrode, one drop of ethanol is deposited between the gap of the mask and the PDMS layer to help in peeling off the mask. The thin pre-stretched PDMS membrane with patterned monolayer electrode on one side is obtained (Figure 5.8E). The PDMS membrane with one transferred electrode, is applied onto a smaller holder, with the PDMS bare surface facing up (Figure 5.8F). On this smaller holder, the first patterned electrode is in contact with the copper connection (Figure 5.8G), and the second electrode is LS transferred on the other side (Figure 5.8C-5.8E). Another smaller holding ring is bonded to the DEA using silicone transfer adhesive to provide the electrical contact for the second electrode (Figure 5.8H). A small drop of conductive silver epoxy is used to ensure a good electrical connection between the monolayer electrode and the copper tape. The active zone of the DEA (3 mm diameter cycle) is located at the center of the pre-stretched 1.4 µm-thick PDMS membrane, where the two electrodes overlapped (see Annex C).

Voltages up to 130 V are applied between the two electrodes of the fabricated DEA. The diameter linear strain of the center active zone is measured as a function of the applied voltage. The linear strain is also measured as a function of frequency to characterize the speed of the DEA.

5.4.4   DEA performance with MWCNT/PT electrodes

As we discussed in the introduction, the electrode stiffness is very important when the DE layer is made thin (see section 5.2). The MWCNT/P3DT monolayer electrodes add very little stiffness to the DEA, allowing good strain at 100V, but such thin electrodes have higher electronic resistivity, limiting device speed. We thus present here both strain and speed data for our DEAs.

The linear strain of active zone for one fabricated DEA is plotted as a function of the applied voltage in Figure 5.9A. For the first time, DEA actuation strains of well above 1% are obtained with driving voltages below 100 V. 4.0% linear strain is obtained for a 100V driving voltage, which corresponds to a S_x/V^2 value of 400 %/kV^2. This value is three times higher than the previous record (*177*).

The actuation strain *vs.* actuation frequency curve (Figure 5.9B) is recorded with the same device. For frequencies below approximately 0.2 Hz, the strain is constant, and for higher frequencies the strain decreases. The electromechanical 3dB point occurs at 1 Hz. Two main reasons can lead to this quite low response speed: electrical charging time, and viscoelastic losses.

The electrical charging time of a DEA can also be approximated as RC, where R is the total resistance of the electrodes (including feedlines) and C is the capacitance of the DEA. At 100 V (i.e., at 4% strain), the total resistance of the 2 electrodes is 860 MΩ, and the capacitance of the DEA is calculated as 1.4 x 10^{-10} F. The computed RC time constant is 120 ms.

The charging time constant of the DEA is determined experimentally by recording the current flowing to the DEA in response to a step in drive voltage. The classical current jump followed by an exponential decay is observed, from which an electrical charging time constant τ of 150 ms is extracted. In the highly simplified model of an RC circuit, the RC time constant corresponds to the time at which the voltage reaches 63.2% of its maximum value. Given the quadratic response of DEAs, 63% of the voltage corresponds to 40% of the maximum strain. Using 100 V as our drive voltage, one sees in Fig. 5.9A that the linear strain at 63 V is 1.5%. From the strain *vs* charging time plot at 100 V based on another sample (Figure 5.9C), 1.5% linear strain is reached between 125 ms and 250 ms, consistent with the electrical charging time.
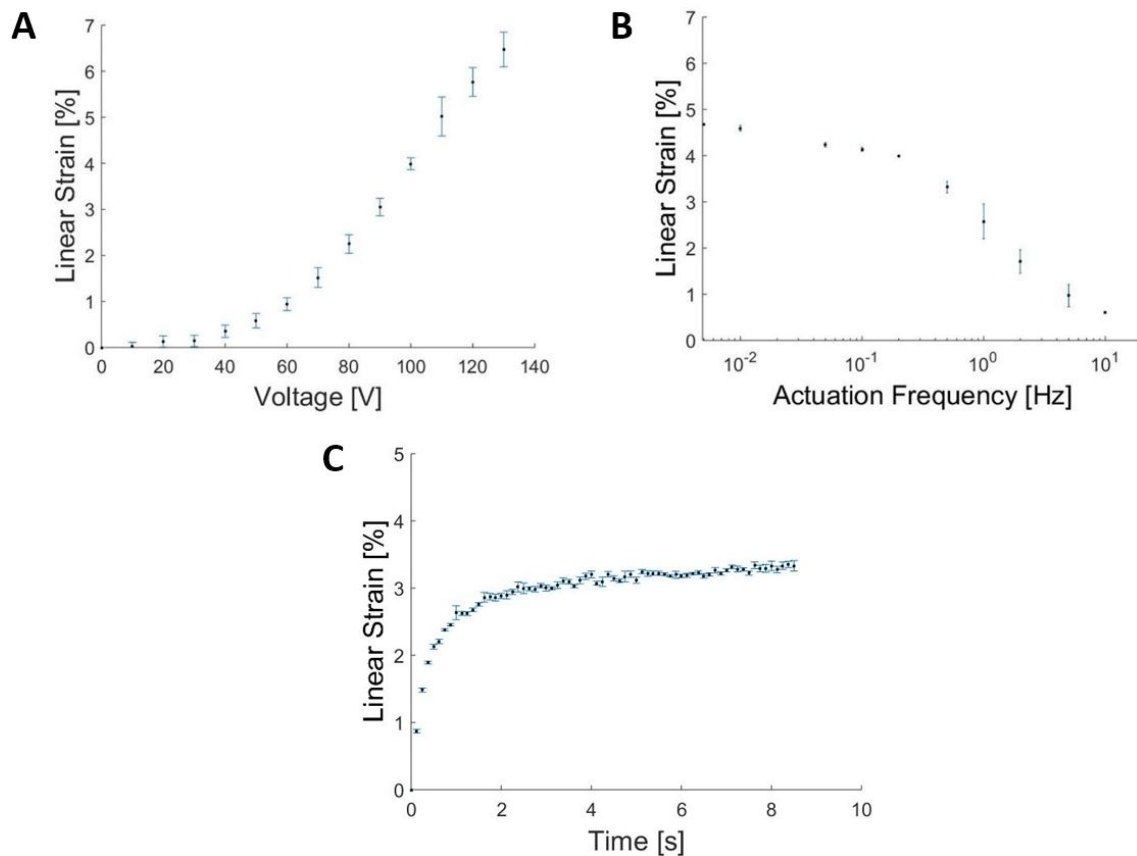
Figure 5.9 Characterization of DEA consisting of a 1.4 µm thick silicone elastomer membrane with the monolayer electrodes. (A) Strain vs. voltage curve, showing about 4% linear strain at 100V. (B) Strain vs. actuation frequency curve. (C) Strain vs. charging time plot.

The overall response speed can thus be mostly explained by the electrical charging time constant. The response time has also a small component due the viscoelastic response of the elastomer. We expect the later to be very small, given the data reported for kHz DEAs using similar silicone elastomers (*5*). To achieve faster low-voltage operating DEAs, the electrode conductivity must be improved, detailed work is described in the following section.

5.5   SWCNT-based electrode fabricated using Langmuir monolayer-method

In the previous section 5.4, MWCNT/PT composite electrodes were developed to fabricate DEAs operating at 100V using the Langmuir-Schaefer (LS) method. We achieved single layer DEAs capable of performing more than 8% area strain with just 100 V as driving voltage. However, as the electrode surface resistance was 20 MΩ/sq, the RC time constant limited the DEAs operating speed to less than 1 Hz. To operate at high frequency, the electrode must have low surface resistance even in the stretched state to not limit the DEA charging time by the RC time constant.

In this section, we present stretchable ultrathin electrodes based on Single Walled Carbon Nanotubes (SWCNTs). We increased the stretchable electrode surface resistance to 0.2 MΩ/sq to improve the DEA speed. In addition, the DE layer thickness is increased to 6 µm, and stacked DEAs are fabricated to improve the output force. The thin and low-roughness SWCNT electrodes fabricated using Langmuir monolayer method, allow the stacked DEA to fail with predictable dielectric breakdown voltage (below 450V). Their good surface resistance allows the DEA to achieve fast actuation of more than 200 Hz.

In the following content, the SWCNT-based electrode is presented regarding to its materials, surface topology, electrical conductivity, and stretchability. The performances of the fabricated stacked DEA using these electrodes are then presented regarding to its strain and speed.

5.5.1   Materials and methods

Materials

Octadecylamine functionalized Single Walled Carbon Nanotubes (SWCNTs) (chemical formula inserted in Figure 5.10) are purchased from Sigma-Aldrich (652482-100MG). Chloroform (≥99.8%) is purchased from Sigma-Aldrich (319988). Polydimethylsiloxane (PDMS) (LSR 4305, Part A and B) is ordered from Bluestar (A-221-05). The PDMS solvent (OS-2) is ordered from Dow Corning (Auburn, MI). Poly(acylic acid) solution (PAA) (25%) is purchased from Chemie Brunschwig (00627-50). The silicone transfer adhesive ARclear is ordered from Adhesive Research (ARclear 8932). The polyester sheets are the backside cover of the silicone adhesive ARclear. Poly(methyl methacrylate) (PMMA) plates are ordered from

Laumat GmbH. Polyethylene terephthalate (PET) substrates of 125 µm-thick is purchased from DuPont Teijin (Melinex ST-506).

Fabrication of SWCNT-based ultra-thin stretchable electrodes by Langmuir-Schaefer method

Functionalized SWCNTs are dissolved in chloroform to a concentration of 0.5 g/L. The solution is sonicated for 3 h in an ice bath. After the solution is warmed to room temperature, it is ready to be used for forming a SWCNT ultra-thin electrode by the horizontal Langmuir-Schaefer (LS) transfer method (see section 5.3, Figure 5.1). Ultrapure water (resistivity >18.2 MΩ·cm) is produced by an ultrapure water purification system (Werner, EASYpure II). The water is poured inside the Langmuir-Blodgett trough (KSV NIMA, KN 2002). 80 µL of the prepared SWCNTs solution is deposited drop by drop on the air-water interface. The floating monolayer is compressed by the barriers of the Langmuir trough to achieve a desired surface pressure. The ultra-thin layer is then transferred onto the corresponding substrates by Langmuir-Schaefer (LS) method for further characterizations. In Annex D, the more detailed fabrication and care during the experiments are described. The related observation during the experiments are also included.

Surface resistance measurement of 2D Langmuir assembled SWCNT electrodes

To study the electrode surface resistance as function of LS transfer number and surface pressure (see section 5.3), the functionalized SWCNT monolayers are LS transferred onto Polyethylene terephthalate (PET) substrates. For the electrode surface resistance as function of the LS transfer layer number, the LS transfer surface pressure is fixed at 3mN/m, while varying the LS transfer number. For the electrode surface resistance as function of the LS transfer surface pressure, the LS transfer number is fixed at 6 layers, while varying the LS transfer surface pressure. The surface resistance of the fabricated electrodes is measured using a 4-probe resistance measurement configuration (Keithley 2000).

SWCNT-based electrodes stretchability test: surface resistance vs. strain

To measure electrical resistance vs strain, a 100 µm-thick PDMS membrane is used as the stretchable substrate on which the SWCNT electrode is transferred by LS method. The PDMS substrate is treated by oxygen plasma (OP) (Manufactured by Diener, ZEPTO). Then the SWCNT-based monolayer compressed at a surface pressure of 3mN/m is LS transferred onto the OP treated PDMS substrate. The LS transfer is repeated 6 times (LS transfer number: 6). To measure the ultra-thin electrodes electrical resistance on the elastomer substrate, patterned 20 nm-thick gold strips are used for the electric connections. Since 4-wire resistance measurement methods is chosen, 4 patterned gold bands are deposited on the SWCNT electrode. The 20 nm-thick gold layers are deposited on the SWCNT layer by a gold sputter coater (JEOL, JFC-1200). For the resistance versus strain measurement, the SWCNTs electrode on PDMS substrate is mounted on a Motorized Linear Stage (Standa, 8MT175-50) to stretch the electrode. The zone with the gold contacts is fixed onto a PMMA rigid support using a silicone

adhesive to avoid deformation of the gold connections. The stretchable zone is a suspended PDMS membrane coated with SWCNT-based electrodes. The electrode is stretched at a speed of 2mm/s, and the electrode resistance is recorded. One sample is stretched successively for 5 cycles, with maximum applied uniaxial strain increasing (5%, 10%, 15%, 20% and 25%). A LabVIEW (National Instruments) code is used to control the instruments and record the data.

SWCNT electrodes surface topography

To study the surface topography of the ultra-thin electrodes, the SWCNT layers are LS transferred onto PET substrate at 3 mN/m for 6 LS transfer. The corresponding topography images of the LS transferred layers are obtained by an Atomic Force Microscope (AFM) (BRUKER, Dimension Edge with ScanAsyst) using the tapping mode.

5.5.2   SWCNT-based ultrathin electrode characterizations
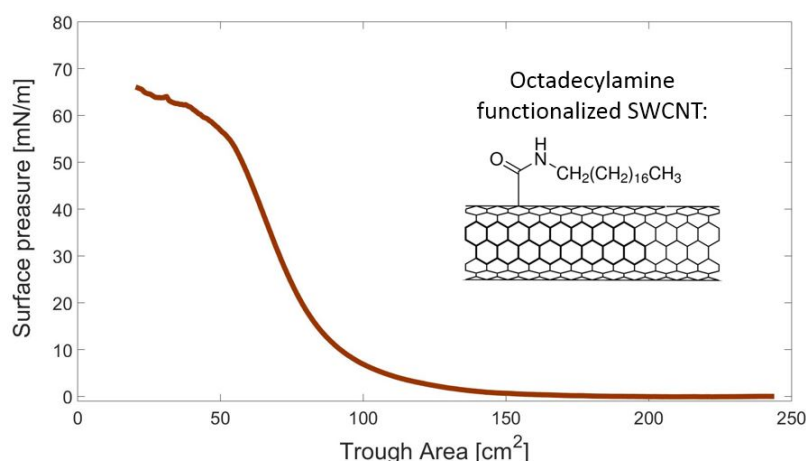
Figure 5.10 SWCNT compression isotherm

The compression isotherm is performed by depositing 60 µL of the SWCNT solution (0.5g/L) at the air-water interface. The isotherm is given in Figure 5.10, which proves that stable monolayer of SWCNTs is formed at the air-water interface. The octadecylamine side chains allow the SWCNTs to spread at the air-water interface. The surface pressure increases during the compression, until the collapse happens at 50 mN/m. The formed SWCNT monolayer can be transferred onto suitable substrates by LS method for further characterizations.

Different LS transfer numbers (3 to 12 transferred monolayers) and different LS transfer surface pressures (3, 10 an 30mN/m) are studied to determine the influence of LS transfer parameters on the electrode properties.

As seen in Figure 5.11A, the surface resistance of the electrodes decreases with increasing number of transferred monolayers. Transferred with surface pressure at 3 mN/m, with 3 LS transfers, the electrode surface resistance is about 1 MΩ/sq, and decreased to 0.2 MΩ/sq with

6 LS transfers. Electrodes with 12 transfers have an even lower surface resistance of 0.04 MΩ/sq. The speed of which the surface resistance decreases, is more than the one of the increase of LS transfer number. This is logical, because the interlayer connection increases with the LS transfer number increase, which helps to improve the electrical conductivity. We chose to use the electrodes with 6 LS transfers, as this electrode meets the surface resistance conditions for 1 kHz operating DEAs (see Annex E).

From Figure 5.11B, with 6 transferred layers, one sees that the LS transfer surface pressure has little influence on the sheet resistance in the studied range. Because the average values are all around 0.12 MΩ/sq for the different samples fabricated with LS transfer surface pressures of 3 mN/m, 10 mN/m and 30 mN/m. Therefore 3mN/m is chosen as the LS transfer surface pressure.

The ultrathin electrodes made at 3mN/m as LS transfer surface pressure, and with 6 LS transferred layers, meet the electrical requirements as electrodes for the DEAs to operate at 1 kHz. Therefore, stretchability and surface roughness characterizations of the electrodes are performed.
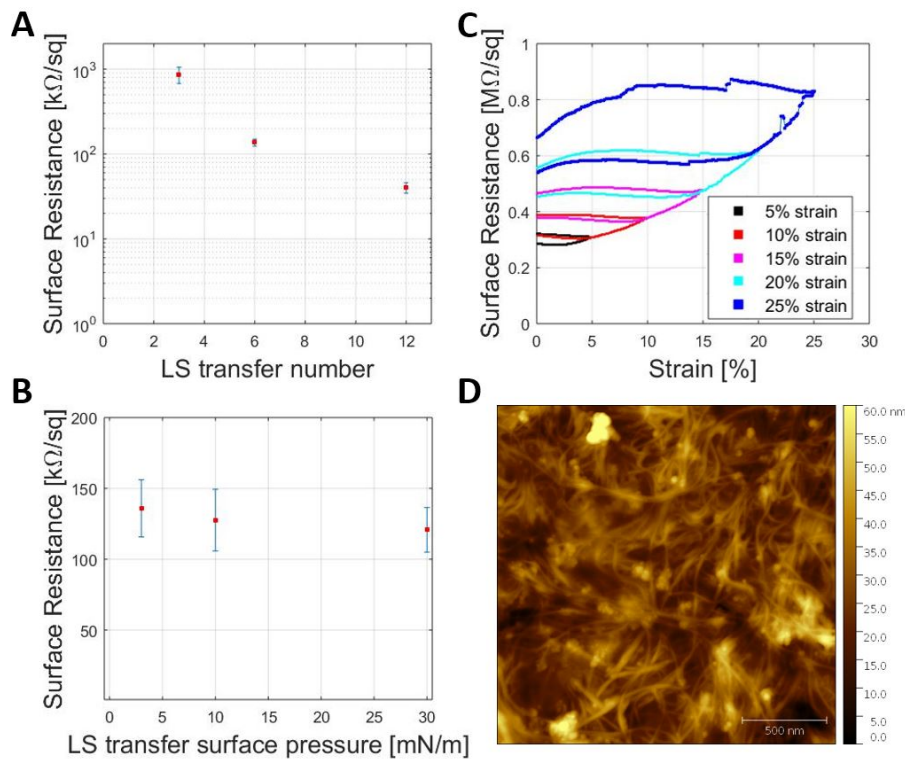
Figure 5.11 Characterization of 2D Langmuir assembled SWCNT-based electrode. (A) Surface resistance vs. number of LS transfers while keeping the LS surface pressure at 3mN/m. (B) Surface resistance vs. LS transfer surface pressure, using 6 LS transfers. (C) Surface resistance vs. linear strain for the electrodes fabricated with 6 LS transfers at 3 mN/m as transfer surface pressure. The surface resistance remains below 1 MΩ/sq at 125% linear stretch. (D) AFM image of the ultra-thin electrode with 6 LS transferred monolayers at 3 mN/m.

The surface resistance vs. strain data (see section 5.5.1) for this electrode is plotted in Figure 5.11C. The ultra-thin electrode keeps almost the same surface resistance up to 5% linear strain.

With increasing strain, the resistance increases. However, even after 25% linear strain, the surface resistance is still less than 1 MΩ/sq.

An AFM image of the ultra-thin stretchable electrode is shown in Figure 5.11D, showing a homogenous interconnected SWCNT network. A few higher spots (brighter regions) can also be seen, which correspond to small aggregates of non-dispersed SWCNTs. The ultrathin electrode meets required electrical, mechanical and surface properties for making stacked DEAs.

In the following section, the developed SWCNT electrode is used to fabricate a stacked DEA. The stacked DEA consists of 3 DE layers sandwiched by 4 electrode layers. The fabrication process is firstly developed. The performance of the stacked DEA is then shown regarding to the DEA strain and speed. The stacked DEA strain is compared with the DEA consisting of reported pad-printed electrodes. Finally, the stacked DEA is compared with other selected soft actuators regarding actuation speed and power density.

5.5.3   Stacked DEA fabrication using SWCNT-based electrodes

With the good SWCNT electrode properties, we developed low-voltage stacked DEAs (LVSDEA) with this electrode, consisting of three DE layers sandwiched by four electrode layers. The LVSDEAs fabrication process are presented in Figure 5.12.

Parts A and B of the PDMS LSR 4305 are mixed with OS-2 (Dow Corning) solvent as described in reference (*144*) in mass fractions of 25 wt%, 25 wt% and 50 wt% respectively using a planetary mixer (Thinky, ARE-250). A 23 µm-thick PDMS membrane is fabricated by casting the uncured PDMS on PET substrate coated with a PAA sacrificial layer, using an automatic film applicator (Zehntner) set to a blade gap of 100 µm. A suspended PDMS membrane is obtained by dissolving the PAA sacrificial layer in hot water. The 23 µm-thick PDMS membrane is then equi-biaxially pre-stretched by the ratio about 2 (see Annex F for why we chose this pre-stretch ratio), reducing the membrane thickness to 6 µm (Figure 5.12A). It is fixed on a custom-made PMMA holder. The pre-stretched PDMS membranes are then used as the dielectric layers of the stacked DEAs.

For LS transferring the patterned electrodes on the PDMS dielectric layers, masks are used. The Oxygen Plasma (OP) treatment needs to be performed only on the bare PDMS zone to ensure good transfer quality. A second sacrificial mask with the same pattern as the mask for the LS transfer is overlapped on the first one for the OP treatment. The second mask protects the first one from OP treatment, as such treatment influences the LS transfer of SWCNTs on the first mask layer. After the OP treatment (Diener, ZEPTO) with 30 W power for 6 s, the second mask is peeled off (Figure 5.12B), and the SWCNT-based monolayers can be LS transferred on the bare PDMS zones with the first mask for the electrode shape patterning. By peeling off the first mask, the suspended PDMS with patterned SWCNTs electrodes is obtained

(Figure 5.12C). The masks are fabricated from 50 µm-thick Polyester sheets, and the mask geometry is cut out using a laser engraving machine (Trotec, Speedy 300).

For more reliable electrical interconnects, a 20 nm-thick gold layer is sputtered on the LS transferred electrodes, with about 3 mm away from the DEA active region, in a shape patterned using the corresponding masks (Figure 5.12D). The masks for gold patterning are made from laser-cut paper. While applying the mask for gold patterning, a 1 mm space gap between the mask and the pre-stretched PDMS membrane is used to avoid direct contact between the two. After the gold layer deposition, the first electrode is finished for the first PDMS layer of the stacked DEA. This PDMS layer is then flipped over to apply the second electrode. This turning over process is done as in Figure 5.8 (E to F), by using PDMS membrane holders with different sizes.

The second electrode is applied as shown in Figure 5.12C. Then the PDMS layer is covered by electrodes on both sides (Figure 5.12E). By sputtering a 20 nm-thick gold layer using a mask on the second LS transferred electrode, the first single layer DEA is completed (Figure 5.12F). Applying of the third DEA electrode onto the second PDMS layer, and fourth DEA electrode onto the third PDMS layer is shown respectively in Figure 5.12G and Figure 5.12H, by repeating the same process as before with suitable masks. Finally, for the LVSDEAs assembly, the three PDMS layers with applied electrodes in Figure 5.12F, G and H, are assembled together on to the frame (Figure 5.12I).
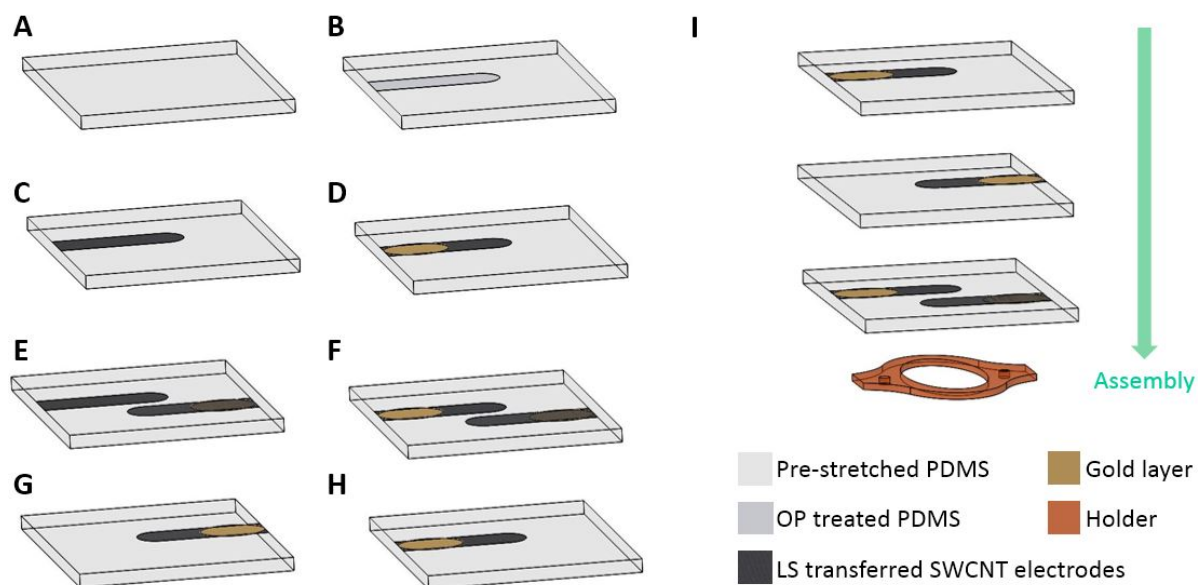
Figure 5.12 LVSDEA fabrication process. (A) 23 µm-thick suspended PDMS membrane equi-biaxially pre-stretched to 6 µm-thick to serve as the first dielectric elastomer (DE) layer. (B) Oxygen plasma (OP) treatment on the suspended pre-stretched first DE layer using a mask. (C) LS transfer of 2D assembled SWCNTs on to OP treated PDMS zone with mask, to serve as the first electrode layer. (D) Deposition of 20 nm thick gold layer on the LS transferred first electrodes with patterned shape by using a mask. (E) LS transfer of second SWCNTs electrode on the backside of first PDMS layer. (F) Applying a gold layer on the second electrode layer. (G) Third electrode on the second DE layer with deposited patterned gold layer. (H) Fourth electrode on the third DE layer with deposited patterned gold layer. (I) Assembly of all the pre-fabricated layers on the holder to make the LVSDEAs.

During the assembly, silicone adhesive is used to ensure the adhesion between the PDMS layers. Conductive silver epoxy drops are applied on each patterned gold layer. After lamination of all layers, fine copper wires are used to puncture through predefined holes on the body frame, and mechanically fixed and electrically connected using silver epoxy. The final assembled stacked layers are vacuum treated to remove any small air bubbles generated during the lamination step. After degassing, the stacked layers are placed in an oven at 80ºC for 2 hours to cure the conductive silver epoxy. The LVSDEAs are then complete.

The above fabricated LVSDEAs is then ready to be characterized regarding to its strain and speed. A single layer DEA with the pad-printed electrodes is also fabricated as in (*144*), to highlight the low stiffness of the LS transferred SWCNT electrodes.

5.5.4   Performance of LVSDEA with SWCNT electrodes

The performance of LVSDEA have been characterized (Figure 5.13). Different single-layer DEAs (see Annex G) have also been prepared to compared their performance with the LVSDEA.
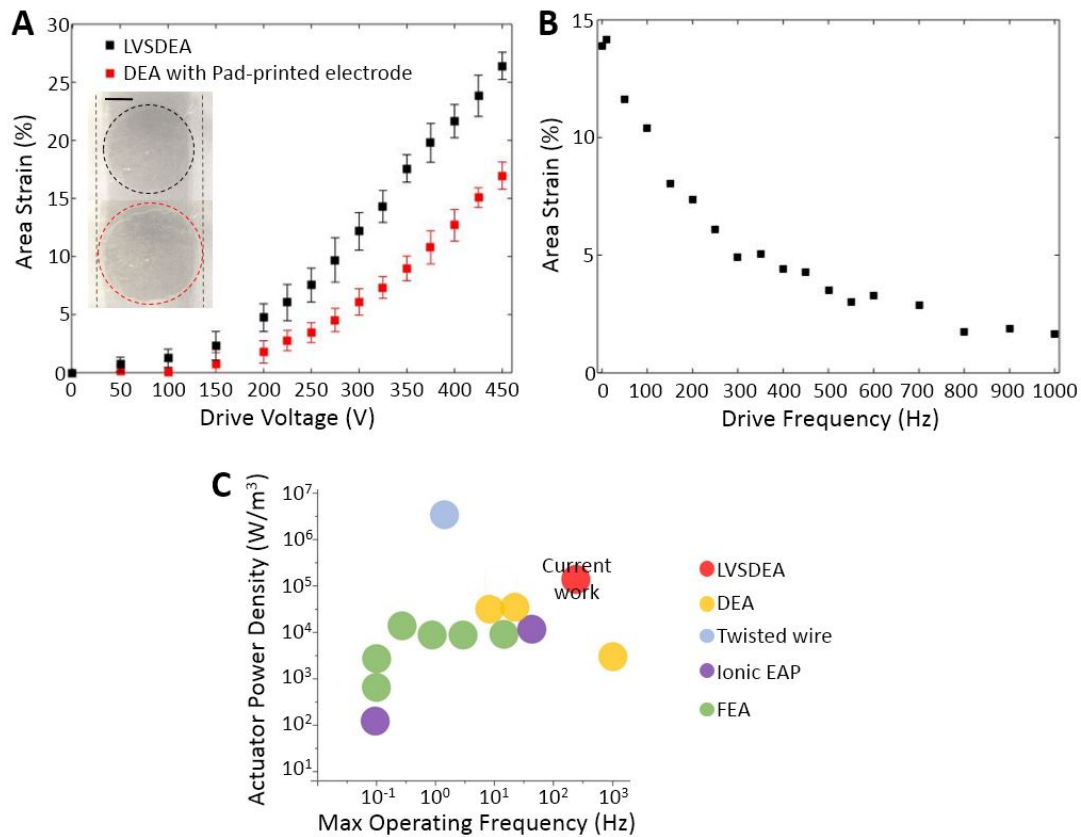
Figure 5.13 LVSDEA performance. (A) Area strain of a 3 mm diameter expanding circle DEAs as a function of the applied voltage, comparing a LVSDEA with a single layer DEA made with our standard carbon-PDMS pad-printed electrodes (*35*). Scale bar 1 mm. (B) LVSDEA strain at 450V vs the driving frequency (square wave driving signal), showing operation over 200Hz. (C) Power density of selected soft actuators as a function of maximum operating frequency. This calculation is for the bare actuators without frames, electronics or compressors. (See Table 5.1)

The low stiffness of the electrode permits the LVSDEA to generate 27% area strain with 450V DC signal (Figure 5.13A), while for the single layer DEA with pad-printed electrodes, the strain is 18% (plots based on one sample for each case). In addition, with this thickness range, the DEAs with pad-printed electrodes cannot fail with a predictable dielectric breakdown field. Several DEA with pad-printed electrodes, fabricated with the same conditions, get breakdown at 400V. Therefore stacked DEA with pad-printed electrodes was not fabricated due to the unpredictable breakdown voltage.

The low surface resistance of the SWCNT-based electrodes permits the LVSDEAs to operate over 200Hz. (Figure 5.13B). Comparing Figure 5.13A and B, the strain values with 450V DC signal are different (from 27% to 14%). This is due to the different dimensions of the images used in both cases (1280x1024 pixels for strain vs drive voltage experiment and 320x240 pixels for strain vs driving frequency curve). The low resolution of the images used for Figure 5.13B is due to the high speed camera.

Our bare LVSDEA alone delivers high power density about $4.5 \ 10^5$ W/m^3 at 200 Hz, see Figure 5.13C. (Table 5.1, detailed calculation see Annex H) Figure 5.13C shows that DEA present the best combination regarding to the power density and working frequency. Compared with other selected DEA examples, our LVSDEA shows the highest power density and is capable of fast operation. Especially, its driving voltage is below 450V, however the others all use several kV for operation.

Soft actuation technology	Maximum power density (W/m^3)	Maximum operating frequency (Hz)	Reference
DEA	$3.0 \ 10^4$	30	(*66*)
	$5.7 \ 10^3$	1000	(*5*)
	$5.6 \ 10^4$	10	(*57*)
	$4.5 \ 10^5$	200	Current work
Fluidic Elastomer Actuator	$1.4 \ 10^4$	1	(*29*)
	$3 \ 10^3$	0.1	(*221*)
	816	0.1	(*10*)
	$1.6 \ 10^4$	5	(*9*)
	$1.8 \ 10^4$	30	(*222*)
	$2 \ 10^4$	0.3	(*223*)
Ionic EAP	140	0.1	(*60*)
	$2.2 \ 10^4$	50	(*61*)
Twisted wire	$4.8 \ 10^6$	2	(*38*)

Table 5.1 Power density of soft actuators capable of generating high output force or capable of fast operation. This data is shown graphically in Fig. 2C. The devices are not operating at resonance.

5.6   Conclusion

The Langmuir-Schaefer method is used for DEAs electrode fabrication for the first time. Multi-walled Carbon Nanotubes and alkyl-polythiophene (MWCNT/PT) are firstly combined to form stable MWCNT/PT composite monolayers at the air-water interface, which then can be transferred onto a PDMS membrane using the Langmuir-Schaefer method. The monolayer electrode consists of an interconnected MWCNT network embedded in a PT monolayer, in which the PT imparts the hydrophobic properties for staying at the air-water interface, while the MWCNTs ensure the electrical conductivity of the system. Using the LS method to fabricate patterned ultrathin stretchable electrodes enables the fabrication of a thin DEA with a 1.4 µm-thick PDMS dielectric membrane. For the first time, with only 100 V, this DEA can reach 4.0% linear strain, correspond to 8% area strain. However, its speed is slow (less than 1Hz), due to the high surface resistance of the MWCNT/PT composite electrode. To increase the operating speed, we improved the properties of the electrodes by fabricating ultra-thin stretchable electrodes using LS method, based on functionalized SWCNTs as conductive materials. In addition, to increase the low-voltage DEA output force, we increased the DE membrane thickness to 6 µm-thick, and then developed stacked DEA.

Compared with the MWCNT/PT system, we decreased the ultra-thin stretchable electrodes resistance by over 2 orders of magnitude. These SWCNT-based electrodes are also stretchable: at 125% linear stretch, the surface resistance is still less than 1 MΩ/sq. They fulfil all the key properties to reach good performance LVSDEAs. The fabricated low-voltage stacked DEA (LVSDEA) with SWCNT electrodes, can output more than 20% area strain with only 450V, and give fast operating of over 200 Hz. The large strain and fast operating speed give the LVSDEA a high power density about $4 \cdot 10^5$ W/m^3. The LVSDEAs represent the best performance DEAs operating below 450V.

The low operating voltage and high power density expand widely the DEA-based applications. We developed untethered soft robot and wearable haptic devices based on these LVSDEAs, which are presented in Chapter 6.

Chapter 6   Soft robotic and wearable haptic devices driven by LVSDEAs

6.1   Summary

In this Chapter, we take the advantage of the sub-450V driving voltage and the high power density ($4.5 \ 10^5$ W/m^3) of the previously developed LVSDEAs (see chapter 5), to develop fully Untethered Artificial Muscle (UnArM) modules. The low driving voltage (below 450V) of LVSDEA allows miniaturized (sub-gram) control and power electronics. By integration of the LVSDEA with the miniaturized driving electronics including battery, sensing and controlling elements, UnArMs are achieved. These sub-gram UnArM modules enable a broad range of untethered soft machines. We demonstrate two developed prototypes based on UnArM modules. The first one is a wearable 20 µm-thick haptic device termed as "feel-through". This device consists of one UnArM module. It can be directly mounted on the fingertip, generating rich notification signals from 1 to 500 Hz. The second prototype is a fast untethered 1 g soft robot, termed as "DEAnsect". DEAnsect is driven by three UnArM modules, capable of autonomous navigation. The high power density UnArMs represent a major step towards autonomous soft mobile machines and wearable human machine interfaces.

6.2   Introduction

By engineering soft matter into actuators, sensors and compliant structures, one can develop wearable devices directly interfaced with the human body, as well as reconfigurable robots that adapt to complex and uncontrolled environments. Recent research advances have produced a broad range of soft robots as described in the previous chapters (Chapter 2 and 3). However, most of these soft machines do not exploit the full potential of soft actuators to be untethered. The low force and power density of most soft actuators results in untethered soft robots with very limited payload carrying ability, to the point that very few soft robots can even carry their own power supply, or suffer from greatly reduced performance when untethered (*224*). The same limitation applies to soft active wearables, whose force must significantly exceed the human perception threshold for effective haptic feedback, and the device volume should be acceptable to wear.

Our previously developed LVSDEAs show high power density (see Chapter 5), which makes it promising to drive untethered systems. We have developed Untethered Artificial Muscles (UnArM) modules based on the LVSDEAs. Each UnArM includes the LVSDEAs, a flexible frame and the power storage, sensing and control electronics on flexible Printed Circuit Board (PCB) (see Figure 6.1).

The core of UnArM modules are the LVSDEAs. Below 500V, there exists a vast selection of low-mass, miniature, commodity surface-mount devices, enabling complex kHz voltage sources weighing only tens or hundreds of milligrams, as shown for instance for piezoelectric flapping-wing robotic insects (*189*, *225*).

Our LVSDEAs enable complete systems exploiting the many advantages of DEAs without the high mass penalty of kV electronics. High energy density soft machines with both embedded intelligence and high performance now become possible.
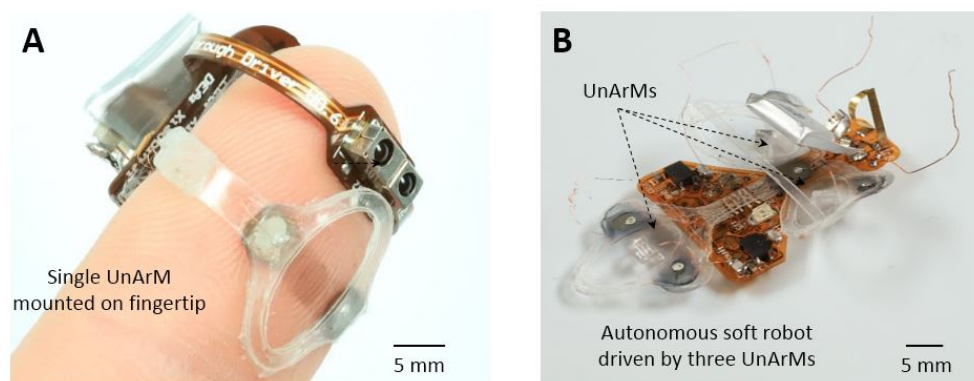
Figure 6.1 Examples of UnArM modules. (A) Photo of one Untethered Artificial Muscle (UnArM) module mounted on a fingertip, used as a "feel-through haptic" device, allowing unimpeded use of the finger while receiving rich localized haptic information (B) Photo of an untethered autonomous robot driven by 3 UnArMs, total mass 970 mg, termed as DEAnsect.

Using a single UnArM module, we demonstrate an on-finger untethered haptic device, termed "feel-through" since its active part is so thin (20 μm) and soft (1 MPa) that it conforms to the

skin (Figure 6.1A). It provides rich localized haptic information by gently moving the skin at frequencies from 1 Hz to 500 Hz. The low-power makes the devices safe; the high stretchability makes the device imperceptible when not actuated, allowing the wearer to perform dexterous tasks, such as writing or fine assembly. This enables many haptic scenarios, from distributed notification to feeling AR/VR objects.

Connecting three UnArM modules with a flexible frame, we demonstrate the first untethered, autonomous insect-size (less than 1g weight, 4 cm-long) soft robot (Figure 6.1B). The integrated sensing and signal processing allow the soft robot to navigate unaided. UnArMs will enable multi-components smart soft machines with a distributed, hierarchical architecture for complex applications. The high power density of LVSDEA allows our key achievements, which are the complete miniaturized untethered systems (soft actuator and all integrated drive electronics).

6.3   Wearable haptic device driven by LVSDEAs

For on-body haptics, the 20 µm-thick LVSDEAs is mounted directly on the body in a format which we call "feel-through" (*226*) given that the device is imperceptible when not actuated. The device complies to the finger shape, allowing unfettered use of the fingertips and fine sensation, yet enabling applying on demand highly localized and rich haptic feedback signals by gently deforming the skin.

6.3.1   Wearable haptic "feel-through" design and working principle

The feel-through active zone is a 3 mm diameter DEA circle with an oval passive zone defined by the flexible holder (Figure 6.2A). When the device is off, the skin is very slightly compressed by the elastomer inside the flexible oval holder. When the DEA is active, the surface area of the elastomer increases, moving the skin (Figure 6.2B).
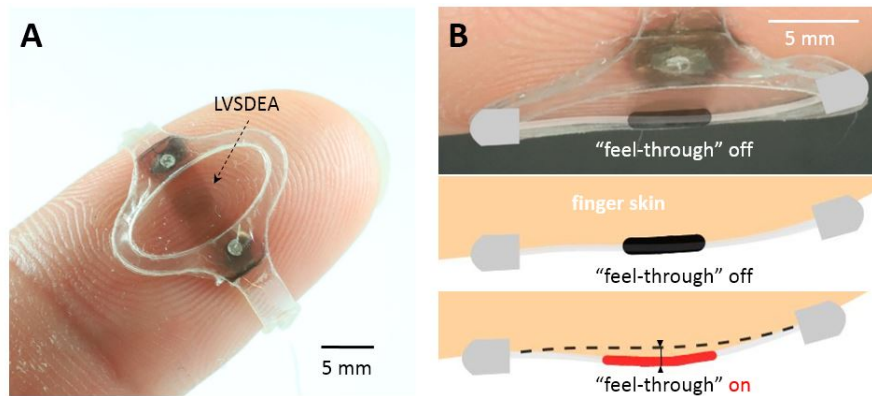
Figure 6.2 "feel-through" design and principle. (A) Photo of "feel-through" on a fingertip, the LVSDEA is a 3 mm diameter circle with oval passive zone fixed in a flexible holder. (B) Top: photo side view of the feel-through haptic device mounted on a fingertip; middle and bottom: cartoon illustrating the working principle: LVSDEA actuates to gently move the finger skin to provide haptic feedback.

6.3.2 "feel-through" haptic devices fabrication

For the fabrication of the "feel-through" device, we follow a similar fabrication process as for the LVSDEA (see section 5.4.3), combined with another additional step: the LVSDEAs are sandwiched between two flexible holders made from laser patterned polyester coated with silicone adhesive. (Figure 6.3) The flexible wires for applying the voltage are embedded inside the flexible holders to avoid direct contact with the skin. The DEA ground electrode is in contact with skin.
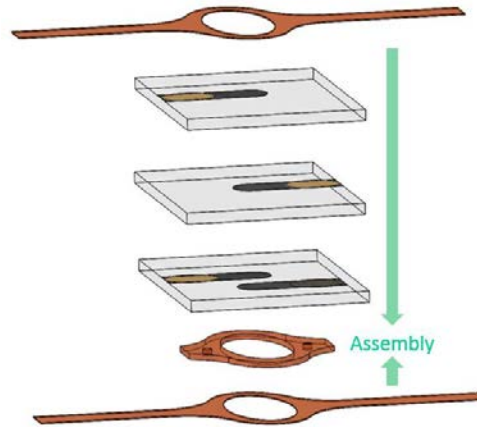
Figure 6.3 "Feel-through" haptic device lamination process. The LVSDEAs are sandwiched between two flexible holders made from laser-cut polyester with coated silicone adhesive, with flexible wires embedded inside the flexible holders.

6.3.3 Tethered "feel-through" haptic devices performance
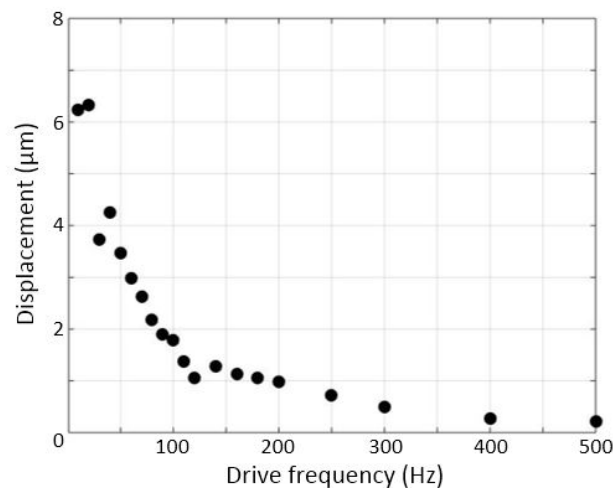
Figure 6.4 Finger skin displacement as function of the drive frequency of the "feel-through" haptic device.

We have measured the skin displacement in the normal direction vs. the driving frequency using a Laser Doppler Vibrometer (Polytec MSV 400). The related data is shown in Figure 6.4. The skin normal displacement (representing the skin movement) depends on drive

frequency, higher frequencies resulting in lower skin displacement. This is in agreement with the LVSDEA strain vs frequency plot presented in Chapter 5 (Figure 5.13B).

6.3.4 "feel-through" test on users: methods and results

Testing methodology for haptic perception on volunteers

14 healthy volunteers (7 female + 7 male, ranging in age from 27 to 46 years) are recruited, and asked to wear the feel-through haptic device on their left index fingertip. The LVSDEAs active zone of the device is located at the center of the fingertip. The user sits in front of a table in a quiet room, and places his/her left arm on the table with the left hand on a soft support (Figure 6.5) so that the user remains comfortable during testing. A computer is in front of the volunteer, who can use his/her right-hand fingers to press keys. Users cannot hear or see any changes in the drive electronics that might give an indication of the applied haptic signal.

Figure 6.5 Photo of the setup for performing user test. "feel-through" mounted on the left hand index fingertip of the user, with the active LVSDEAs zone located at the center of the fingertip. The hand is situated on a support to ensure comfort and stability during the test.

For each volunteer, testing is carried out in two parts:

Haptic test Part 1 (Perceived signal intensity test as a function of frequency):

The aim of this test is to study the perceived intensity of the feedback given by the feel-through devices operating with different frequencies.

The drive signals are given in Table 6.1. The V_{max} stands for the maximum voltage applied on the "feel-through" devices in the corresponding test. We do not use a fixed voltage for all the test, because the devices used for different volunteers are slightly different. Indeed, due to the final PDMS membrane thickness changes in the range of 6-7 µm during the fabrication, the driving voltage of all our fabricated feel-through devices varies from 420 to 440 V. The slight difference in the PDMS thickness changes the exact driving voltage for the DEA to output the same strain. Before starting the experiment, the corresponding driving voltage of the device used in the corresponding experiment is determined. First, three driving signals are sent to the

user, with 420 V as amplitude and 10, 100, and 200 Hz as frequency. The users are asked if they can feel at least one of the signals nicely. If this is the case, then 420V is chosen to be the V_{max}. If the user cannot feel nicely none of the three signals, the voltage is then increased to 430V and the same process is repeated to determine the V_{max}. The process is stopped until 440V as V_{max} is reached. Higher voltages present the risk to induce dielectric breakdown for the DEA.

Signal number	1	2	3	4	5	6	7	8	9	10	11	12
Voltage	0	V_{max}	V_{max}	V_{max}	V_{max}	V_{max}	V_{max}	V_{max}	V_{max}	V_{max}	V_{max}	V_{max}
Fre-quency (Hz)	-	1	5	10	20	50	100	150	200	300	400	500

Table 6.1 Signals used for "feel-through" test Part 1 (intensity test).

An interface is displayed on the screen. When the user is ready for the testing, he/she clicks "start experiment". A random signal from the above 12 signals is applied to the device. The user feels the signal given from the device for at least 2s, then types a number from 0 to 4, corresponding to the perceived signal intensity with:

0: feel nothing

1: difficult to feel

2: can be felt

3: can be felt easily

4: can be felt very easily

Once the user is ready, he/she can press "enter" to start the next signal. Each of the 12 different signals is sent randomly 10 times (in total 120 signals for testing, taking typically about 15 mins to complete the test).

Haptic test Part 2 (Perceived signals recognition test):

The aim of this test is to study the possibility for the users to distinguish and recognize different perceived signals generated by the "feel-through" device. 6 different predefined signals (Figure 6.6), are used in this experiment. The signals are chosen to cover different frequency ranges. The users attempt to identify them.

A testing interface is displayed on the computer. When the user is ready for the testing, the user clicks "start learning" on the interface to experience the stimuli corresponding to the 6 signals. By typing a number from 1 to 6 and pressing "enter", the corresponding signal is sent to the haptic device, with the signal number displayed on the computer screen. The users practice

freely until they have learned all the 6 signals. An information sheet with the waveform of the 6 signals (Figure 6.6) is available for helping the users to remember the signals.

Once the user is ready, he/she can stop learning by clicking "Abort learning" and start the experiment by clicking "Start Experiment" on the interface.
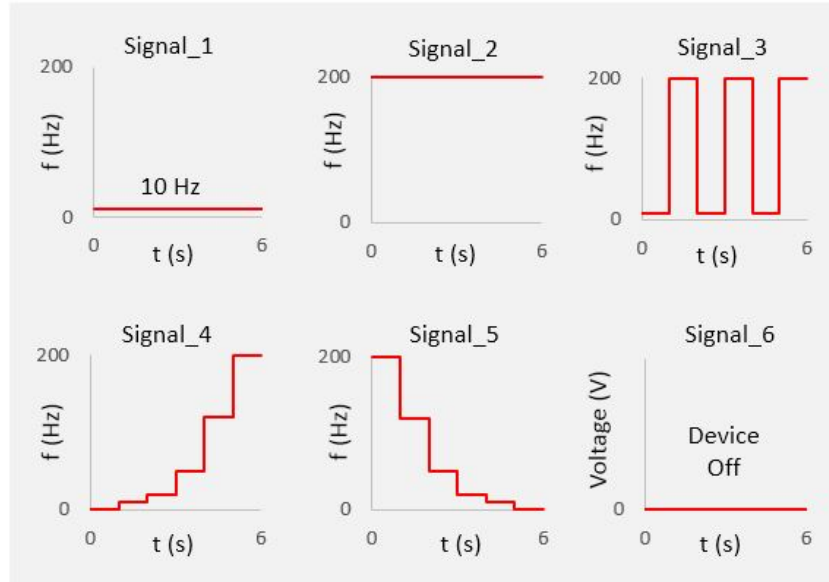
Figure 6.6 Waveform of the 6 signals used for haptic pattern recognition.

A random signal from the predefined 6 signals is sent to the haptic device. The user feels the signal for at least 6s, then inputs the number corresponding to the signal he/she has identified based on the learning part. Then user presses "enter" to validate the input number and once ready, he/she can press "enter" again to start the next signal. The users have noticed that the overall intensity of the feedback signals seem to decrease with the test time increasing. The hypothesis is that: the sensitivity of the cutaneous mechanoreceptors on the fingertip decreases with the test time increasing and their sensitivity may also get lost because of keeping the same gesture for long time. Therefore breaks are taken (generally very short, less than 1 min) to recover the sensitivity of the cutaneous mechanoreceptors. Each of the 6 different signals is applied randomly 10 times (in total 60 signals for testing, taking typically about 40 mins to complete the test).

"Feel-through" device user test data and analysis

As described in the methods section, we recruited 14 volunteers. Complete experiments have been taken for 11 of the 14 users due to a device failing during testing, a change in test procedure, and a medical condition for one user.

From the data for part 1 of the haptic tests, all users easily feel some frequencies and some users reported easily sensing the entire frequency span. Each individual user has his or her characteristic sensitivity for this test. Data from four tested users representing their different sensibilities are given in Figure 6.7. For the test part 2, we report the confusion matrices (Figure 6.8) for the four users whose data of test part 1 are given in Figure 6.7. The corresponding

confusion matrix based on 11 volunteers is given in Figure 6.9. Users identify signals 1, 2, 3 and 6 easily, with an identification rate (IR) of over 85%. For the similar signals 4 and 5, the identification rate is over 70%.
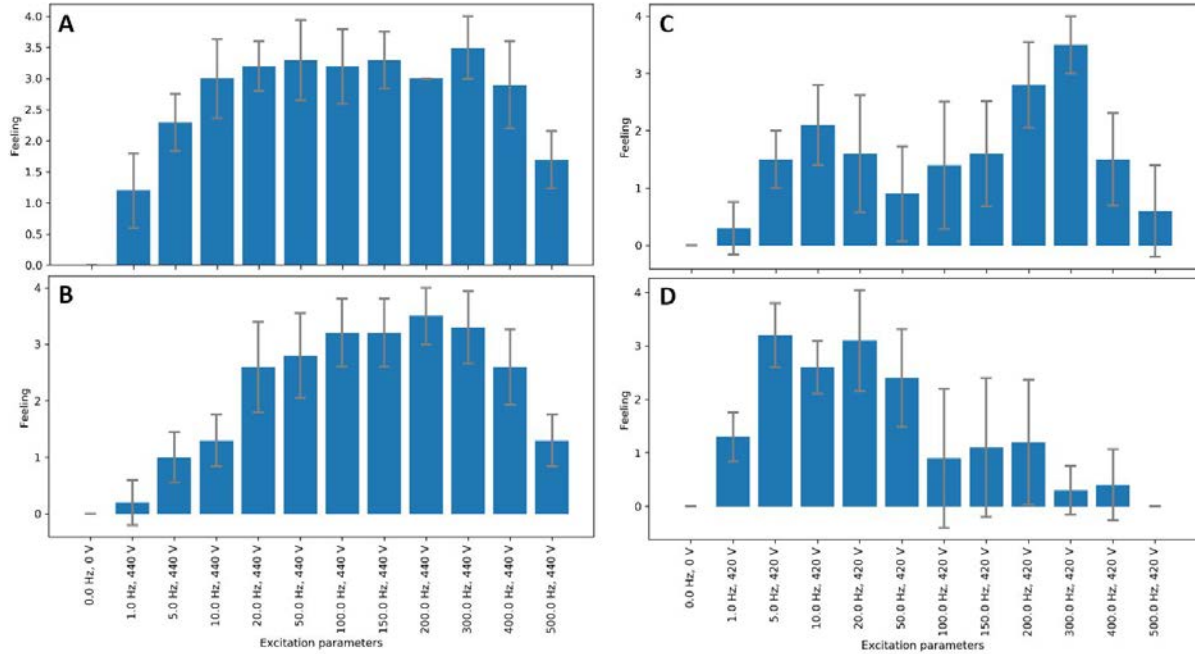
Figure 6.7 Data from 4 users from the "feel-through" Part 1 user test, showing four typical types of sensitivity behavior. (A) This user perceives a wide frequency range from 10-400Hz. (B) This user perceives better signals between 100 Hz and 300 Hz. (C) This user perceives best signals of two frequency bands, one around 10 Hz and one around 300 Hz. (D) This user perceives only at low frequencies below 20 Hz.

A

Response / Stimuli	Signal 1	Signal 2	Signal 3	Signal 4	Signal 5	Signal 6
Signal 1	100%	0%	0%	0%	0%	0%
Signal 2	0%	100%	0%	0%	0%	0%
Signal 3	0%	0%	100%	0%	0%	0%
Signal 4	0%	0%	0%	100%	0%	0%
Signal 5	0%	0%	0%	0%	100%	0%
Signal 6	0%	0%	0%	0%	0%	100%

C

Response / Stimuli	Signal 1	Signal 2	Signal 3	Signal 4	Signal 5	Signal 6
Signal 1	80%	0%	0%	0%	0%	20%
Signal 2	0%	100%	0%	0%	0%	0%
Signal 3	10%	0%	90%	0%	0%	0%
Signal 4	0%	0%	10%	50%	40%	0%
Signal 5	0%	10%	0%	50%	40%	0%
Signal 6	0%	0%	0%	0%	0%	100%

B

Response / Stimuli	Signal 1	Signal 2	Signal 3	Signal 4	Signal 5	Signal 6
Signal 1	100%	0%	0%	0%	0%	0%
Signal 2	0%	100%	0%	0%	0%	0%
Signal 3	0%	0%	100%	0%	0%	0%
Signal 4	0%	0%	0%	90%	10%	0%
Signal 5	0%	0%	10%	0%	90%	0%
Signal 6	0%	0%	0%	0%	0%	100%

D

Response / Stimuli	Signal 1	Signal 2	Signal 3	Signal 4	Signal 5	Signal 6
Signal 1	60%	20%	20%	0%	0%	0%
Signal 2	10%	50%	0%	0%	0%	40%
Signal 3	0%	0%	80%	20%	0%	0%
Signal 4	20%	10%	0%	50%	20%	0%
Signal 5	0%	10%	10%	30%	40%	10%
Signal 6	0%	30%	0%	0%	0%	70%

Figure 6.8 Confusion matrices of the "feel-through" Part 2 users test for the same four users whose Part 1 data is shown in Fig. 6.7.

In general, regarding to the two parts of test, the users who easily perceive a broad range of frequencies in Part 1 (Figure 6.7) have very high accuracy in signal identification. Users who

do not feel certain frequency bands are less accurate. The results from test Part 1 and 2 demonstrate that LVSDEAs are effective at delivering some on-body notifications.

Based on the user test results, our "feel-though" device can generate perceptible signals with different operating frequencies. Combining signals with different frequencies can lead to much more versatile feedback. The arrays of DEAs can be used for mixed and augmented reality scenarios, allowing users to feel virtual objects.

Feedback / Stimuli	Signal_1	Signal_2	Signal_3	Signal_4	Signal_5	Signal_6
Signal_1	85%	3%	4%	3%	0%	5%
Signal_2	4%	89%	1%	0%	1%	5%
Signal_3	3%	0%	87%	7%	2%	1%
Signal_4	1%	5%	5%	74%	13%	2%
Signal_5	0%	5%	5%	15%	73%	2%
Signal_6	0%	3%	0%	0%	0%	97%

Figure 6.9 Confusion matrix showing the average response of 11 untrained volunteers to the 6 stimuli signals delivered to a single wired LVSDEA mounted on the left index fingertip, showing very high correct identification rate, validating a range of notification scenarios

6.3.5 Untethered "feel-through" demonstration
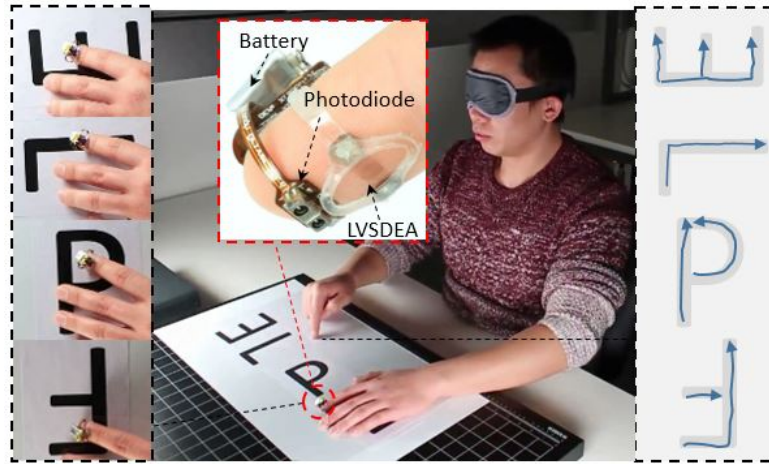
Figure 6.10 Untethered version of the feel-through haptic device demonstration. The device is programmed to deliver 200 Hz vibration when on black regions. The blindfolded user correctly identifies randomly rotated and placed letters E, P, F, and L.

Miniaturized control electronics are developed by Dr. Xinchang LUI in the EPFL-LAI (see Annex I). The microcontroller uses photodiodes as sensory input, giving the device basic intelligence, implementing a finite state machine structure for feedback control. We illustrate one use-case of the haptic device (on one user) in an untethered "feel-through" scenario. Based on the input from the photodiodes, the device is programmed to give vibrotactile feedback when it is on a black surface, and to remain off when on a white surface. The feel-though haptic device is mounted on a fingertip, which the blindfolded user freely scans over a flat and smooth

plastic plate under which randomly oriented E, P, F and L letters have been placed. The users correctly identified both position and orientation of the letters. (Figure 6.10)

The feel-through device shows the possibility to allow users to "see" the color with the finger-tip. This corresponds to an additional sensation which we normally cannot access with the touch sense organs. By using other types of suitable sensors on the device, the "feel-though" is also possible to allow the user to "touch" sound and smell.

6.4   Soft robots (DEAnsect) driven by LVSDEAs

We further used three LVSDEAs to drive an insect robot, termed "DEAnsect". In this section, the DEAnsect design and operating principle are firstly discussed. The DEAnsect robot performance is then characterized. Further, untethered DEAnsect driven by three UnArMs is developed, which is capable of autonomously navigation.

6.4.1   DEAnsect designs and working principle
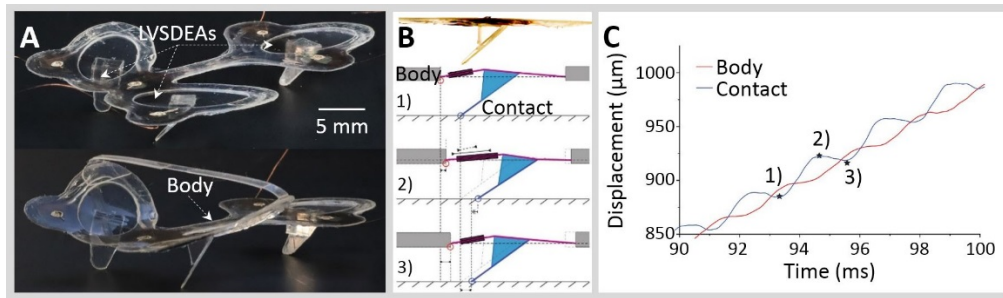
Figure 6.11 Soft robot (DEAnsect) design and moving principle. (A) Top: Photo of flat (as fabricated) DEAnsect robot; bottom: DEAnsect with body held in bent shape using tape to increase the stiffness of the whole structure for increased load capacity. (B) Schematic cross-section of one leg and DEA, illustrating the motion principle. (C) Plot of robot body and leg contact displacement as function of time extracted from high speed camera video.

The DEAnsect is a 35 mm-long robot, with 3 legs, each driven by an independent LVSDEA, each 3 mm in diameter and 20 µm-thick. Two body shapes are studied in this work: fist, DEAnsect with flat body (as fabricated) (Figure 6.11A up); second "DEAnsect" in bent shape to increase the global structure stiffness for higher load capacity (Figure 6.11A down). DEAnsect is fully mobile in both configurations. Without the electronics, the bare robot mass is 190 mg.

The DEAnsect motion principle is illustrated as following after it achieves steady moving state. Using angled legs, the DEAnsect exploits asymmetrical friction forces to move forward. For each cycle, the DEAnsect leg is described by three steps in Figure 6.11B: 1), 2) and 3). From step 1) to 2), the DEAnsect leg is pushed forward when the LVSDEA expands. The robot body also moves forward slightly due to the inertia. Following the LVSDEA contraction from step

2) to 3), the leg contact stays almost static due to the static friction, while the LVSDEA contracts, pulling the robot body forward. With motion recorded using a high-speed camera, the DEAnsect body and leg displacement vs. time is plotted in Figure 6.11C, with the moving steps corresponding to Figure 6.11B marked on the plots. The average forward step is 40 µm, corresponding to a forward speed of 18 mm/s.

6.4.2   DEAnsect and fabrication
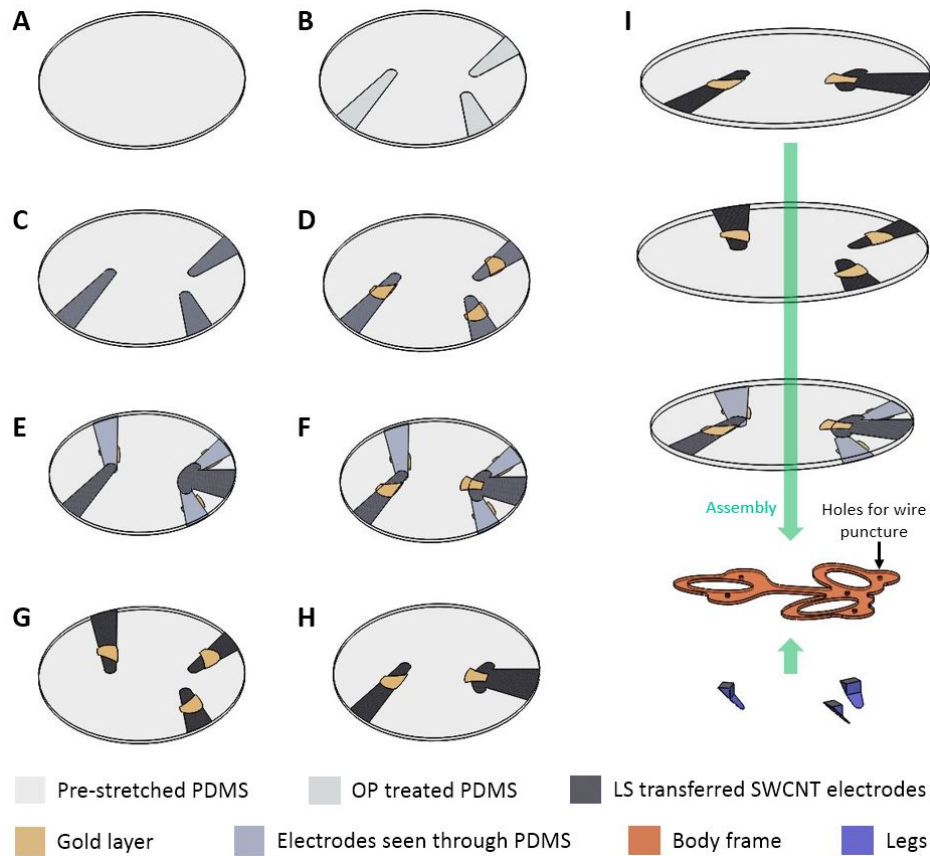
Figure 6.12 DEAnsect soft robot fabrication process. (A) 23 µm-thick suspended PDMS equi-biaxially pre-stretched to 6 µm thickness to serve as the first dielectric elastomer (DE) layer. (B) Oxygen plasma (OP) treatment on the suspended pre-stretched first DE layer using a mask. (C) LS transfer of 2D assembled (6 times) SWCNTs on to OP treated PDMS zone with mask, to serve as the first electrode layer. (D) Deposition of 20 nm-thick gold layer on the LS transferred first electrodes with shape patterned by using a mask. (E) LS transfer of second SWCNTs electrode on the backside of first PDMS layer. (F) Application of a gold layer on the second electrode layer. (G) Third electrode on the second DE layer with deposited patterned gold layer. (H) Fourth electrode on the third DE layer with deposited patterned gold layer. (I) Lamination of all the pre-fabricated layers on the DEAnsect body frame. The robot legs are assembled from laser cut PET and PMMA parts. Then three legs are mounted beside each LVSDEA to finalize the DEAnsect.

For the fabrication of the "DEAnsect" robot, we follow a similar fabrication process as for the LVSDEAs (see section 5.4.3) with appropriately-shaped masks and holders for the desired pattern. (Figure 6.12)

The legs of the DEAnsect robot are composed of laser cut PET and PMMA (connected by ARclear adhesive). The leg assembly is mounted to the passive membrane in close proximity

to the DEA active zone (as show in Figure 6.11A and B; and Figure G1A insert photo for top view).

6.4.3   Tethered DEAnsect performance

The DEAnsect leg displacement as function of the driving frequency of one DEAnsect leg is given in Figure 6.13. The experiment is performed by raising the DEAnsect body off the moving surface, while keeping the DEAnsect body parallel. With the driving frequency increase, the leg displacement decrease in general, because the LVSDEA is limited by its response time. However two leg displacement peaks are found, which is due to the amplification of displacement by the resonance of the leg-DEAs system. The two peaks may relate to two different resonance modes of the system, whose understanding needs further study. From the Figure 6.13, the peak at 580 Hz presents the best leg displacement.
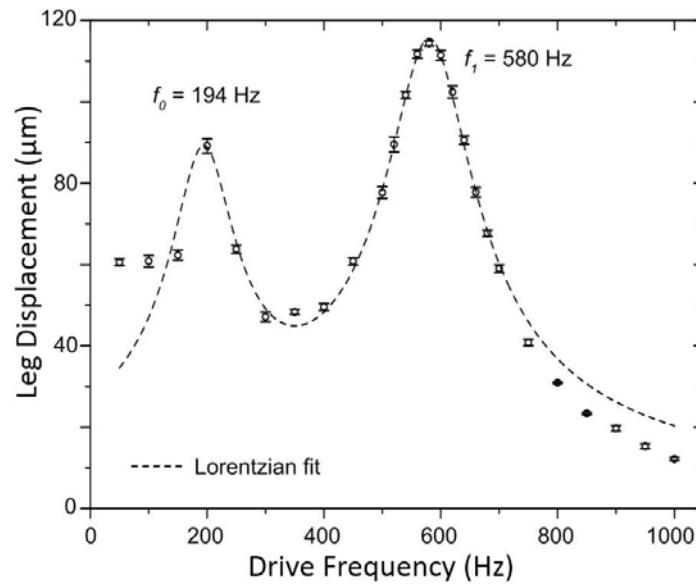
Figure 6.13 Robot leg displacement vs. driving frequency when the leg is not in contact with moving surface. The in-plane motion of the soft robot leg driven by a LVSDEA, showing operation up to 1 kHz, with two resonance peaks.

The speed of the DEAnsect is analyzed with regard to the following aspects: 1) robot speed vs. the frequency of the driving signal; 2) robot speed vs. the driving voltage amplitude; 3) robot speed on different surfaces with differing friction constants; 4) robot speed vs. different carrying weight.

The DEAnsect speed is plotted as function of the driving frequency in Figure 6.14A. The DEAnsect is with the flat shape, as shown in Figure 6.11A top. The drive voltage is fixed at 450 V, while the driving frequency varies from 50 Hz to 1 kHz. Two peaks can be seen in speed vs frequency curve, at around 150 Hz and 450 Hz. They correspond to two resonance modes of the system, as seen in Figure 6.13. At 450 Hz, the robot travels at a speed of 18 mm/s (40 µm/period). The DEAnsect speed is also plotted as function of the driving voltage as shown in Figure 6.14B. The driving frequency is fixed at 450 Hz, but the driving amplitude varies from 250 V to 450 V. The robot starts moving at around 300 V. With the voltage amplitude increasing, the robot speed increases almost linearly (0.11 mm/s/V). The robot speed can thus

be controlled by tuning the applied drive voltage. Maximum velocity of 18 mm/s is obtained with a drive amplitude of 450 V at 450 Hz.
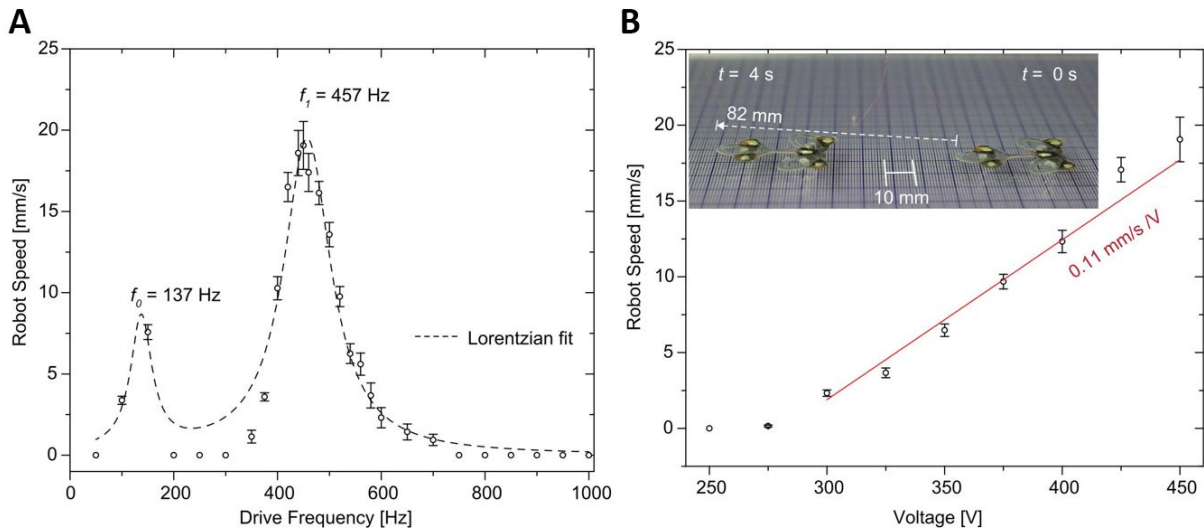
Figure 6.14 DEAnsect speed as function of driving frequency and voltage. (A)DEAnsect speed vs. drive frequency. With driving voltage of 450V, DEAnsect presents two speed peaks corresponding to resonances at 137 Hz and 457 Hz. At 450 Hz driving frequency, the non-deformed DEAnsect present the best moving speed of 18 mm/s (B) DEAnsect speed vs. drive voltage at resonance frequency (450 Hz). The robot speed can be controlled by turning the driving voltage (approximately 0.11 mm/s/V with linear fit).

The effect of different surfaces on the robot velocity is summarized in Table 6.2. Four types of surfaces are tested: PMMA, Polyester sheet, office paper and sandpaper (grit P2500). The DEAnsect is with non-deformed body, as shown in Figure 6.11A top. The driving signals is fixed to 450V with 450Hz. On PMMA, the bare robot shows the fastest speed (19 mm/s). When the surface roughness increases, the robot speed decreases (12 mm/s for paper surface). If the surface is too rough, as observed with sandpaper, the robot stops moving.

Materials surface	Soft robot speed (mm/s)
PMMA	19 ± 1.5
Polyester	14 ± 0.5
Paper	12 ± 0.8
Sand Paper P2500	0

Table 6.2 Bare DEAnsect robot speed on different materials surface.

Robot speed as function of the carrying weight is summarized in Table 6.3. A Polyester surface is used for this characterization, because the robot present the best moving speed on this surface when loaded with weight. The PMMA surface do not give the best robot speed anymore when the robot carries extra load.

Load (mg)	Soft robot speed (mm/s)	Resonance frequency (Hz)

0	29.8 ± 1.8	450 ± 10
275 ± 2	22.7 ± 2.6	430 ± 10
450 ± 4	16.1 ± 1.4	420 ± 10
550 ± 6	14.7 ± 0.4	400 ± 10
650 ± 8	12.9 ± 1.8	395 ± 10
750 ± 10	11.7 ± 2.3	390 ± 10
850 ± 12	10.8 ± 1.6	380 ± 10
950 ± 14	6.6 ± 1.9	365 ± 10

Table 6.3 Bare DEAnsect (deformed body) speed vs. load for a drive voltage of 450V.
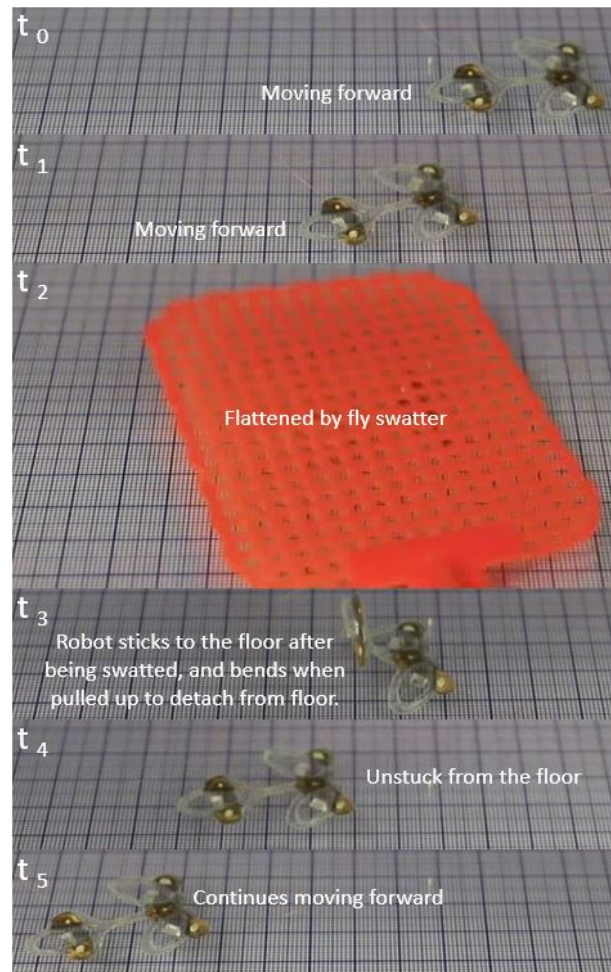
Figure 6.15 Robust DEAnsect continues moving after flapped by a fly swatter.

To carry additional weight, the robot is slightly bent using tape, as shown in Figure 6.11A (down). By increasing the contact angle of the two legs at the back, the stiffness of the whole

robot structure increases, and the robot's load carrying capacity increases. Indeed, without deformation, the robot can carry up to a 700 mg load. With deformation, it can carry 950 mg, which is 5 times of its own weight (190 mg). When deformed, the speed with 0 mg load almost doubled, from 18 mm/s to 30 mm/s. With added load, the DEAnsect speed as well as the driving frequency decreases, as the load changes the resonance frequency of the system (Table 6.3). The step size is reduced with increasing load.

The DEAnsect is extremely robust: after being completely flattened by a fly swatter, it can be peeled off the moving floor, and continues moving forwards (Figure 6.15). This resilience and ability to sustain very high deformation is a core advantage of soft robots.

6.4.4 Untethered autonomous DEAnsect demonstration

The miniaturized control electronics are developed to fit within a mass budget of 800 mg, including the rechargeable battery (Annex I). The on-board electronics is developed by Dr. Xinchang Lui from EPFL-LAI.

Fabricated on a flex-PCB, running of a 3.7 V battery, the control electronics has two independent channels, each with independent waveforms at up to 480 V and 1 kHz, with amplitude and frequency dynamically set by the microcontroller.

By controlling the two channels independently with the integrated microcontroller (see Annex I), the robot can achieve turning. We define channel 1 as front leg plus left leg; and channel 2 as front leg plus right leg. Therefore, when only channel 1 is on, the DEAnsect turn right. When only channel 2 is on, the DEAnsect turns left. When both channel 1 and 2 are on, the DEAnsect move straight forward.
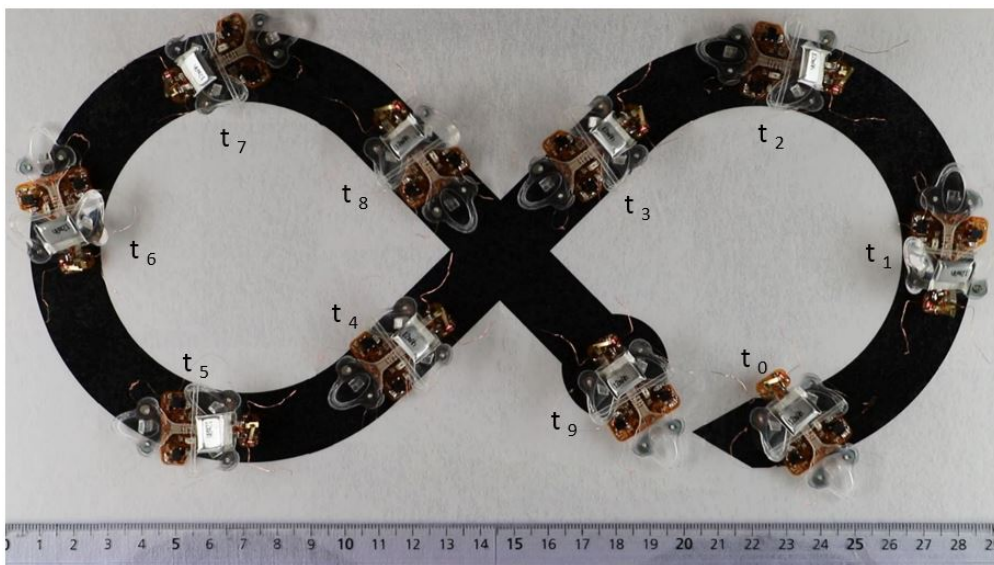
Figure 6.16 Integrated with the control electronics, the untethered DEAnsect autonomously navigates a figure-"8" path, and automatically stops at the end of the path. Ruler scale is in cm. Total elapsed time from t_0 to t_9 is 65 s

The microcontroller also uses photodiodes as sensory input, giving the robot basic intelligence, implementing a finite state machine structure for feedback control: the untethered integrated DEAnsect autonomously navigates a figure "8" as shown in Figure 6.16, automatically coming to a stop at the end, illustrating the potential to make smart untethered robots based on DEAs.

6.5 Conclusion

In this chapter, we have shown Untethered Artificial Muscle (UnArM) modules based on LVSDEAs that operate at both high speed (over 200 Hz) and low-voltage (sub-450V), with high power densities, enabling a broad range of wearable and soft robotics applications that today are excluded due to the bulk of power supplies. The low driving voltage of LVSDEA allows for miniaturized control electronics, with a mass reduction of several orders of magnitude, and thus enabling high-performance untethered operation of soft machines using artificial muscles. We have illustrated two prototypes driven by UnArMs. The first is an untethered autonomous DEAnsect robot. The DEAnsect is fast, with moving speed of 18 mm/s for flat body and 30 mm/s for bended body; DEAnsect is robust, which can sustain strong flattening by fly swatter and keep functionality; DEAnsect is strong, with a body weight of 190 mg, capable of carrying 950 mg load and moving forward. The high load capacity of DEAnsect enables the integration of 770 mg on-board power and controlling electronics to develop the autonomous untethered DEAnsect. For the first time, small scale (1 g, 4 cm-long) untethered autonomous robot driven by DEAs are capable of autonomous navigation. The second prototype is an untethered wearable haptics device "feel-through". The haptic device is compliant so that it can adapt the fingertip form. Its active zone is a 3mm-diameter circle with thickness of only 20 µm. The thin active membrane allows the finger for free use while wearing the haptic device, and the mechanoreceptors covered by the device can remain sensitive to feel through the device. It can generate rich notification signals with wide frequency range from 1-500 Hz. The low-voltage enables untethered "feel-through" haptic device with total weight about 1 g. We demonstrated that the untethered "feel-through" can give user augmented sensation, which allows the user to "see" letters using fingertip. We anticipate these results will enable much broader use of stretchable DEAs for soft exoskeletons, autonomous soft robots, wearables and haptic interfaces.

Chapter 7   Conclusion

The goal of this thesis is to decrease the DEA driving voltage. The approach to achieve this goal is decreasing the dielectric membrane thickness. Decreasing the dielectric elastomer thickness adds much more critical conditions to the DEA electrodes compared with the ones used for thick DEAs.

Therefore, the research activities were conducted by developing the DEA novel electrode materials and related fabrication technologies to meet all the critical requirements needed by the low-voltage DEAs. Two approaches were taken during this thesis:

> ➢ First approach: developing extremely soft and thin stretchable ionic electrodes.

> ➢ Second approach: developing ultrathin stretchable non-ionic electrodes with Langmuir monolayer method.

In the following section, the achieved results are firstly summarized. Then corresponding possible future works are proposed for all the achieved results.

7.1   Summary

List of achieved results during this thesis work:

- The main contribution: we decreased the driving voltage of DEA by one order of magnitude, from the general value of several kV, down to below 450V. And developed microfabrication process for making high performance low-voltage stacked DEAs (LVSDEA).

- We developed extremely soft and transparent ionogel as DEA electrodes. By 3D patterning the ionogel into an optical grating element, a DEA driven soft transparent tunable transmission grating was developed.

- We fabricated single layer DEA that produce 8% area strain with only 100V driving voltage.

- We developed nm-thick stretchable conductors using Langmuir monolayer method. The electrode has a surface resistance of 0.2 MΩ/sq, which enables the fabricated LVS-DEA for fast actuation. This high performance of the electrodes sets the high performance of LVSDEAs.

- We developed novel soft robots "DEAnsect" driven by LVSDEAs. The DEAnsect is fast (18 mm/s), robust (continue moving after being flattened by fly swatter), strong (load capacity: 5x bodyweight) and steerable.

- We developed novel "feel-through" haptic devices by applying the LVSDEA directly on the fingertip skin, capable to generate notification signal from 1 Hz to 500 Hz.

- We integrated the LVSDEA with all the auxiliary support systems including sensing, control and power elements, and developed small-scale (cm^3) and lightweight (1g) Untethered Artificial Muscle (UnArMs) modules. Applications of untethered autonomous soft robots (capable autonomously navigate complex path) and untethered wearable haptic devices (capable of help the use to "see" letters using fingertip) were developed based on UnArMs.

The high power density UnArMs represent a major step towards autonomous soft mobile machines and wearable human machine interfaces. UnArMs contribute to the development of real-word applications using DEA-based technologies.

The achievements of this thesis can benefit the whole DEA fields, and bring the DEA-based applications, especially wearable haptic devices, closer to the customers.

In the following section, we propose the possible related future works based on the achieved results from this thesis work.

7.2 Future work

Future work related with ionogel electrode

- **Solving ion migration problem**. The ion migration is a common problem for DEA devices using ionic-based conductors as electrodes, or for DEA applications in ionic environment. Future works should be addressed to limit the ions to migrate into the dielectric elastomer. One approach could be adding additional protection layers on the DE to prevent or slowdown the ion migration speed. But this approach is only a halfway solution and also adds stiffness on the DE. Another approach may be more challenging, but may be possible to solve the problem primarily. I propose here to develop DE materials with super-hydrophobic properties, where the energy need to break the equilibrium between the ions and the super-hydrophobic materials is more than what the ions obtain under electric field. Here, two possible approaches are proposed. The first one is to physically blend super-hydrophobic micro-particles inside the DE. The second is to chemically bond super-hydrophobic side chains on the DE polymer main chain.

- **Transparent tunable micro-lens array.** Micro-lenses can be used to collect the scene information in tiny versions. With an array of micro-lenses, each micro-lens is with a different angle and position. Therefore, the scene can be reproduced with parallax to reproduce 3D images. It is promising to pattern the transparent ionogel into curved micro-lens array for developing tunable transparent micro-lenses array driven by DEAs. The patterning can be performed by using a mold as the case for the developed tunable grating in the thesis work. Or the curved lens structure can be directly 3D patterned by inkjet printing, because the droplets formed could be used as micro-lenses.

- **Invisible soft robots and wearable devices.** The ionogel electrodes are highly transparent (93% transmittance). Transparent DEAs can be used to drive soft robots and wearable devices. The transparency can add the invisibility on the devices to increase the functionality.

Future work related with Langmuir ultrathin electrode

- **Nanometer-thick stretchable conductor with increased conductivity.** More conductive materials (e.g. Silver Nanowires, AgNWs) should be used to form nanometer-thick stretchable DEA electrodes with Langmuir method. The mechanical properties should be studied as function of the fabrication conditions. Such as the LS transfer pressure as function of the stiffness of the formed ultrathin layer. Ideally, it is possible to achieve high performance electrodes which are conductive (sheet resistance less than 3 kΩ/sq), thin (less than 20 nm) and soft (less than 1 MPa). With these electrodes, the DEA with 1 cm^2 active area, and PDMS dielectric thickness of 100 nm, is promising to be developed. The DEA will be possible to operate with 10V and with a RC time constant of only 1 ms. A stack of such DEAs will further enable more applications. This is very challenging work, but promising. The electrode properties are the key elements to achieve this goal. For the AgNWs, the typical diameter of the nanowire is around 20 nm, which means the AgNW monolayer should be fabricated to achieve the 20 nm DEA electrode thickness. However, with simply a monolayer, the electrode stretchability may get degraded. In addition, nanoparticles always form aggregates. With a thin dielectric layer of 100 nm, the aggregates may possibly cause the stacked DEA to fail with unpredictable breakdown field.

- **Automated multilayer fabrication process for low-voltage DEAs.** As reviewed in Chapter 3, no automated multilayer DEA construction process has been reported for stacked DEAs with driving voltage below 500V. In this thesis work, the stacking method enable 3-layer DEA devices to operate below 450V. However, when the stacking layer number is increased, the current stacking method cannot work properly anymore. The lamination for each layer will be difficult due to the interlayer adhesion step. Automated multilayer construction should be developed. The Langmuir technology is suitable for making electrodes for multilayer DEAs, due to the capability to fabricate homogenous nm-thick layers. To achieve low-voltage DEAs with more stacked layers, an automated roll-to-roll multilayer fabrication process is proposed in Figure 7.1. In this process, the electrode is fabricated by Langmuir method, and the

dielectric layer is fabricated by solution coating on the substrate. For the deposition of electrode, the surface tension between the right roll and the barrier of the Langmuir trough is kept as constant. The speed of the rolling is thus controlled. For controlling the thickness of the PDMS dielectric layer, the concentration of the precursors solution can be controlled. At the top side, the PDMS precursors could be cured after coated on the substrate by UV lamp. This proposition is just a simplified illustration for this idea. Much detailed works need to be considered for using this approach, including electrode patterning, dielectric membrane pre-stretch and inter-layer electrode connection.
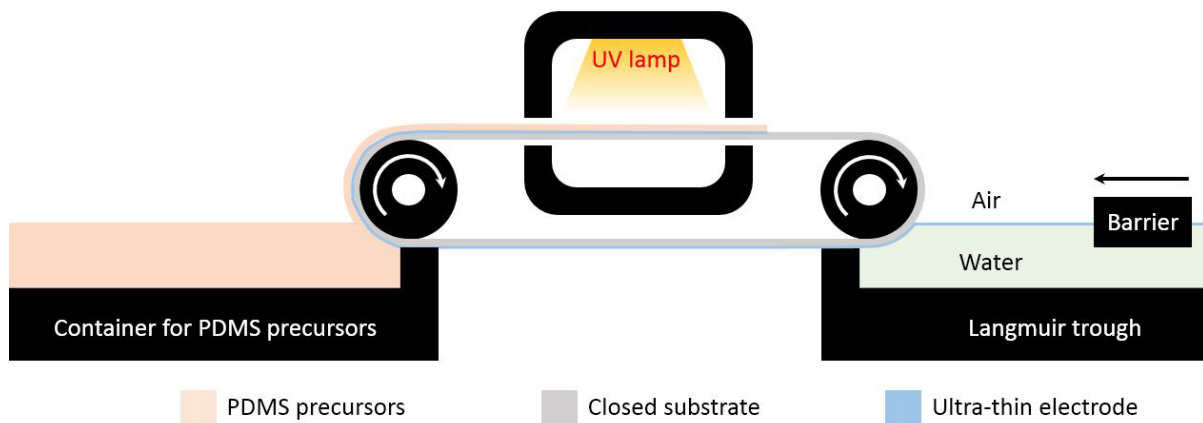
Figure 7.1 Simplified illustration of multilayer DEA fabrication by roll-to-roll process.

- **Wearable haptic device array.** Regarding to the developed "feel-through" haptic devices, a larger array could deliver much richer feedback signals than a single DEA. The DEA array shown in Figure 7.2 is an array of single layer DEAs. It shows the possibility to develop a multilayer DEA array with the developed fabrication process. More stacked layer could increase the device output force, so that the feedback signals driven by any frequency can be easily perceived by the users. Complexed pattern of the array is promising to be developed to cover different body parts. Such as a haptic glove to cover the whole hand.

- **Soft robots improvements.** For the soft robot "DEAnsect", the future work could be addressed to improve the robot performance, including the load capacity and speed. The DEAnsect can't move on rough surfaces such as sandpaper for this moment. To improve the performance, the robot should be designed to generate bigger walking gait so that it can go cross the obstacles. Adding extra muscle parts in the robot design is also promising, so that the soft robot should be capable of changing its body shape to go through limited structures. This behavior will evidently show the advantages of being soft (multi-degree of freedom). For the untethered soft robots, the robot control electronics should be further decreased in size and weight, to improve the performance of the untethered robot. This returns to the basic goal of reducing the DEA driving voltage. Further improving the DEA power density, and decreasing the driving voltage are the key elements to achieve untethered flying robot driven by DEAs.
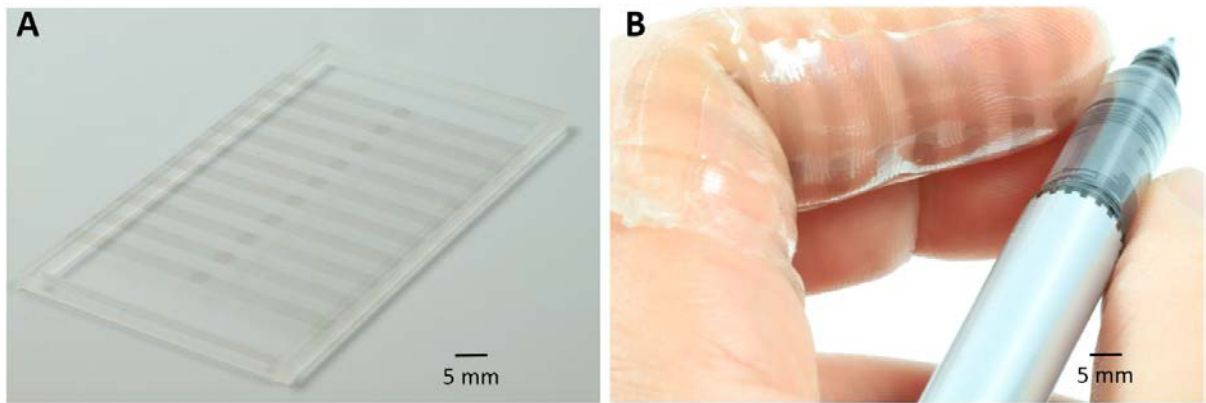
Figure 7.2 "Feel-through" array with 10 ultra-thin DEAs. (A) Photo of the suspended DEA array. (B) Photo of the array on a left index finger, while holding a pen. The ultra-thin DEAs conform to the skin, allowing the user to perform fine manipulations tasks.

Annex A: Bubble stretcher for pre-stretch sub-micron membranes

Introduction

"Bubble stretcher" is developed to pre-stretch thin PDMS membranes for making low working voltage DEA device.

Design concept

The Bubble stretcher consists of three parts as shown in Figure A1. First part, the air chamber to generate air pressure (Figure A1A). Second part, the membrane block (Figure A1B down), and membrane holder for fixing the PDMS (Figure A1B up), and close the air chamber by mechanical stress so that the pressure can be generated. Third part, the substrate (Figure A1C down), and the holder for holding the pre-stretched PDMS membrane (Figure A1C up). A picture of the assembled stretcher is given in Figure A1D.
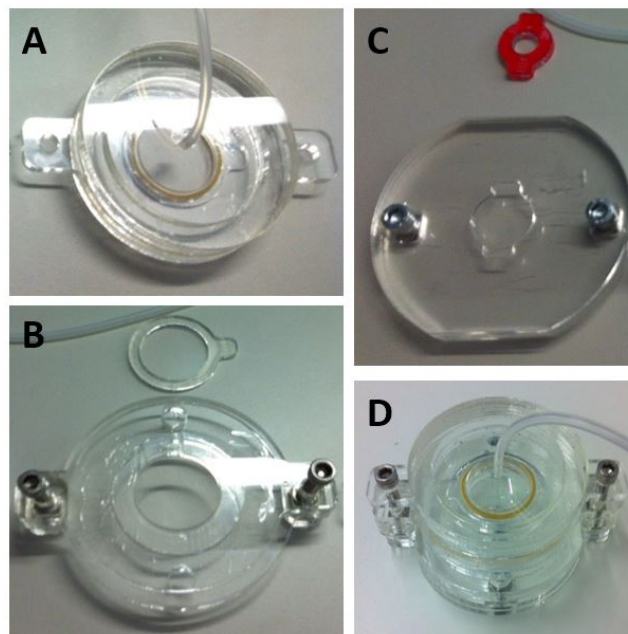
Figure A. 1 Bubble stretcher photos for parts and assembled device. (A) air chamber. (B) the PDMS membrane holder (up) and the membrane block (down). (C) the substrate(down) and the holder for pre-stretched PDMS membrane (up). (D) assembled stretcher.

Working principle

A simplified device configuration and the membrane stretching steps are illustrated in Figure A2.

The air chamber (Figure A2A,①)is connected with a pressure pump. When the pressure inside the air chamber increase, the PDMS membrane is stretched. The detailed steps are illustrated by cartoon in Figure A2B: (i) When the pressure inside the chamber increases, the thin PDMS membrane is deformed, therefore the PDMS membrane can touch the holder for prestretched membrane (Figure A2A,③) and get fixed on it because of the adhesion. In Figure A2B (ii), with the pressure inside the chamber increasing, the adesion between the PDMS membrane and the holder for prestretched PDMS membrane become better. Then, in Figure A2B (iii), with the pressure keeping increasing, the PDMS membrane breaks at the sides. But the parts fixed on the holder is well protected.
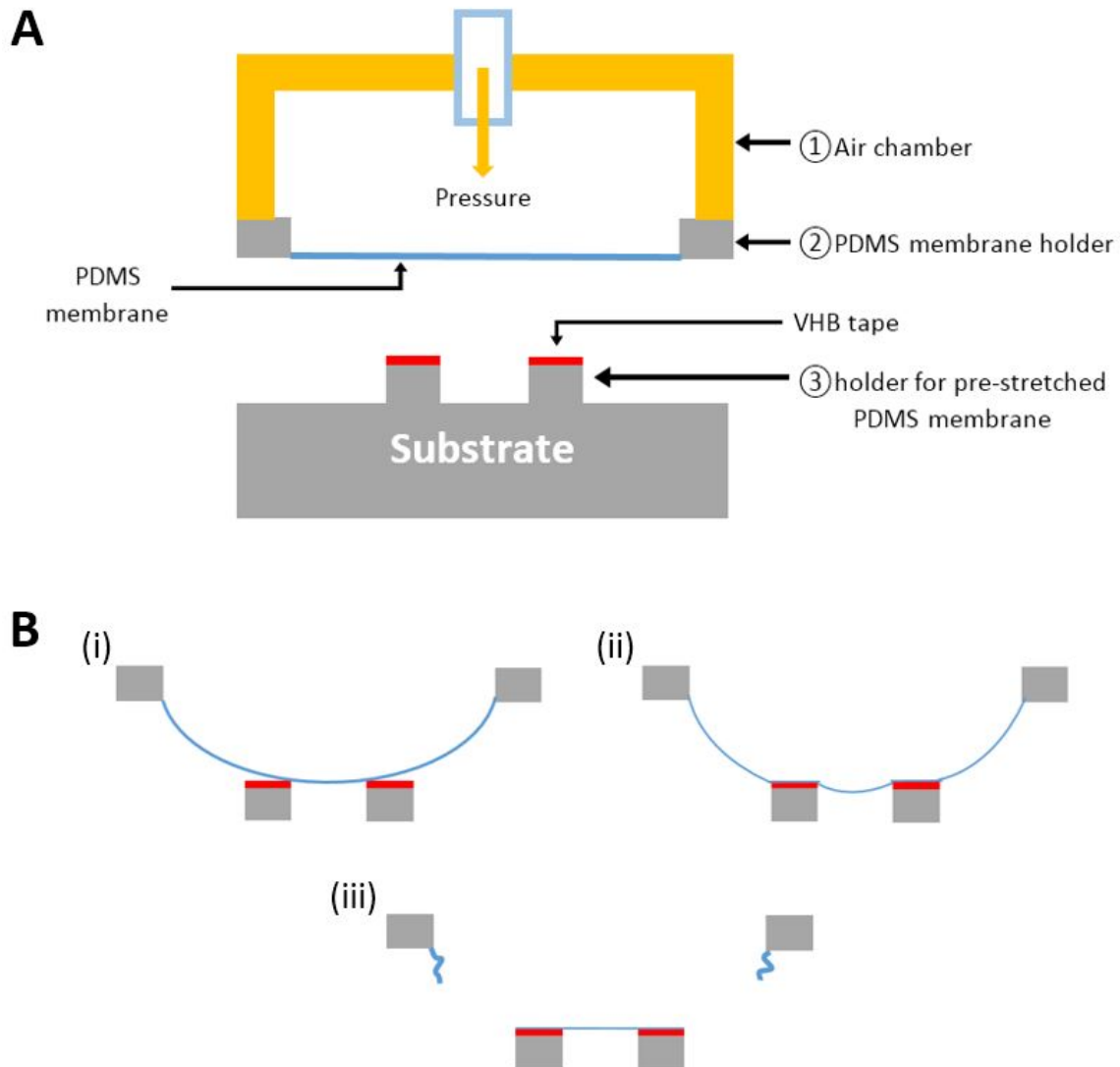
Figure A. 2 Bubble stretcher working principle. (A) simplified Bubble stretcher configuration. (B) different working steps for stretching a sub-µm-thick membrane.

Predictive calculations for $\lambda = 1.3$

For DEA devices with PDMS standard fabrication process (*144*), PDMS with a pre-stretch ratio of $\lambda = 1.3$ is desired. This can be achieved by adjusting the distance d between the holder for pre-stretched membrane Figure A2A③ and the holder of no stretched PDMS Figure A2A②. The meaning of each used symbol for the calculation is given in Figure A3.
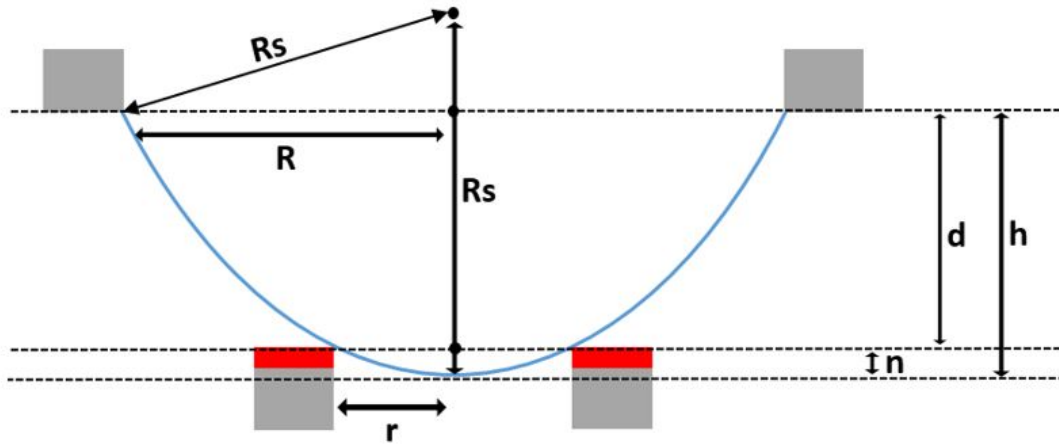
Figure A. 3 Figure illustration for the meaning of the symbols used for calculation.

The surface of stretched PDMS are similar to a spherical cap. And the formula to calculate the surface of a spherical cap is : $S = 2\pi\, rh$

We define the total spherical cap surface is S_t and the surface for the part fixed on the holder Figure A2A③ is S_f .

$$So,\ S_t = 2\pi\, Rs\, h\, ;\, S_f = 2\pi\, Rs\, n.$$

At the boundary state showed by Figure A3, the pre-stretch ratio of the total spherical surface is:

$$\lambda_1{}^2 = \frac{S_t}{\pi\, R^2}$$

When the PDMS is fixed on the holder Figure A2A③, and the pressure disappear, so the fixed part on the holder Figure A2A③ contract and become plan again. And the contract ratio is :

$$\lambda_2{}^2 = \frac{\pi\, r^2}{S_f}$$

So, the final pre-stretch ratio is :

$$\lambda = \lambda_1 * \lambda_2$$

To achieve $\lambda = 1.3$,

$$\frac{2\pi\, Rs\, h * \pi\, r^2}{2\pi\, Rs\, n * \pi\, R^2} = 1.3^2$$

$$\frac{h * r^2}{n * R^2} = 1.3^2 \quad \text{Eq. (A1).}$$

Because, $(Rs-h)^2 + R^2 = Rs^2$

$$\text{So, } Rs = \frac{R^2 + h^2}{2h} \quad \text{Eq. (A2)}$$

And, $(Rs-n)^2 + R^2 = Rs^2$; So,

$$n = \frac{2Rs - \sqrt{4Rs^2 - 4rr}}{2} \quad \text{Eq. (A3)}$$

If we put Eq. (A2) and Eq. (A3) into Eq. (A1), we can obtain :

$$h^2 = \frac{1.1661\, R^4}{1.69\, R^2 - r^2}$$

So, if we put $r = 5$mm, $R = 15$mm. We can get $h = 12.89$mm.

When the stretcher is fabricated, r is fixed at 5mm, and R is fixed at 15mm. And because n is very small, so d is fixed at 12.5mm directly (combination of different thickness PMMA layers and 0.5 mm VHB tape layers of 0.5 mm thick). Then the different parts made from PMMA are cut by laser, and VHB tape of 0.5 mm thick and screws are chosen to insure the adhesion and connection between the parts.

Experiment test

Then the Bubble stretcher is used to stretch the 0.93 µm PDMS membranes, with a pressure of 10 mbar. The membranes are obtained with a final thickness of 0.58 µm after stretching (Figure A4).

So, a stretch ratio of $\lambda = \sqrt[2]{0.93/0.58} = 1.26$ is obtained.

Figure A. 4 Photo of the pre-stretched sub-µm thick PDMS membrane using Bubble stretcher.

Annex B: Electrodes mechanical properties for thin DEAs

To explain the mechanical properties of DEA electrodes, I suppose a DEA consisting of *n* layer of dielectric elastomer sandwiched by *n+1* layer of electrodes, as shown in Figure B1.
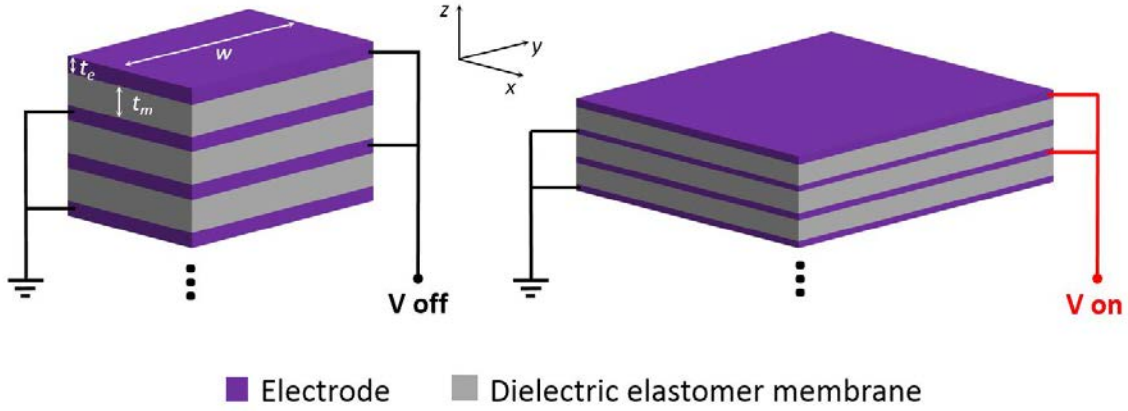
Figure B. 1 Cartoon illustration of DEA consisting n layers of dielectric membranes and n+1 layer of electrodes.

When the voltage is on, the DEA is squeezed in thickness and expand in plan. We suppose that the DEA strain in the *x* direction is s_x, which is generated by the electrostatic force from the applied voltage. Without applying voltage, the equivalent stress F_{exp} to generate the same strain s_x (as using electrostatic force) for *n* layers of dielectric elastomer is :

$$F_{exp} = n \, Y_m \, t_m \, w \, s_x \quad \text{Eq. (B1)}$$

$$s_x = \frac{F_{exp}}{n \, Y_m t_m \, w} \quad \text{Eq. (B2)}$$

With s_x the strain in *x* direction; t_m the thickness of dielectric elastomer membrane; Y_m the Young's modulus of the dielectric elastomer; *w* the width of DEA in *y* direction; F_{exp} the equivalent force to generate the strain s_x in the x direction.

If we apply F_{exp} on the whole DEA structure (taking into account of the *n+1* electrode layers), the corresponding strain in *x* is:

$$s_x' = \frac{F_{exp}}{n \, Y_m t_m \, w + (n+1) \, Y_e t_e \, w} \quad \text{Eq. (B3)}$$

With t_e the thickness of electrode; Y_e the Young's modulus of the electrode; s_x' the strain in the x direction when apply F_{exp} on the DEA.

Dividing the Eq. (B3) by Eq. (B2), we can obtain:

$$\frac{s_x'}{s_x} = \frac{n\, Y_m t_m}{n\, Y_m t_m\ + (n+1)\, Y_e t_e}$$

$$\frac{s_x'}{s_x} = \frac{1}{1 + \frac{(n+1)\, Y_e t_e}{n\, Y_m t_m}}$$

To achieve s_x' as approach as s_x, we can conclude the following inequality should be satisfied:

$$\frac{(n+1)\, Y_e t_e}{n\, Y_m t_m} \ll 1$$

Which is equivalent to:

$$(n+1)\ Y_e\, t_e \ll n\, Y_m\, t_m \quad \text{Eq. (B4)}$$

Eq. B4 shows that the $Y_e\, t_e$ value of the electrode should be as small as possible to not apply significant constrain on the dielectric elastomer during the DEA actuation and result in reduced strain.

Annex C: MWCNT/PT electrode additional characterizations

Optical image and surface resistance correspond to different centrifuge parameters

The MWCNT/P3DT solution is centrifuged before used for the Langmuir monolayer fabrication. The MWCNT/PT electrode system optical image and surface resistance correspond to different centrifuge parameters are given in Figure C1, and Table C1.
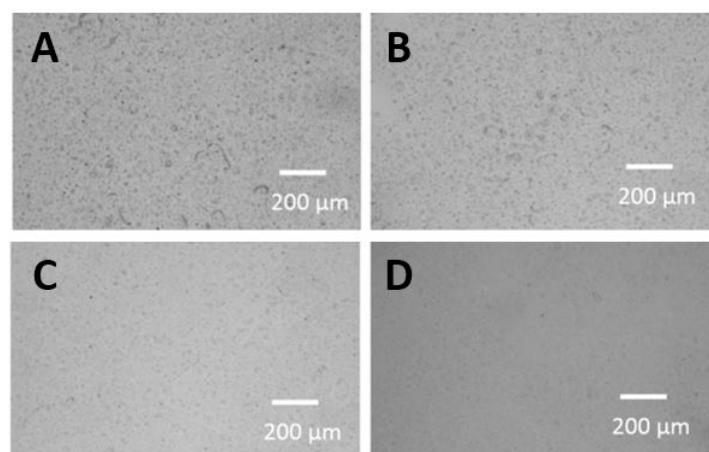
Figure C. 1 Optical microscopy images of MWCNT/P3DT monolayer LS transferred onto PDMS substrate obtained for different centrifugation times of the MWCNT/P3DT spreading solution used for Langmuir monolayer elaboration. (A) 15 min x 1. (B) 15 min x 2. (C) 15 min x 3. (D) 15 min x 4.

Centrifugation Time	Surface Resistance
15 min	18 MΩ
15 min x 2	23 MΩ
15 min x 3	42 MΩ
15 min x 4	200 MΩ

Table C. 1 Surface resistance of the MWCNT/P3DT monolayer LS transferred onto PDMS substrate obtained for different centrifugation times of the MWCNT/P3DT spreading solution used for Langmuir monolayer elaboration.

Brewster Angle Microscopy (BAM)

BAM experiments are performed by means of the apparatus developed by Meunier (227). The air-water interface is illuminated at the Brewster angle (53°) with a polarized collimated laser beam, and the reflected beam is received to a microscope. The BAM image of the fabricated MWCNT/PT layer at the air-water interface is given in Figure C2.
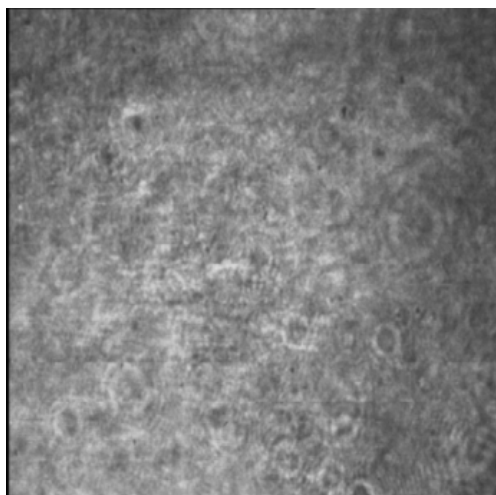
Figure C. 2 BAM image (600 µm x 600 µm) of a P3DT monolayer at the air-water interface at a surface pressure of 15mN/m.

100 µm-thick PDMS substrate for AFM images

The preparation of the 100 µm-thick PDMS membrane is prepared as Rosset et al.(*144*) A solution of siloxane solvent OS-2 (50 wt%), Sylgard 186 part A (45.5 wt%) and part B (4.5 wt%) is blade casted on a polyethylene terephthalate (PET) substrate with a gap of 300 µm. The casted membranes are cured at 100°C for 1 h.

In order to measure the surface resistance as a function of stretching, the PDMS membrane is detached from the PET support. To avoid pre-mechanical stresses, the PDMS membrane and its support are immersed into liquid nitrogen for a few minutes until the PDMS is in its glass state. Then the PDMS membrane is easily peeled off from the PET support. The suspended PDMS with the transferred monolayer regains its stretchability at room temperature. The topography of the electrode is observed by AFM and optical microscopy before and after immersion in liquid nitrogen and no significant change is detected.

10 µm-thick PDMS substrate for Pull test

A very soft PDMS membrane MED-4086 (Young's modulus 40 kPa) is used as substrate for Young's modulus measurements, in order to obtain better precision than with a more rigid membrane. MED-4086 part A (25 wt%) and part B (25 wt%) are diluted in the siloxane solvent OS-2 (50 wt%). The solution is blade casted with a gap of 40 µm on a PET substrate (coated with a PAA sacrificial layer), and cured at 150°C for 45 min in the oven. By releasing in hot water to dissolve the PAA, a suspended 10 µm-thick PDMS membrane is obtained. The suspended 10 µm-thick bare PDMS membrane presents a rectangular shape of dimensions 2 mm x 10 mm.

2.0 µm-thick PDMS membrane for DEA

The 2.0 µm-thick PDMS membrane used for DEA fabrication is obtained from a solution in siloxane solvent OS-2 (66 wt%) of Sylgard 186 part A (31 wt%) and part B (3 wt%).

The solution is blade casted on a PET substrate coated with a PAA sacrificial layer, with a gap of 15 µm, and cured at 100°C for 30 min in an oven.

Photo of the 1.4 µm-thick DEA
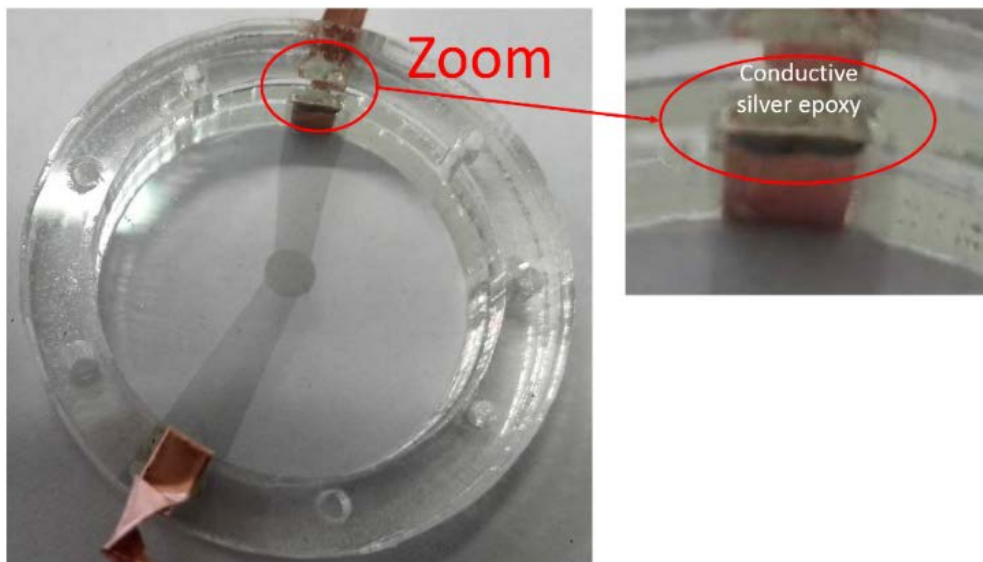
Figure C. 3 1.4 µm-thick DEA device. We highlighted external electrode connection with stretchable electrode by using conductive silver epoxy.

Thickness measurement of the composite MWCNT/PT monolayer electrode.

In order to determine the thickness of the MWCNT/PT monolayer electrode, MWCNT/PT monolayers and pure PT monolayers are LS transferred onto glass substrates covered by a PDMS monolayer ensuring good quality transfer. As PT continuous phase is very thin with respect to MWCNT and not easily detected on the profiles of the composite monolayer, 3-layers PT films are used for PT monolayer thickness measurement. The height profiles are measured at the interface between the film and the bare substrate on at least three areas. No significant difference is detected between both PT having different side chain length.
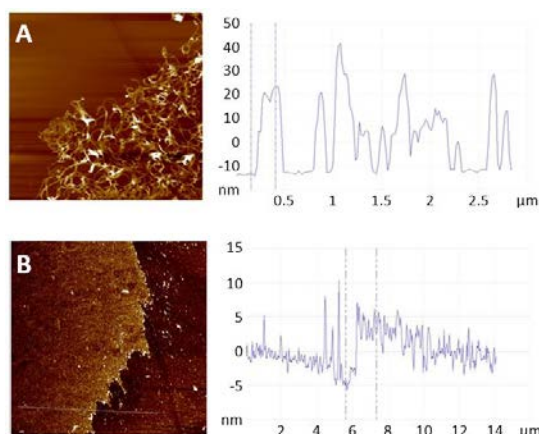
Figure C. 4 AFM images (10 µm X 10 µm) at the step position between bare glass substrate and the corresponding thickness height profile (A) MWCNT/P3DT monolayer (B) 3-layers P3DT

From the height profile of the MWCNT/PT monolayer (Figure C4), a thickness of about 30 nm is deduced for the MWCNT network. From the profile of the 3-layers PT film, a thickness close to 2 nm is deduced for the PT monolayer and thus for the PT continuous phase in the composite MWCNT/PT monolayer. A range of 2 - 30 nm is thus considered for the thickness of the MWCNT/PT composite monolayer.

Monolayer electrode surface resistance as a function of time for MWCNT/P3HT and MWCNT/P3DT electrodes do not present a significant difference. (Figure C5)
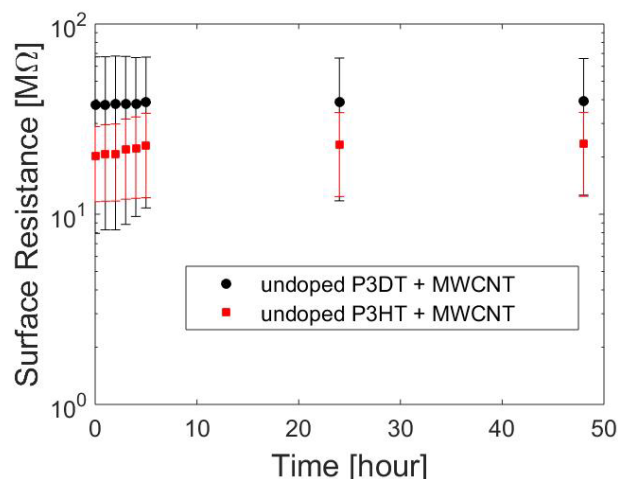
Figure C. 5 Surface resistance of undoped MWCNT/ P3DT and MWCNT/ P3HT composite monolayer electrodes as a function of time.

Additional AFM images under different stretching conditions are given is Figure C6.
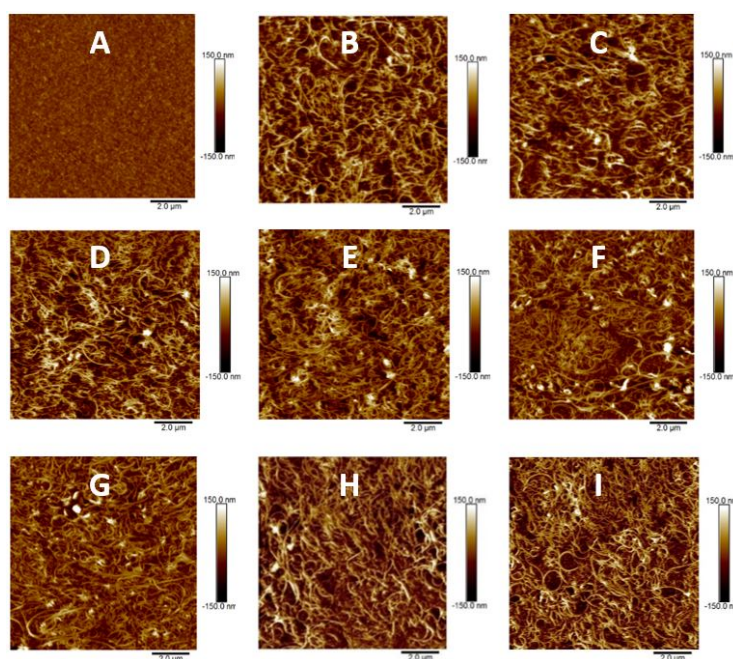
Figure C. 6 AFM images of (A) PDMS bare substrate (B-G) PDMS covered by a MWCNT/P3DT monolayer electrode at different strain values (B) 0%, (C) 20%, (D) 40%, (E) 60%, (F) 80%, and (G) 100%. (H) back to 0% strain after 100% strain. (I) back to 0% after 10 cycles with 60% strain.

DEA characterization: Strain vs. true electric field curve

The DEA strain vs the true electric filed plot based on one sample is given in Figure C7.
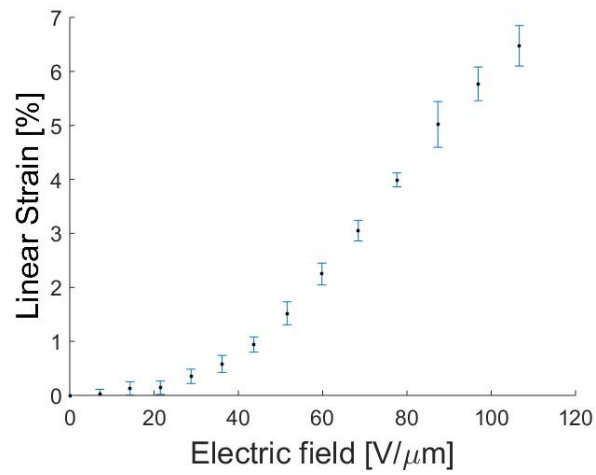
Figure C. 7 Strain vs true electric field.

Annex D: Observations for the fabrication of SWCNT electrode using Langmuir method

In the following part, I describe the observations during all my experiments performed for the fabrication of SWCNT electrode using Langmuir method.

The Langmuir trough that I used to fabricate all the SWCNT electrodes is shown in Figure D1 (KSV NIMA, KN 2002).
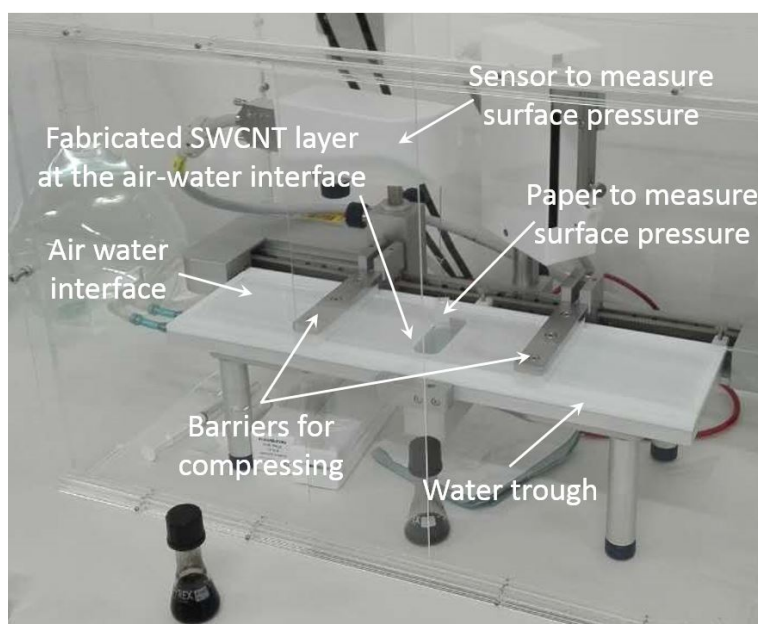
Figure D. 1 Langmuir tough photo with formed SWCNT layer at the air-water interface.

When the trough is filled with ultra-pure water, an air-water interface is generated. Once the pressure sensor is calibrated, 80 µL of SWCNT solution (0.5 g/L in chloroform) are spread dropwise on the air-water interface. Then the monolayer is rested for 2 minutes to allow the solvent evaporation.

Using the barriers, the SWCNTs monolayer is then compressed at a constant speed until the desired surface pressure is reached. The reproducibility of the monolayer density is controlled and the stability of the monolayer is also checked by monitoring the area variation at constant surface pressure during a few minutes.

If the area is constant, the monolayer can be transferred onto substrate (e.g. PET, PDMS etc.). For this, the substrate is horizontally approached to the layer at the air-water interface and then raised.

Annex E: DEA electrical response speed prediction using cut-off frequency

In the following part, the influence of the dielectric membrane thickness on the electric response time of the DEA is studied. We suppose that the DEA active zone is a 3mm diameter circle with PDMS (polydimethylsiloxane) as dielectric elastomer (Figure E1.A). The corresponding equivalent electric circle is supposed to be as in Figure E1.B (supposing leakage current is 0A).
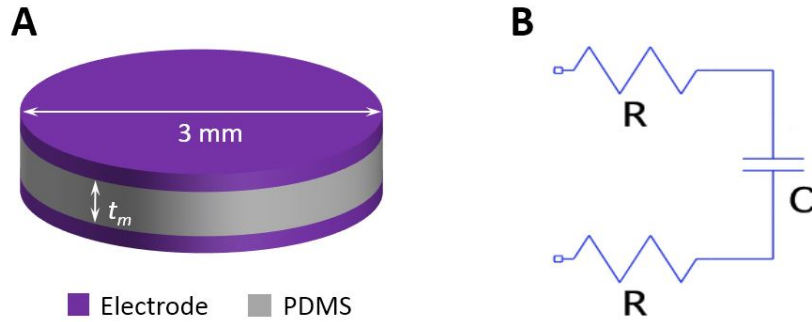
Figure E. 1 DEA structure and electronic circuit model. (A) DEA structure: 3 mm diameter circle with PDMS as dielectric membrane. (B) Equivalent electronic circuit of DEA used in this prediction.

The cut-off frequency of the capacitor is:

$$f_c = \frac{1}{2\pi * \tau} = \frac{1}{4\pi * R * C} = \frac{t_m}{4\pi\, R\, \varepsilon_0\, \varepsilon_r\, A_0} \quad \text{Eq. (E1)}$$

With R the electrode resistance; C the capacitance of the DEA; τ the RC time constant; t_m the thickness of PDMS; f_c the cut off frequency; ε_0 the permittivity of the vacuum ; ε_r the relative permittivity of dielectric ; A_0 the area of the DEA active zone.

$$R = \frac{t_m}{4\pi\, f_c\, \varepsilon_0\, \varepsilon_r\, A_0} \quad \text{Eq. (E2)}$$

We can easily estimate the maximum electrode resistance R from Eq. (E2). In Figure E2, we plot (with log scale for both axis) the maximum electrode resistance as function of the PDMS thickness (t_m, ranging from 1 nm to 100 µm) for a given operating frequency (ranging from 0.1 Hz to 1000 Hz).

Figure E2 shows that: for a given operating frequency, when the thickness of the PDMS decreases, the maximum electrode resistance should also be decreased to keep the same operation frequency. This means that the electrode for DEAs with thinner PDMS layer should present

better electrical conductivity than the one for thick PDMS layers for working at the same frequency. If we fix the PDMS thickness at constant value, DEAs capable of high operation frequency correspond to the ones with low electrode resistance.
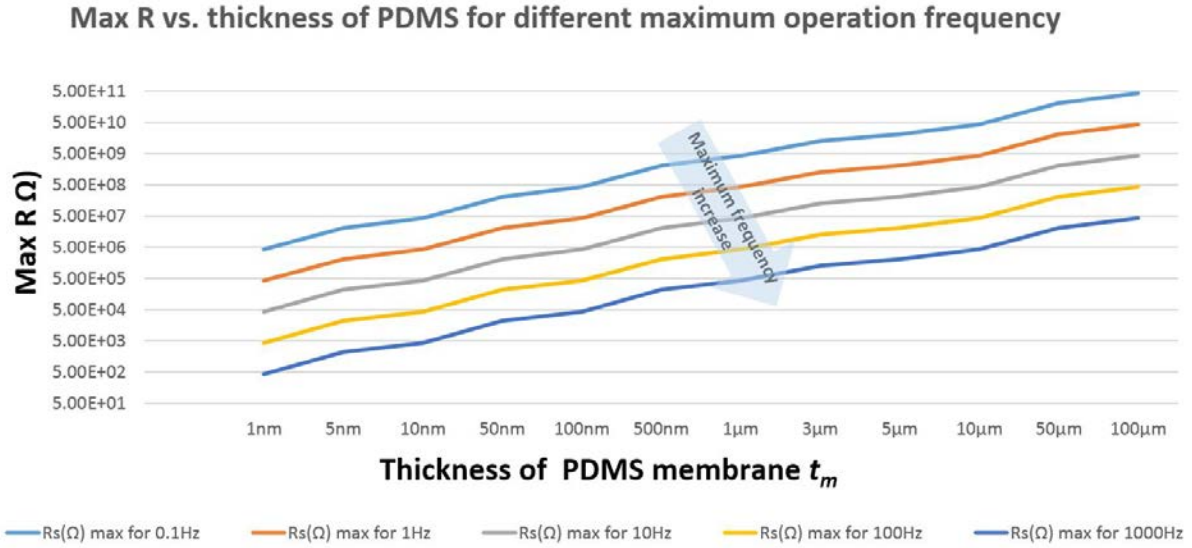
Figure E. 2 Influence of PDMS dielectric thickness on the DEA electrical response time.

Annex F: PDMS LSR 4305 pre-stretch ratio determination

From experimental results, we find that the PDMS LSR 4305 is promising to be used as the DE layers for making low-voltage DEAs.

We fabricate different DEAs to determine the pre-stretch ratio needed for this PDMS membrane to give the best electromechanical performance. The initial thickness of the PDMS membrane we fabricated is 18 µm-thick. Then the 18 µm-thick PDMS membranes are equi-biaxially pre-stretched to different final thickness with different pre-stretch ratios. DEAs with each PDMS membrane with different pre-stretch ratios are fabricated. The DEAs are then characterized regarding to the maximum achievable strain and corresponding breakdown voltage. The data is presented in Table F1.

DEA sample number	Initial PDMS membrane thickness (µm)	Final PDMS membrane thickness (µm)	Pre-stretch ratio	Maximum applied Voltage (V)	Normalized breakdown field (V/ µm)	Linear strain at breakdown field (%)
1	18	11.0	1.3	450	48.6	9.3
2	18	4.3	2	320	96.0	13.0
3	18	4.5	2	320	91.4	12.0
4	18	2.9	2.5	300	122	8.9

Table F. 1 Influence of pre-stretch ratio on the DEA fabricated with PDMS LSR 4305.

From Table F1, we can find that: with the pre-stretch ratio around 2, this PDMS membrane give the highest S/kV^2 ratio compared to other fabricated DEAs with different PDMS membrane pre-stretch ratio.

Annex G: Single layer DEA performance characterizations

To explore the effect of different electrodes materials and fabrication process on DEA performance, we fabricate three types of single layer DEAs using the same pre-stretched PDMS LSR4305 layer with final thickness of 6 µm. And compared their performance with the LVS-DEA. The information about fabrication and materials used for these four types of DEAs are described in Table G1. We compared these four types of DEAs with one sample for each type of DEA. They are compared with the structure of a DEAnsect robot leg, by measuring leg displacement and leg speed, see Figure G1.

Name of DEAs	Oxygen plasma (OP) treatment for PDMS dielectric layer	Number of dielectric layers	Electrode fabrication technique
SWCNT electrode	without OP treatment	1	LS SWCNT
SWCNT electrode OP	with OP treatment	1	LS SWCNT
Pad-printed electrode	without OP treatment	1	Pad-Printing carbon black dispersed in PDMS
Stacked DEA (LVSDEA)	with OP treatment	3	LS SWCNT

Table G. 1 The four types of DEAs used to compare actuation performance. They differ by: i) electrode fabrication technology, ii) number of dielectric layers, and iii) use or not of oxygen plasma treatment for better electrode adhesion.
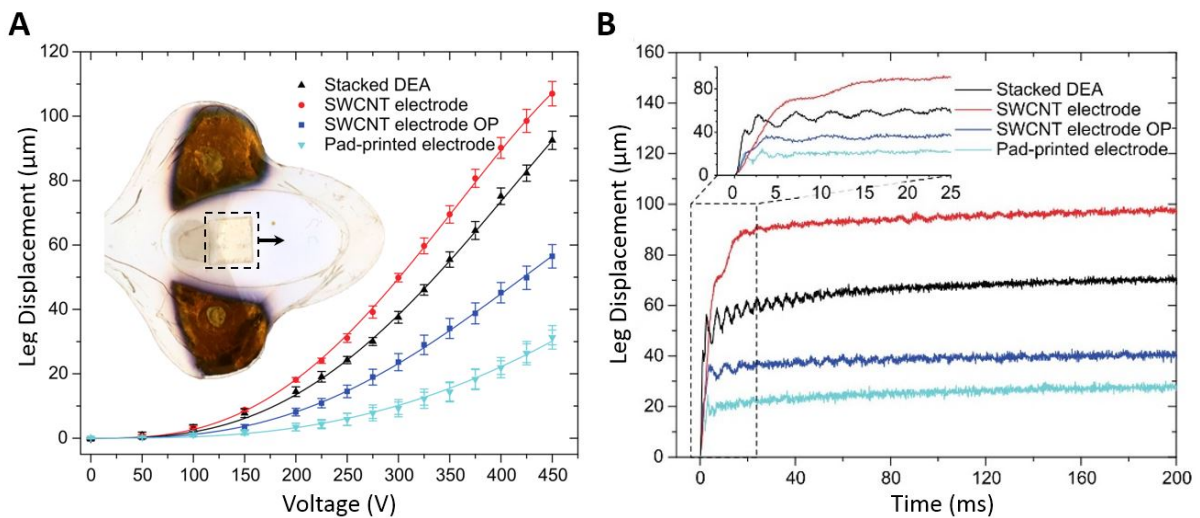
Figure G. 1 Comparison of LVSDEAs with three types of single layer DEAs made with different conditions as listed in Table G1, integrated in a DEAnsect leg structure. (A) Leg displacement vs. applied DC voltage (after 5s). (B) Leg displacement vs. time with for a 450V step driving voltage. The LVSDEAs shows be best combination of displacement and speed.

In Figure G1A, for a 450 V DC driving signal, the DEAs with LS fabricated electrodes show larger leg displacement than the one with the Pad-Printed electrodes we typically use for our kV DEAs (*144*). This shows that the ultra-thin (less than 100 nm-thick) SWCNT electrode fabricated using LS method presents less stiffening effect than the 2 µm-thick pad-printed electrodes. Comparing the DEA SWCNT electrode and SWCNT electrode OP, the former shows larger leg displacement. This is due to the oxygen plasma (OP) treatment for the DEA (SWCNT electrode OP) stiffens the PDMS dielectric layer (*228*), because the OP treatment is possible to form one rigid layer of silica dioxide on the PDMS surface. By comparing DEA SWCNT electrode OP and the stacked DEAs, the leg displacement of the stacked DEAs is bigger, which indicates that the stiffening effect of OP treatment is less for the stacked structure, which is due to the increased silicone ratio with the stacked structure.

Leg displacement vs. charging time is reported in Figure G1B. The DEA SWCNT electrode shows the largest leg displacement, however it needs the longest time to respond, i.e., it has the longest electrode RC time constant. The surface resistance of electrodes on the PDMS without OP treatment (3 MΩ/sq) is more than 10 times higher than with OP treatment (150 kΩ/sq). For other types of DEAs, the time to achieve full strain is about the same. In this case, the response time may be limited by the mechanical properties (viscoelasticity) of the PDMS membranes. For the DEA with thick Pad-printed electrodes, the leg displacement is mechanically limited principally by the electrode stiffening effect.

From Figure G, we can conclude that OP treatment can lower the electrode surface resistance to increase the DEA operating speed, however the OP treatment can also stiffen the DEA resulting in lower output strain. With stacked structures, due to the increased output force, the stiffening effect of OP treatment on the DE layers is reduced due to the decreased electrode/dielectric layer ratio in the stacked structure. Among the four types of DEAs, the stacked DEA (LVSDEA) presents the best combination of fast actuation and high leg displacement.

Annex H: LVSDEA power density calculation

In this part, I explain how the power density of the LVSDEAs (shown in the section 5.5.4) is calculated.

I use the equation that Pelrine et al (*65*) used for estimating the elastic strain energy density in DEAs:

$$u_e = \frac{1}{2} Y s_z^2 \quad \text{Eq. (H1)}$$

With u_e the elastic strain energy density per unit volume; Y the Young's modulus of the dielectric elastomer; s_z the DEA thickness strain.

Using Eq. (H1), we can get the power density by multiplying the energy density with the DEA operation frequency f. So:

$$P = u_e * f = \frac{1}{2} Y s_z^2 * f \quad \text{Eq. (H2)}$$

With P the power density per unit volume; f the DEA operation frequency.

The Power density vs. DEA operation frequency plot is given in Figure H1. The data points are based on the same data given in Figure 5.13B.
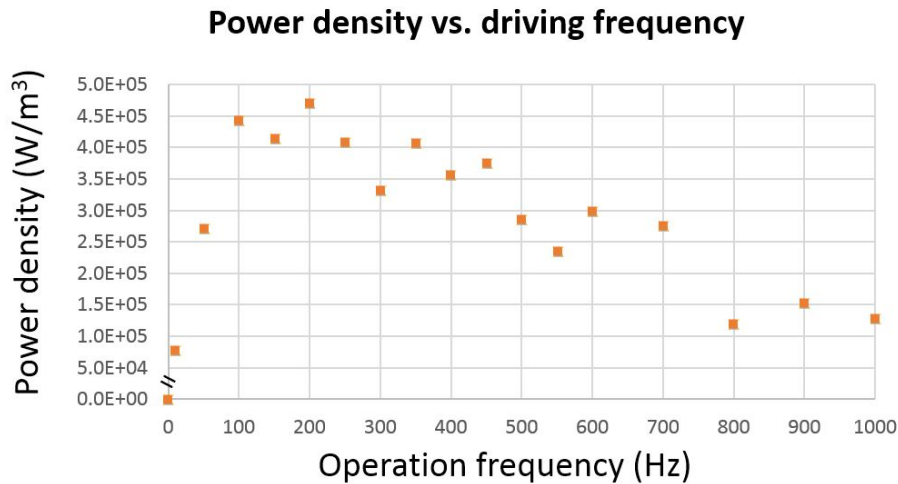
Figure H. 1 LVSDEAs power density as function of its operation frequency.

Figure H1 shows that the power density first increases with the operation frequency increase, and presents a peak value (~4.5 10^5 W/m^3) at 200 Hz. Then it decreases with operation frequency increasing due to the decreased strain values, which are limited by the DEA response time.

Annex I: Sub-gram UnArM electronics

The design and performance of the compact low-mass on-board electronics used to drive the UnArM modules are described here. This work is done by Dr. Xinchang LIU in the EPFL-LAI. This Annex I is adapted from the publication in preparation:

X. Ji, X. Liu, V. Cacucciolo, M. Imboden, Y. Civet, A. E. Haitami, S. Cantin, Y. Perriard, H. Shea. "Untethered Untethered Artificial Muscles for Autonomous Soft Machines", In preparation.

The following part is written by Dr. Xinchang LIU.

Description	Model	Quantity	Weight (mg)
Transformer	ATB322515	2	96
MOSFET	EPC2035	2	3
MOSFET	BSS127	1	8
Resistor	0201	1	1
Diode	CMSD2004S	7	56
Capacitor	0805	3	51
Sensors	VCNT2020 and other components	2	33
Microcontroller	LPC1102	1	5
Power management	TLV70528YFPR and other components	1	6
LED	0402	1	1
FPCB	L: 29 mm; W: 21 mm; (391 mm^2)	1	70
Solder			~ 20
Switch	Custom made	1	~ 40
Battery	Lithium polymer 12 mAh	1	390
Total weight			~780

Table I. 1 Components of the 780 mg electronics board.

We explain only in detail here the on-board electronics for the DEAnsect. The electronics principle is the same for the untethered "feel-through" haptic devices. As shown in Table I1, the

bare DEAnsect robot (i.e. without the electronics) can carry a 950 mg load (see Chapter 5) when driven by a 450 V square wave at a frequency ranging from 300 to 500 Hz. The electrical equivalent circuit for the DEAs can be approximated as a capacitance $C_a = 92$ pF in series with a resistance $R_a = 2$ MΩ. In order to achieve directional control, at least two independent output channels are required. Given that the lowest mass commercial lithium polymer battery we could obtain weighs 390 mg, the mass budget for the lightweight driver is 560 mg. The circuit must charge three LVSDEAs to the target voltage (up to 480 V) at their mechanical resonance frequency (up to 500 Hz), starting from an initial voltage of 3.7 V, with a step-up ratio higher than 100, and an operating time of 10 min for a fully charged battery.

Miniaturized voltage conversion circuits for micro-robotic applications have been reported (*225*, *229*). Commercially available voltage converters with the required capabilities weigh several grams. The smallest reported standalone voltage converter used for piezoelectric flapping-wing robotic insect is a sub-50mg voltage converter and high-voltage drivers (without control functionality) with step-up ratios of up to 60 and working frequency of 120 Hz (*225*).

Energy efficiency is an important design constraint, because it influences strongly the robot's operating time. Campolo et al. (*230*) proposed a charge recovery scheme for piezoelectric actuators using additional components. Mottet et al. (*231*) studied resonating topologies to transfer electrical charge between multiple DEAs with an increase of the amount of energy transferred. The waveform conditioning stage after the high voltage output and the current feedback measurement becomes complex both in terms of weight and power consumption. As a result, an open loop circuit may be the best-suited for our case. We thus opted to develop an open loop flyback solution to drive the DEAs. The on-board electronics consist of a power management module, micro-controller, voltage converter driver and proximity reflective objective detection circuit as shown in Figure I1A.

The DEAnsect has three actuators: front, left and right. If all three actuators are activated, the robot moves straight forward. If one of the side actuators is turned off, the robot turns towards that actuator. In principle, a three-channel driver is required if each actuator must to be independently controlled. However, if all three actuators are operated at the same frequency (because their mechanical resonance frequencies are nearly identical), it is possible to arrange the outputs of a two channel flyback driver to enable active steering.

The circuit topology and selected components are given in Figure I1B and in Table I1. The basic principle of the flyback circuit is as follows. First, turn on switch S1 to let a current flow in the primary of the transformer. Then, when S1 is switched off, the transformer will release its stored energy to the secondary side, thus, creating a peak voltage and current pulse. As the diode D1 allows the current to flow only in one direction, the capacitor C1 will be charged to a high voltage. S2 is a switch to discharge the DEA. By alternating charging and discharging cycle, the DEA can be driven at a desired frequency.

From the energy point of view, an efficient flyback circuit should have a low equivalent capacitance (depending mostly on the MOSFET and the PCB material) or a high input power, initially stored in the transformer. The current is limited by the saturation and power dissipation limit of the transformer. In practice, the current at the primary side is set to 1.25 A. The selection of C1 is also a delicate topic. On one hand, it is preferred to have a low value capacitor because the energy will be released after each charging and discharging cycle. On the other hand, C1 is also the buffer between the direct output of a flyback circuit and the DEA load. If its value is too small, the DEA will not work correctly.

In one charging cycle, one pulse typically is not sufficient to raise the voltage to the desired level. Multiple pulses are thus needed to step up the voltage. As each pulse consume energy E_i, the more pulses one cycle has, the less efficient the system is. The objective is therefore to achieve the required voltage with a minimal number of pulses. Several parameters affect the step-up performance such as the spacing time t_s between two pulses and the output capacitor value C_1, as seen above. A solver was been programmed to optimize C_1 and t_s. Figure I1C shows the effective amplitude in function of output capacitor value and spacing time for the minimum pulse number to achieve a signal equivalent to a 450 V square wave. Figure I1D gives the optimal waveform during one complete charging/discharging cycle.

For a working frequency 500 Hz and using the results of the optimization process, the power needed for three actuators is given in Equation S1:

$$P_{3DEAs} = 3.f_s.n_{pulse}.E_i = 204.8 \text{ mW} \quad \text{Eq. (I.1)}$$

A 3.7 V lithium polymer battery of 12 mA.h capacity can provide about 159.8 J energy. Divided by P_{3DEAs} in Eq. I.1, the total working duration is 780 s or 13 minutes. The driver efficiency can be defined as the average efficiency of all pulses in one charging cycle. According to the simulation, the average driver efficiency is 31.7%. If we consider the voltage charged to actuator's equivalent capacitor, the efficiency of the electronic system can also be defined as the energy stored to the actuator after one charging cycle divided by the total input energy. In this case, the efficiency drops to 6.9%, mainly because of the electrode's high resistance (2 MΩ) of the DEA.

Figure I1E shows the flexible PCB of the drive with soldered components. The surface of the driver is 391 mm^2. On the top side, there are four output pads where the wires of the robot can be soldered. The battery and the mechanical switch are also soldered on the Flex-PCB at the narrow end.

An endurance test has been carried out measuring one output channel with an output capacitor of 47 pF instead of the 75 pF obtained from the optimization results. As a result, we are not at the optimal working point and the target voltage is lowered. However, 25 pulses are still used in this test by adjusting the pulse spacing. As shown in Figure I1B, two actuators are powered up during this test. The theoretical duration is 19.5 minutes. The test gives a measured working time of 19 minutes, at which point the battery voltage drops below 3 V (Figure I1F).

Due to characteristics of the Li-polymer battery, one has a drop of about 20% of the input voltage during operation. The micro-controller has been programmed to compensate for this. In Figure I1F, one can see that the output voltage is maintained with less than 1.2% variation during the first 15 minutes. When the battery voltage drops more significantly, the voltage swing can reach up to 3.6%.

For the feel-through application, a single channel driver has been made for one DEA (Figure I1G and Figure I1H). It shares the same principle and parameters optimization method as for the DEAnsect. As the requirement on mass is not as strict as for the DEAnsect robot, the flexible PCB has been stiffened to improve its mechanical robustness, and a larger infrared module has been adopted to increase the sensing distance up to 10 mm. A more robust, but heavier, switch and more LEDs are added to facilitate the user interaction with the driver.
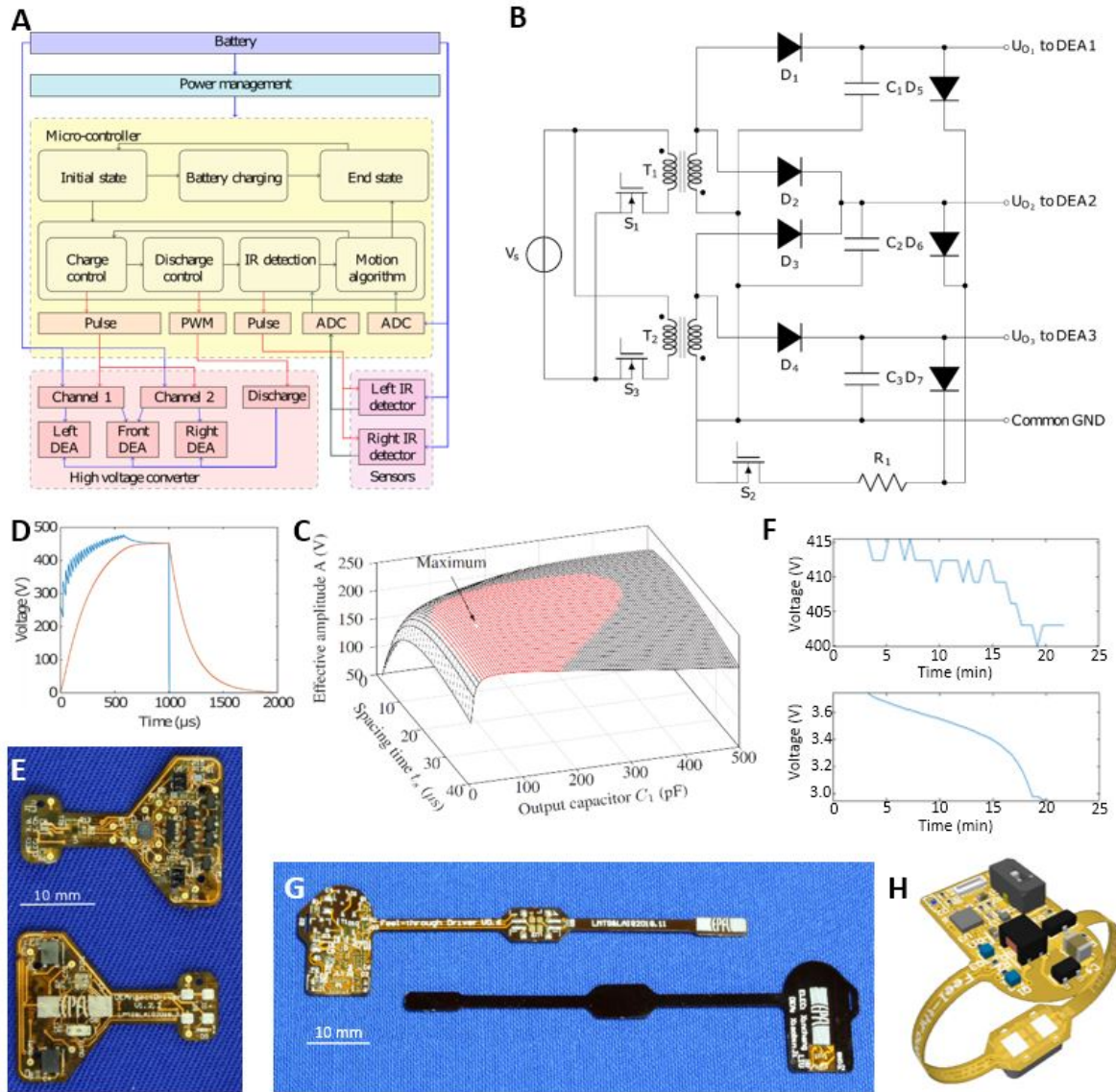
Figure I. 1 On-board electronics for UnArM modules. (A) Block diagram of low-mass control electronics. Blue lines: power Bus. Black lines: program state changes. Red lines: control signals. Green lines: sensor signals. (B) Two channel flyback circuit for driving three actuators. (C) Optimization results for t_s and C_1, using a minimum $n_{pulse} = 25$. The white point is the

maximum where $A = 248$ V while $t_s = 24$ µs and $C_1 = 75$ pF. The red area is the area for Amplitude > 231.5 V, which corresponds to an effective amplitude of a 420 V square wave at 500 Hz. (D) Simulated output voltage of the driver (in blue) and the voltage on the equivalent capacitor of the DEA (in red). The effective fundamental amplitude of Fourier transform of the red curve is 248 V while $n_{pulse} = 25$, $t_s = 24$ us and $C_1 = 75$ pF. The maximum driver output voltage is 476 V, the final voltage of the charging cycle is 452 V. (E) Photo of DEAnsect driver circuit. (F) Endurance test results. (G) Photo of Feel-through driver circuit. (H) CAD illustration of the Feel-through driver circuit folded for mounting on a fingertip.

References

1. C. Majidi, Soft-Matter Engineering for Soft Robotics. *Adv. Mater. Technol.*, 1800477 (2018).

2. D. Rus, M. T. Tolley, Design, fabrication and control of soft robots. *Nature*. **521**, 467–475 (2015).

3. S. M. Mirvakili, I. W. Hunter, Artificial Muscles: Mechanisms, Applications, and Challenges. *Adv. Mater.* **30**, 1704407 (2018).

4. L. Hines, K. Petersen, G. Z. Lum, M. Sitti, Soft Actuators for Small-Scale Robotics. *Adv. Mater.* **29**, 1603483 (2017).

5. L. Maffli, S. Rosset, M. Ghilardi, F. Carpi, H. Shea, Ultrafast All-Polymer Electrically Tunable Silicone Lenses. *Adv. Funct. Mater.* **25**, 1656–1665 (2015).

6. J. Huang, T. Li, C. Chiang Foo, J. Zhu, D. R. Clarke, Z. Suo, Giant, voltage-actuated deformation of a dielectric elastomer under dead load. *Appl. Phys. Lett.* **100**, 041911 (2012).

7. C. Keplinger, T. Li, R. Baumgartner, Z. Suo, S. Bauer, Harnessing snap-through instability in soft dielectrics to achieve giant voltage-triggered deformation. *Soft Matter*. **8**, 285–288 (2012).

8. M. Aschwanden, A. Stemmer, Y. Bar-Cohen, Ed. (San Diego, California, 2007; http://proceedings.spiedigitallibrary.org/proceeding.aspx?doi=10.1117/12.713325), p. 65241N.

9. A. D. Marchese, R. K. Katzschmann, D. Rus, A Recipe for Soft Fluidic Elastomer Robots. *Soft Robot.* **2**, 7–25 (2015).

10. S. Kurumaya, B. T. Phillips, K. P. Becker, M. H. Rosen, D. F. Gruber, K. C. Galloway, K. Suzumori, R. J. Wood, A Modular Soft Robotic Wrist for Underwater Manipulation. *Soft Robot.* **5**, 399–409 (2018).

11. F. Ilievski, A. D. Mazzeo, R. F. Shepherd, X. Chen, G. M. Whitesides, Soft Robotics for Chemists. *Angew. Chem. Int. Ed.* **50**, 1890–1895 (2011).

12. A. Rafsanjani, Y. Zhang, B. Liu, S. M. Rubinstein, K. Bertoldi, Kirigami skins make a simple soft actuator crawl. *Sci. Robot.* **3**, eaar7555 (2018).

13. M. Wehner, R. L. Truby, D. J. Fitzgerald, B. Mosadegh, G. M. Whitesides, J. A. Lewis, R. J. Wood, An integrated design and fabrication strategy for entirely soft, autonomous robots. *Nature*. **536**, 451–455 (2016).

14. N. W. Bartlett, M. T. Tolley, J. T. B. Overvelde, J. C. Weaver, B. Mosadegh, K. Bertoldi, G. M. Whitesides, R. J. Wood, A 3D-printed, functionally graded soft robot powered by combustion. *Science*. **349**, 161–165 (2015).

References

15. A.-M. Georgarakis, H. A. Sonar, M. D. Rinderknecht, O. Lambercy, B. J. Martin, V. Klamroth-Marganska, J. Paik, R. Riener, J. E. Duarte, in *2017 International Conference on Rehabilitation Robotics (ICORR)* (IEEE, London, 2017; https://ieeexplore.ieee.org/document/8009216/), pp. 25–30.

16. J. J. Huaroto, E. Suarez, H. I. Krebs, P. D. Marasco, E. A. Vela, A Soft Pneumatic Actuator as a Haptic Wearable Device for Upper Limb Amputees: Toward a Soft Robotic Liner. *IEEE Robot. Autom. Lett.* **4**, 17–24 (2019).

17. R. F. Shepherd, F. Ilievski, W. Choi, S. A. Morin, A. A. Stokes, A. D. Mazzeo, X. Chen, M. Wang, G. M. Whitesides, Multigait soft robot. *Proc. Natl. Acad. Sci.* **108**, 20400–20403 (2011).

18. P. Polygerinos, S. Lyne, Zheng Wang, L. F. Nicolini, B. Mosadegh, G. M. Whitesides, C. J. Walsh, in *2013 IEEE/RSJ International Conference on Intelligent Robots and Systems* (IEEE, Tokyo, 2013; http://ieeexplore.ieee.org/document/6696549/), pp. 1512–1517.

19. M. T. Tolley, R. F. Shepherd, B. Mosadegh, K. C. Galloway, M. Wehner, M. Karpelson, R. J. Wood, G. M. Whitesides, A Resilient, Untethered Soft Robot. *Soft Robot.* **1**, 213–223 (2014).

20. A. Miriyev, K. Stack, H. Lipson, Soft material for soft actuators. *Nat. Commun.* **8** (2017), doi:10.1038/s41467-017-00685-3.

21. M. A. Robertson, H. Sadeghi, J. M. Florez, J. Paik, Soft Pneumatic Actuator Fascicles for High Force and Reliability. *Soft Robot.* **4**, 23–32 (2017).

22. A. A. Stokes, R. F. Shepherd, S. A. Morin, F. Ilievski, G. M. Whitesides, A Hybrid Combining Hard and Soft Robots. *Soft Robot.* **1**, 70–74 (2014).

23. J. Barreiros, H. Claure, B. Peele, O. Shapira, J. Spjut, D. Luebke, M. Jung, R. Shepherd, Fluidic Elastomer Actuators for Haptic Interactions in Virtual Reality. *IEEE Robot. Autom. Lett.* **4**, 277–284 (2019).

24. A. D. Marchese, C. D. Onal, D. Rus, Autonomous Soft Robotic Fish Capable of Escape Maneuvers Using Fluidic Elastomer Actuators. *Soft Robot.* **1**, 75–87 (2014).

25. H. Yuk, S. Lin, C. Ma, M. Takaffoli, N. X. Fang, X. Zhao, Hydraulic hydrogel actuators and robots optically and sonically camouflaged in water. *Nat. Commun.* **8**, 14230 (2017).

26. P. Polygerinos, Z. Wang, K. C. Galloway, R. J. Wood, C. J. Walsh, Soft robotic glove for combined assistance and at-home rehabilitation. *Robot. Auton. Syst.* **73**, 135–143 (2015).

27. R. K. Katzschmann, J. DelPreto, R. MacCurdy, D. Rus, Exploration of underwater life with an acoustically controlled soft robotic fish. *Sci. Robot.* **3**, eaar3449 (2018).

28. S. Terryn, J. Brancart, D. Lefeber, G. Van Assche, B. Vanderborght, Self-healing soft pneumatic robots. *Sci. Robot.* **2**, eaan4268 (2017).

29. D. Yang, M. S. Verma, J.-H. So, B. Mosadegh, C. Keplinger, B. Lee, F. Khashai, E. Lossner, Z. Suo, G. M. Whitesides, Buckling Pneumatic Linear Actuators Inspired by Muscle. *Adv. Mater. Technol.* **1**, 1600055 (2016).

30. T. Chen, O. R. Bilal, K. Shea, C. Daraio, Harnessing bistability for directional propulsion of soft, untethered robots. *Proc. Natl. Acad. Sci.* **115**, 5698–5702 (2018).

31. M. Behl, A. Lendlein, Shape-memory polymers. *Mater. Today*. **10**, 20–28 (2007).

32. K. Wang, X. X. Zhu, Two-Way Reversible Shape Memory Polymers Containing Polydopamine Nanospheres: Light Actuation, Robotic Locomotion, and Artificial Muscles. *ACS Biomater. Sci. Eng.* **4**, 3099–3106 (2018).

33. K. Wang, Y.-G. Jia, X. X. Zhu, Two-Way Reversible Shape Memory Polymers Made of Cross-Linked Cocrystallizable Random Copolymers with Tunable Actuation Temperatures. *Macromolecules*. **50**, 8570–8579 (2017).

34. N. Besse, S. Rosset, J. J. Zarate, H. Shea, Flexible Active Skin: Large Reconfigurable Arrays of Individually Addressed Shape Memory Polymer Actuators. *Adv. Mater. Technol.* **2**, 1700102 (2017).

35. M. Rogóż, H. Zeng, C. Xuan, D. S. Wiersma, P. Wasylczyk, Light-Driven Soft Robot Mimics Caterpillar Locomotion in Natural Scale. *Adv. Opt. Mater.* **4**, 1689–1694 (2016).

36. J. Zhou, S. A. Turner, S. M. Brosnan, Q. Li, J.-M. Y. Carrillo, D. Nykypanchuk, O. Gang, V. S. Ashby, A. V. Dobrynin, S. S. Sheiko, Shapeshifting: Reversible Shape Memory in Semicrystalline Elastomers. *Macromolecules*. **47**, 1768–1776 (2014).

37. Y. Mao, K. Yu, M. S. Isakov, J. Wu, M. L. Dunn, H. Jerry Qi, Sequential Self-Folding Structures by 3D Printed Digital Shape Memory Polymers. *Sci. Rep.* **5** (2015), doi:10.1038/srep13616.

38. C. S. Haines, M. D. Lima, N. Li, G. M. Spinks, J. Foroughi, J. D. W. Madden, S. H. Kim, S. Fang, M. Jung de Andrade, F. Goktepe, O. Goktepe, S. M. Mirvakili, S. Naficy, X. Lepro, J. Oh, M. E. Kozlov, S. J. Kim, X. Xu, B. J. Swedlove, G. G. Wallace, R. H. Baughman, Artificial Muscles from Fishing Line and Sewing Thread. *Science*. **343**, 868–872 (2014).

39. J. Zotzmann, M. Behl, D. Hofmann, A. Lendlein, Reversible Triple-Shape Effect of Polymer Networks Containing Polypentadecalactone- and Poly(ε-caprolactone)-Segments. *Adv. Mater.* **22**, 3424–3429 (2010).

40. X. Huang, K. Kumar, M. K. Jawed, A. Mohammadi Nasab, Z. Ye, W. Shan, C. Majidi, Highly Dynamic Shape Memory Alloy Actuator for Fast Moving Soft Robots. *Adv. Mater. Technol.*, 1800540 (2019).

41. H.-T. Lin, G. G. Leisk, B. Trimmer, GoQBot: a caterpillar-inspired soft-bodied rolling robot. *Bioinspir. Biomim.* **6**, 026007 (2011).

42. A. Villoslada, A. Flores, D. Copaci, D. Blanco, L. Moreno, High-displacement flexible Shape Memory Alloy actuator for soft wearable robots. *Robot. Auton. Syst.* **73**, 91–101 (2015).

43. Z. Wang, G. Hang, Y. Wang, J. Li, W. Du, Embedded SMA wire actuated biomimetic fin: a module for biomimetic underwater propulsion. *Smart Mater. Struct.* **17**, 025039 (2008).

44. A. Villanueva, C. Smith, S. Priya, A biomimetic robotic jellyfish (Robojelly) actuated by shape memory alloy composite actuators. *Bioinspir. Biomim.* **6**, 036004 (2011).

45. S. Kim, E. Hawkes, K. Choy, M. Joldaz, J. Foleyz, R. Wood, in *2009 IEEE/RSJ International Conference on Intelligent Robots and Systems* (IEEE, St. Louis, MO, USA, 2009; http://ieeexplore.ieee.org/document/5354178/), pp. 2228–2234.

46. Z. Zhakypov, F. Heremans, A. Billard, J. Paik, An Origami-Inspired Reconfigurable Suction Gripper for Picking Objects With Variable Shape and Size. *IEEE Robot. Autom. Lett.* **3**, 2894–2901 (2018).

47. Y. Yang, M. Zhang, D. Li, Y. Shen, Graphene-Based Light-Driven Soft Robot with Snake-Inspired Concertina and Serpentine Locomotion. *Adv. Mater. Technol.* **4**, 1800366 (2019).

48. X. Zhang, C. L. Pint, M. H. Lee, B. E. Schubert, A. Jamshidi, K. Takei, H. Ko, A. Gillies, R. Bardhan, J. J. Urban, M. Wu, R. Fearing, A. Javey, Optically- and Thermally-Responsive Programmable Materials Based on Carbon Nanotube-Hydrogel Polymer Composites. *Nano Lett.* **11**, 3239–3244 (2011).

49. S. Taccola, F. Greco, E. Sinibaldi, A. Mondini, B. Mazzolai, V. Mattoli, Toward a New Generation of Electrically Controllable Hygromorphic Soft Actuators. *Adv. Mater.* **27**, 1668–1675 (2015).

50. H. Lu, M. Zhang, Y. Yang, Q. Huang, T. Fukuda, Z. Wang, Y. Shen, A bioinspired multi-legged soft millirobot that functions in both dry and wet conditions. *Nat. Commun.* **9** (2018), doi:10.1038/s41467-018-06491-9.

51. E. Diller, J. Zhuang, G. Zhan Lum, M. R. Edwards, M. Sitti, Continuously distributed magnetization profile for millimeter-scale elastomeric undulatory swimming. *Appl. Phys. Lett.* **104**, 174101 (2014).

52. Y. Kim, H. Yuk, R. Zhao, S. A. Chester, X. Zhao, Printing ferromagnetic domains for untethered fast-transforming soft materials. *Nature*. **558**, 274–279 (2018).

53. M. Li, Y. Wang, A. Chen, A. Naidu, B. S. Napier, W. Li, C. L. Rodriguez, S. A. Crooker, F. G. Omenetto, Flexible magnetic composites for light-controlled actuation and interfaces. *Proc. Natl. Acad. Sci.* **115**, 8119–8124 (2018).

54. F. Fiorillo, G. Bertotti, C. Appino, M. Pasquale, in *Wiley Encyclopedia of Electrical and Electronics Engineering* (John Wiley & Sons, Inc., Hoboken, NJ, USA, 1999; http://doi.wiley.com/10.1002/047134608X.W4504.pub2), pp. 1–42.

55. S. Jeon, A. K. Hoshiar, K. Kim, S. Lee, E. Kim, S. Lee, J. Kim, B. J. Nelson, H.-J. Cha, B.-J. Yi, H. Choi, A Magnetically Controlled Soft Microrobot Steering a Guidewire in a Three-Dimensional Phantom Vascular Network. *Soft Robot.* **6**, 54–68 (2019).

56. I. Must, F. Kaasik, I. Põldsalu, L. Mihkels, U. Johanson, A. Punning, A. Aabloo, Ionic and Capacitive Artificial Muscle for Biomimetic Soft Robotics: Ionic and Capacitive Artificial Muscle for Biomimetic Soft Robotics. *Adv. Eng. Mater.* **17**, 84–94 (2015).

57. M. Duduta, E. Hajiesmaili, H. Zhao, R. J. Wood, D. R. Clarke, Realizing the potential of dielectric elastomer artificial muscles. *Proc. Natl. Acad. Sci.*, 201815053 (2019).

58. N. Kellaris, V. Gopaluni Venkata, G. M. Smith, S. K. Mitchell, C. Keplinger, Peano-HA-SEL actuators: Muscle-mimetic, electrohydraulic transducers that linearly contract on activation. *Sci. Robot.* **3**, eaar3276 (2018).

59. E. Acome, S. K. Mitchell, T. G. Morrissey, M. B. Emmett, C. Benjamin, M. King, M. Radakovitz, C. Keplinger, Hydraulically amplified self-healing electrostatic actuators with muscle-like performance. *Science.* **359**, 61–65 (2018).

60. H. S. Wang, J. Cho, D. S. Song, J. H. Jang, J. Y. Jho, J. H. Park, High-Performance Electroactive Polymer Actuators Based on Ultrathick Ionic Polymer–Metal Composites with Nanodispersed Metal Electrodes. *ACS Appl. Mater. Interfaces.* **9**, 21998–22005 (2017).

61. A. Maziz, C. Plesse, C. Soyer, C. Chevrot, D. Teyssié, E. Cattan, F. Vidal, Demonstrating kHz Frequency Actuation for Conducting Polymer Microactuators. *Adv. Funct. Mater.* **24**, 4851–4859 (2014).

62. E. W. H. Jager, Microrobots for Micrometer-Size Objects in Aqueous Media: Potential Tools for Single-Cell Manipulation. *Science.* **288**, 2335–2338 (2000).

63. Zheng Chen, S. Shatara, Xiaobo Tan, Modeling of Biomimetic Robotic Fish Propelled by An Ionic Polymer–Metal Composite Caudal Fin. *IEEEASME Trans. Mechatron.* **15**, 448–459 (2010).

64. A. Kodaira, K. Asaka, T. Horiuchi, G. Endo, H. Nabae, K. Suzumori, IPMC Monolithic Thin Film Robots Fabricated Through a Multi-Layer Casting Process. *IEEE Robot. Autom. Lett.* **4**, 1335–1342 (2019).

65. R. Pelrine, High-Speed Electrically Actuated Elastomers with Strain Greater Than 100%. *Science.* **287**, 836–839 (2000).

66. M. Duduta, R. J. Wood, D. R. Clarke, Multilayer Dielectric Elastomers for Fast, Programmable Actuation without Prestretch. *Adv. Mater.* **28**, 8058–8063 (2016).

67. Y. Fuchigami, T. Takigawa, K. Urayama, Electrical Actuation of Cholesteric Liquid Crystal Gels. *ACS Macro Lett.* **3**, 813–818 (2014).

68. Y. S. Kim, M. Liu, Y. Ishida, Y. Ebina, M. Osada, T. Sasaki, T. Hikima, M. Takata, T. Aida, Thermoresponsive actuation enabled by permittivity switching in an electrostatically anisotropic hydrogel. *Nat. Mater.* **14**, 1002–1007 (2015).

69. J. W. Bae, E.-J. Shin, J. Jeong, D.-S. Choi, J. E. Lee, B. U. Nam, L. Lin, S.-Y. Kim, High-Performance PVC Gel for Adaptive Micro-Lenses with Variable Focal Length. *Sci. Rep.* **7** (2017), doi:10.1038/s41598-017-02324-9.

70. S. Maeda, Y. Hara, T. Sakai, R. Yoshida, S. Hashimoto, Self-Walking Gel. *Adv. Mater.* **19**, 3480–3484 (2007).

71. B. Tondu, Modelling of the McKibben artificial muscle: A review. *J. Intell. Mater. Syst. Struct.* **23**, 225–253 (2012).

72. M. T. Tolley, R. F. Shepherd, M. Karpelson, N. W. Bartlett, K. C. Galloway, M. Wehner, R. Nunes, G. M. Whitesides, R. J. Wood, in *2014 IEEE/RSJ International Conference on Intelligent Robots and Systems* (IEEE, Chicago, IL, USA, 2014; http://ieeexplore.ieee.org/document/6942615/), pp. 561–566.

73. H. A. Sonar, J. Paik, Soft Pneumatic Actuator Skin with Piezoelectric Sensors for Vibrotactile Feedback. *Front. Robot. AI.* **2** (2016), doi:10.3389/frobt.2015.00038.

74. J. Zhang, J. Sheng, C. T. O'Neill, C. J. Walsh, R. J. Wood, J.-H. Ryu, J. P. Desai, M. C. Yip, Robotic Artificial Muscles: Current Progress and Future Perspectives, 21.

75. J. Maas, D. Tepel, T. Hoffstadt, Actuator design and automated manufacturing process for DEAP-based multilayer stack-actuators. *Meccanica.* **50**, 2839–2854 (2015).

76. S. Shian, D. R. Clarke, Electrically-tunable surface deformation of a soft elastomer. *Soft Matter.* **12**, 3137–3141 (2016).

77. A. She, S. Zhang, S. Shian, D. R. Clarke, F. Capasso, Adaptive metalenses with simultaneous electrical control of focal length, astigmatism, and shift. *Sci. Adv.* **4**, eaap9957 (2018).

78. S. Akbari, H. R. Shea, Microfabrication and characterization of an array of dielectric elastomer actuators generating uniaxial strain to stretch individual cells. *J. Micromechanics Microengineering.* **22**, 045020 (2012).

79. A. Poulin, C. Saygili Demir, S. Rosset, T. V. Petrova, H. Shea, Dielectric elastomer actuator for mechanical loading of 2D cell cultures. *Lab. Chip.* **16**, 3788–3794 (2016).

80. A. Poulin, M. Imboden, F. Sorba, S. Grazioli, C. Martin-Olmos, S. Rosset, H. Shea, An ultra-fast mechanically active cell culture substrate. *Sci. Rep.* **8** (2018), doi:10.1038/s41598-018-27915-y.

81. M. Imboden, E. de Coulon, A. Poulin, C. Dellenbach, S. Rosset, H. Shea, S. Rohr, High-speed mechano-active multielectrode array for investigating rapid stretch effects on cardiac tissue. *Nat. Commun.* **10** (2019), doi:10.1038/s41467-019-08757-2.

82. C. Keplinger, J.-Y. Sun, C. C. Foo, P. Rothemund, G. M. Whitesides, Z. Suo, Stretchable, Transparent, Ionic Conductors. *Science.* **341**, 984–987 (2013).

83. G.-Y. Gu, J. Zhu, L.-M. Zhu, X. Zhu, A survey on dielectric elastomer actuators for soft robots. *Bioinspir. Biomim.* **12**, 011003 (2017).

84. K. Jung, J. C. Koo, J. Nam, Y. K. Lee, H. R. Choi, Artificial annelid robot driven by soft actuators. *Bioinspir. Biomim.* **2**, S42–S49 (2007).

85. G. Gu, J. Zou, R. Zhao, X. Zhao, X. Zhu, Soft wall-climbing robots. *Sci. Robot.*, 13 (2018).

86. L. Xu, H.-Q. Chen, J. Zou, W.-T. Dong, G.-Y. Gu, L.-M. Zhu, X.-Y. Zhu, Bio-inspired annelid robot: a dielectric elastomer actuated soft robot. *Bioinspir. Biomim.* **12**, 025003 (2017).

87. T. Li, Z. Zou, G. Mao, X. Yang, Y. Liang, C. Li, S. Qu, Z. Suo, W. Yang, Agile and Resilient Insect-Scale Robot. *Soft Robot.* **6**, 133–141 (2019).

88. C. T. Nguyen, H. Phung, T. D. Nguyen, H. Jung, H. R. Choi, Multiple-degrees-of-freedom dielectric elastomer actuators for soft printable hexapod robot. *Sens. Actuators Phys.* **267**, 505–516 (2017).

89. M. Duduta, D. R. Clarke, R. J. Wood, in *2017 IEEE International Conference on Robotics and Automation (ICRA)* (IEEE, Singapore, Singapore, 2017; http://ieeexplore.ieee.org/document/7989501/), pp. 4346–4351.

90. M. T. Petralia, R. J. Wood, in *2010 IEEE/RSJ International Conference on Intelligent Robots and Systems* (IEEE, Taipei, 2010; http://ieeexplore.ieee.org/document/5652506/), pp. 2357–2363.

91. Q. Pei, M. Rosenthal, S. Stanford, H. Prahlad, R. Pelrine, Multiple-degrees-of-freedom electroelastomer roll actuators. *Smart Mater. Struct.* **13**, N86–N92 (2004).

92. R. Pelrine, R. D. Kornbluh, Q. Pei, S. Stanford, S. Oh, J. Eckerle, R. J. Full, M. A. Rosenthal, K. Meijer, Y. Bar-Cohen, Ed. (San Diego, CA, 2002; http://proceedings.spiedigitallibrary.org/proceeding.aspx?articleid=882848), pp. 126–137.

93. C. T. Nguyen, H. Phung, T. D. Nguyen, C. Lee, U. Kim, D. Lee, H. Moon, J. Koo, J. Nam, H. R. Choi, A small biomimetic quadruped robot driven by multistacked dielectric elastomer actuators. *Smart Mater. Struct.* **23**, 065005 (2014).

94. Q. Pei, R. Pelrine, M. A. Rosenthal, S. Stanford, H. Prahlad, R. D. Kornbluh, Y. Bar-Cohen, Ed. (San Diego, CA, 2004; http://proceedings.spiedigitallibrary.org/proceeding.aspx?doi=10.1117/12.540462), p. 41.

95. J. Cao, L. Qin, J. Liu, Q. Ren, C. C. Foo, H. Wang, H. P. Lee, J. Zhu, Untethered soft robot capable of stable locomotion using soft electrostatic actuators. *Extreme Mech. Lett.* **21**, 9–16 (2018).

96. J.-S. Plante, L. M. Devita, S. Dubowsky, Y. Bar-Cohen, Ed. (San Diego, California, 2007; http://proceedings.spiedigitallibrary.org/proceeding.aspx?doi=10.1117/12.715236), p. 652406.

97. S. Rosset, H. R. Shea, Y. Bar-Cohen, Ed. (San Diego, California, United States, 2015; http://proceedings.spiedigitallibrary.org/proceeding.aspx?doi=10.1117/12.2085279), p. 943009.

98. I. A. Anderson, T. Hale, T. Gisby, T. Inamura, T. McKay, B. O'Brien, S. Walbran, E. P. Calius, A thin membrane artificial muscle rotary motor. *Appl. Phys. A.* **98**, 75–83 (2010).

99. A. Minaminosono, H. Shigemune, Y. Okuno, T. Katsumata, N. Hosoya, S. Maeda, A Deformable Motor Driven by Dielectric Elastomer Actuators and Flexible Mechanisms. *Front. Robot. AI.* **6** (2019), doi:10.3389/frobt.2019.00001.

100. W.-B. Li, W.-M. Zhang, H.-X. Zou, Z.-K. Peng, G. Meng, Multisegment annular dielectric elastomer actuators for soft robots. *Smart Mater. Struct.* **27**, 115024 (2018).

101. M. Artusi, M. Potz, J. Aristizabal, C. Menon, S. Cocuzza, S. Debei, Electroactive Elastomeric Actuators for the Implementation of a Deformable Spherical Rover. *IEEEASME Trans. Mechatron.* **16**, 50–57 (2011).

102. J. Shintake, V. Cacucciolo, H. Shea, D. Floreano, Soft Biomimetic Fish Robot Made of Dielectric Elastomer Actuators. *Soft Robot.* **5**, 466–474 (2018).

103. C. Christianson, N. N. Goldberg, D. D. Deheyn, S. Cai, M. T. Tolley, Translucent soft robots driven by frameless fluid electrode dielectric elastomer actuators. *Sci. Robot.* **3**, eaat1893 (2018).

104. H. Godaba, J. Li, Y. Wang, J. Zhu, A Soft Jellyfish Robot Driven by a Dielectric Elastomer Actuator. *IEEE Robot. Autom. Lett.* **1**, 624–631 (2016).

105. B. Liu, F. Chen, S. Wang, Z. Fu, T. Cheng, T. Li, Electromechanical Control and Stability Analysis of a Soft Swim-Bladder Robot Driven by Dielectric Elastomer. *J. Appl. Mech.* **84**, 091005 (2017).

106. C. Jordi, S. Michel, E. Fink, Fish-like propulsion of an airship with planar membrane dielectric elastomer actuators. *Bioinspir. Biomim.* **5**, 026007 (2010).

107. T. Li, G. Li, Y. Liang, T. Cheng, J. Dai, X. Yang, B. Liu, Z. Zeng, Z. Huang, Y. Luo, T. Xie, W. Yang, Fast-moving soft electronic fish. *Sci. Adv.*, 8 (2017).

108. S. Shian, K. Bertoldi, D. R. Clarke, Dielectric Elastomer Based "Grippers" for Soft Robotics. *Adv. Mater.* **27**, 6814–6819 (2015).

109. G. Kofod, W. Wirges, M. Paajanen, S. Bauer, Energy minimization for self-organized structure formation and actuation. *Appl. Phys. Lett.* **90**, 081916 (2007).

110. J. Shintake, S. Rosset, B. Schubert, D. Floreano, H. Shea, Versatile Soft Grippers with Intrinsic Electroadhesion Based on Multifunctional Polymer Actuators. *Adv. Mater.* **28**, 231–238 (2016).

111. H. Zhang, Y. Zhou, M. Dai, Z. Zhang, A novel flying robot system driven by dielectric elastomer balloon actuators. *J. Intell. Mater. Syst. Struct.* **29**, 2522–2527 (2018).

112. F. Carpi, A. Mannini, D. De Rossi, Y. Bar-Cohen, Ed. (San Diego, California, 2008; http://proceedings.spiedigitallibrary.org/proceeding.aspx?doi=10.1117/12.774644), p. 692705.

113. H. Boys, G. Frediani, M. Ghilardi, S. Poslad, J. C. Busfield, F. Carpi, in *2018 IEEE International Conference on Soft Robotics (RoboSoft)* (IEEE, Livorno, Italy, 2018; https://ieeexplore.ieee.org/document/8404931/), pp. 270–275.

114. H. S. Lee, H. Phung, D.-H. Lee, U. K. Kim, C. T. Nguyen, H. Moon, J. C. Koo, J. Nam, H. R. Choi, Design analysis and fabrication of arrayed tactile display based on dielectric elastomer actuator. *Sens. Actuators Phys.* **205**, 191–198 (2014).

115. S. Mun, S. Yun, S. Nam, S. K. Park, S. Park, B. J. Park, J. M. Lim, K.-U. Kyung, Electro-Active Polymer Based Soft Tactile Interface for Wearable Devices. *IEEE Trans. Haptics.* **11**, 15–21 (2018).

116. L. E. Knoop, J. Rossiter, Y. Bar-Cohen, Ed. (San Diego, California, USA, 2014; http://proceedings.spiedigitallibrary.org/proceeding.aspx?doi=10.1117/12.2044572), p. 905610.

117. K. Jun, J. Kim, I.-K. Oh, An Electroactive and Transparent Haptic Interface Utilizing Soft Elastomer Actuators with Silver Nanowire Electrodes. *Small.* **14**, 1801603 (2018).

118. G. Frediani, D. Mazzei, D. E. De Rossi, F. Carpi, Wearable Wireless Tactile Display for Virtual Interactions with Soft Bodies. *Front. Bioeng. Biotechnol.* **2** (2014), doi:10.3389/fbioe.2014.00031.

119. P. Jean, A. Wattez, G. Ardoise, C. Melis, R. Van Kessel, A. Fourmon, E. Barrabino, J. Heemskerk, J. P. Queau, Y. Bar-Cohen, Ed. (San Diego, California, 2012; http://proceedings.spiedigitallibrary.org/proceeding.aspx?doi=10.1117/12.934222), p. 83400C.

120. T. G. McKay, B. M. O'Brien, E. P. Calius, I. A. Anderson, Soft generators using dielectric elastomers. *Appl. Phys. Lett.* **98**, 142903 (2011).

121. S. J. A. Koh, C. Keplinger, T. Li, S. Bauer, Z. Suo, Dielectric Elastomer Generators: How Much Energy Can Be Converted? *IEEEASME Trans. Mechatron.* **16**, 33–41 (2011).

122. R. D. Kornbluh, R. Pelrine, H. Prahlad, A. Wong-Foy, B. McCoy, S. Kim, J. Eckerle, T. Low, Y. Bar-Cohen, F. Carpi, Eds. (San Diego, California, USA, 2011; http://proceedings.spiedigitallibrary.org/proceeding.aspx?doi=10.1117/12.882367), p. 797605.

123. G. Moretti, G. P. R. Papini, M. Righi, D. Forehand, D. Ingram, R. Vertechy, M. Fontana, Resonant wave energy harvester based on dielectric elastomer generator. *Smart Mater. Struct.* **27**, 035015 (2018).

124. J. Cheng, Z. Jia, T. Li, Dielectric-elastomer-based capacitive force sensing with tunable and enhanced sensitivity. *Extreme Mech. Lett.* **21**, 49–56 (2018).

125. H. Böse, M. Thuy, S. Stier, in *Electroactive Polymer Actuators and Devices (EAPAD) XX*, Y. Bar-Cohen, Ed. (SPIE, Denver, United States, 2018; https://www.spiedigitallibrary.org/conference-proceedings-of-spie/10594/2297212/Wearable-operation-device-with-different-types-of-dielectric-elastomer-sensors/10.1117/12.2297212.full), p. 30.

126. T. A. Gisby, B. M. O'Brien, I. A. Anderson, Self sensing feedback for dielectric elastomer actuators. *Appl. Phys. Lett.* **102**, 193703 (2013).

127. B. O'Brien, J. Thode, I. Anderson, E. Calius, E. Haemmerle, S. Xie, Y. Bar-Cohen, Ed. (San Diego, California, 2007; http://proceedings.spiedigitallibrary.org/proceeding.aspx?doi=10.1117/12.715823), p. 652415.

128. R. E. Pelrine, R. D. Kornbluh, J. P. Joseph, Electrostriction of polymer dielectrics with compliant electrodes as a means of actuation. *Sens. Actuators Phys.* **64**, 77–85 (1998).

129. R. V. Mateiu, L. Yu, A. L. Skov, Y. Bar-Cohen, Ed. (Portland, Oregon, United States, 2017; http://proceedings.spiedigitallibrary.org/proceeding.aspx?doi=10.1117/12.2258719), p. 1016328.

130. D. Gatti, H. Haus, M. Matysek, B. Frohnapfel, C. Tropea, H. F. Schlaak, The dielectric breakdown limit of silicone dielectric elastomer actuators. *Appl. Phys. Lett.* **104**, 052905 (2014).

131. L. Duan, J. Zhang, M. Zhang, C.-H. Li, J.-L. Zuo, Increasing the breakdown strength of dielectric actuators by using Cu/Cu $_x$ O/silicone dielectric elastomers. *J. Mater. Chem. C*. **6**, 12175–12179 (2018).

132. S. J. A. Koh, T. Li, J. Zhou, X. Zhao, W. Hong, J. Zhu, Z. Suo, Mechanisms of large actuation strain in dielectric elastomers. *J. Polym. Sci. Part B Polym. Phys.* **49**, 504–515 (2011).

133. X. Zhao, Z. Suo, Theory of Dielectric Elastomers Capable of Giant Deformation of Actuation. *Phys. Rev. Lett.* **104** (2010), doi:10.1103/PhysRevLett.104.178302.

134. R. Pelrine, R. Kornbluh, in *Electromechanically Active Polymers: A Concise Reference*, F. Carpi, Ed. (Springer International Publishing, Cham, 2016; https://doi.org/10.1007/978-3-319-31530-0_30), *Polymers and Polymeric Composites: A Reference Series*, pp. 671–686.

135. F. B. Madsen, A. E. Daugaard, S. Hvilsted, A. L. Skov, The Current State of Silicone-Based Dielectric Elastomer Transducers. *Macromol. Rapid Commun.* **37**, 378–413 (2016).

136. D. M. Opris, Polar Elastomers as Novel Materials for Electromechanical Actuator Applications. *Adv. Mater.* **30**, 1703678 (2018).

137. X. Niu, H. Stoyanov, W. Hu, R. Leo, P. Brochu, Q. Pei, Synthesizing a new dielectric elastomer exhibiting large actuation strain and suppressed electromechanical instability without prestretching. *J. Polym. Sci. Part B Polym. Phys.* **51**, 197–206 (2013).

138. P. Brochu, Q. Pei, Advances in Dielectric Elastomers for Actuators and Artificial Muscles. *Macromol. Rapid Commun.* **31**, 10–36 (2010).

139. R. Pelrine, R. Kornbluh, J. Joseph, R. Heydt, Q. Pei, S. Chiba, High-field deformation of elastomeric dielectrics for actuators. *Mater. Sci. Eng. C*. **11**, 89–100 (2000).

140. K. Jung, J. Lee, M. Cho, J. C. Koo, J. Nam, Y. Lee, H. R. Choi, Development of enhanced synthetic elastomer for energy-efficient polymer actuators. *Smart Mater. Struct.* **16**, S288–S294 (2007).

141. R. Shankar, T. K. Ghosh, R. J. Spontak, Electroactive Nanostructured Polymers as Tunable Actuators. *Adv. Mater.* **19**, 2218–2223 (2007).

142. S. M. Ha, W. Yuan, Q. Pei, R. Pelrine, S. Stanford, Interpenetrating Polymer Networks for High-Performance Electroelastomer Artificial Muscles. *Adv. Mater.* **18**, 887–891 (2006).

143. X. Niu, X. Yang, P. Brochu, H. Stoyanov, S. Yun, Z. Yu, Q. Pei, Bistable Large-Strain Actuation of Interpenetrating Polymer Networks. *Adv. Mater.* **24**, 6513–6519 (2012).

144. S. Rosset, O. A. Araromi, S. Schlatter, H. R. Shea, Fabrication Process of Silicone-based Dielectric Elastomer Actuators. *JoVE J. Vis. Exp.*, e53423 (2016).

145. C. A. de Saint-Aubin, S. Rosset, S. Schlatter, H. Shea, High-cycle electromechanical aging of dielectric elastomer actuators with carbon-based electrodes. *Smart Mater. Struct.* **27**, 074002 (2018).

146. S. Rosset, H. R. Shea, Flexible and stretchable electrodes for dielectric elastomer actuators. *Appl. Phys. A*. **110**, 281–307 (2013).

147. D. McCoul, W. Hu, M. Gao, V. Mehta, Q. Pei, Recent Advances in Stretchable and Transparent Electronic Materials. *Adv. Electron. Mater.* **2**, 1500407 (2016).

148. C. Cao, S. Burgess, A. T. Conn, Toward a Dielectric Elastomer Resonator Driven Flapping Wing Micro Air Vehicle. *Front. Robot. AI.* **5** (2019), doi:10.3389/frobt.2018.00137.

149. F. Carpi, D. De Rossi, Dielectric elastomer cylindrical actuators: electromechanical modelling and experimental evaluation. *Mater. Sci. Eng. C*. **24**, 555–562 (2004).

150. S. Rosset, B. M. O'Brien, T. Gisby, D. Xu, H. R. Shea, I. A. Anderson, Self-sensing dielectric elastomer actuators in closed-loop operation. *Smart Mater. Struct.* **22**, 104018 (2013).

151. B. M. O'Brien, E. P. Calius, T. Inamura, S. Q. Xie, I. A. Anderson, Dielectric elastomer switches for smart artificial muscles. *Appl. Phys. A*. **100**, 385–389 (2010).

152. S. Schlatter, S. Rosset, H. Shea, Y. Bar-Cohen, Ed. (Portland, Oregon, United States, 2017; http://proceedings.spiedigitallibrary.org/proceeding.aspx?doi=10.1117/12.2258615), p. 1016311.

153. A. Poulin, S. Rosset, H. R. Shea, Printing low-voltage dielectric elastomer actuators. *Appl. Phys. Lett.* **107**, 244104 (2015).

154. F. Carpi, C. Salaris, D. D. Rossi, Folded dielectric elastomer actuators. *Smart Mater. Struct.* **16**, S300–S305 (2007).

155.   F. Carpi, A. Migliore, G. Serra, D. D. Rossi, Helical dielectric elastomer actuators. *Smart Mater. Struct.* **14**, 1210–1216 (2005).

156.   M. B. Krishnan, S. Rosset, S. Bhattacharya, H. R. Shea, Fabrication of transmissive dielectric elastomer actuator driven tunable optical gratings with improved tunability. *Opt. Eng.* **55**, 047104 (2016).

157.   P. Lochmatter, G. Kovacs, Design and characterization of an active hinge segment based on soft dielectric EAPs. *Sens. Actuators Phys.* **141**, 577–587 (2008).

158.   N. H. Chuc, N. H. L. Vuong, D. S. Kim, H. P. Moon, J. C. Koo, Y. K. Lee, J.-D. Nam, H. R. Choi, Fabrication and Control of Rectilinear Artificial Muscle Actuator. *IEEEASME Trans. Mechatron.* **16**, 167–176 (2011).

159.   O. A. Araromi, A. T. Conn, C. S. Ling, J. M. Rossiter, R. Vaidyanathan, S. C. Burgess, Spray deposited multilayered dielectric elastomer actuators. *Sens. Actuators Phys.* **167**, 459–467 (2011).

160.   P. Lotz, M. Matysek, H. F. Schlaak, Fabrication and Application of Miniaturized Dielectric Elastomer Stack Actuators. *IEEEASME Trans. Mechatron.* **16**, 58–66 (2011).

161.   M. Aschwanden, D. Niederer, A. Stemmer, Y. Bar-Cohen, Ed. (San Diego, California, 2008; http://proceedings.spiedigitallibrary.org/proceeding.aspx?doi=10.1117/12.776100), p. 69271R.

162.   W. Yuan, L. B. Hu, Z. B. Yu, T. Lam, J. Biggs, S. M. Ha, D. J. Xi, B. Chen, M. K. Senesky, G. Grüner, Q. Pei, Fault-Tolerant Dielectric Elastomer Actuators using Single-Walled Carbon Nanotube Electrodes. *Adv. Mater.* **20**, 621–625 (2008).

163.   L. Hu, W. Yuan, P. Brochu, G. Gruner, Q. Pei, Highly stretchable, conductive, and transparent nanotube thin films. *Appl. Phys. Lett.* **94**, 161108 (2009).

164.   T. Töpper, F. Weiss, B. Osmani, C. Bippes, V. Leung, B. Müller, Siloxane-based thin films for biomimetic low-voltage dielectric actuators. *Sens. Actuators Phys.* **233**, 32–41 (2015).

165.   A. Pimpin, Y. Suzuki, N. Kasagi, Microelectrostrictive Actuator With Large Out-of-Plane Deformation for Flow-Control Application. *J. Microelectromechanical Syst.* **16**, 753–764 (2007).

166.   R. W. Jones, R. Sarban, Inverse grey-box model-based control of a dielectric elastomer actuator. *Smart Mater. Struct.* **21**, 075019 (2012).

167.   S. Rosset, M. Niklaus, P. Dubois, H. R. Shea, Metal Ion Implantation for the Fabrication of Stretchable Electrodes on Elastomers. *Adv. Funct. Mater.* **19**, 470–478 (2009).

168.   S. Yun, X. Niu, Z. Yu, W. Hu, P. Brochu, Q. Pei, Compliant Silver Nanowire-Polymer Composite Electrodes for Bistable Large Strain Actuation. *Adv. Mater.* **24**, 1321–1327 (2012).

169. L. R. Finkenauer, C. Majidi, Y. Bar-Cohen, Ed. (San Diego, California, USA, 2014; http://proceedings.spiedigitallibrary.org/proceeding.aspx?doi=10.1117/12.2049112), p. 90563I.

170. M. Niklaus, H. R. Shea, Electrical conductivity and Young's modulus of flexible nano-composites made by metal-ion implantation of polydimethylsiloxane: The relationship between nanostructure and macroscopic properties. *Acta Mater.* **59**, 830–840 (2011).

171. G. Corbelli, C. Ghisleri, M. Marelli, P. Milani, L. Ravagnan, Highly Deformable Nanostructured Elastomeric Electrodes With Improving Conductivity Upon Cyclical Stretching. *Adv. Mater.* **23**, 4504–4508 (2011).

172. N. Pekas, Q. Zhang, D. Juncker, Electrostatic actuator with liquid metal–elastomer compliant electrodes used for on-chip microvalving. *J. Micromechanics Microengineering*. **22**, 097001 (2012).

173. L. R. Finkenauer, C. Majidi, Y. Bar-Cohen, Ed. (San Diego, California, USA, 2014; http://proceedings.spiedigitallibrary.org/proceeding.aspx?doi=10.1117/12.2049112), p. 90563I.

174. B. Chen, Y. Bai, F. Xiang, J.-Y. Sun, Y. Mei Chen, H. Wang, J. Zhou, Z. Suo, Stretchable and transparent hydrogels as soft conductors for dielectric elastomer actuators. *J. Polym. Sci. Part B Polym. Phys.* **52**, 1055–1060 (2014).

175. W. Yuan, T. Lam, J. Biggs, L. Hu, Z. Yu, S. Ha, D. Xi, M. K. Senesky, G. Grüner, Q. Pei, Y. Bar-Cohen, Ed. (San Diego, California, 2007; http://proceedings.spiedigitallibrary.org/proceeding.aspx?doi=10.1117/12.715383), p. 65240N.

176. T. Lam, H. Tran, W. Yuan, Z. Yu, S. Ha, R. Kaner, Q. Pei, Y. Bar-Cohen, Ed. (San Diego, California, 2008; http://proceedings.spiedigitallibrary.org/proceeding.aspx?doi=10.1117/12.776817), p. 69270O.

177. A. Poulin, S. Rosset, H. R. Shea, Printing low-voltage dielectric elastomer actuators. *Appl. Phys. Lett.* **107**, 244104 (2015).

178. D. McCoul, S. Rosset, S. Schlatter, H. Shea, Inkjet 3D printing of UV and thermal cure silicone elastomers for dielectric elastomer actuators. *Smart Mater. Struct.* **26**, 125022 (2017).

179. R. Palakodeti, M. R. Kessler, Influence of frequency and prestrain on the mechanical efficiency of dielectric electroactive polymer actuators. *Mater. Lett.* **60**, 3437–3440 (2006).

180. S. Akbari, S. Rosset, H. R. Shea, Improved electromechanical behavior in castable dielectric elastomer actuators. *Appl. Phys. Lett.* **102**, 071906 (2013).

181. G. Kofod, P. Sommer-Larsen, R. Kornbluh, R. Pelrine, Actuation Response of Polyacrylate Dielectric Elastomers. *J. Intell. Mater. Syst. Struct.* **14**, 787–793 (2003).

182. G. Kovacs, L. Düring, S. Michel, G. Terrasi, Stacked dielectric elastomer actuator for tensile force transmission. *Sens. Actuators Phys.* **155**, 299–307 (2009).

183.   S. Hau, G. Rizzello, S. Seelecke, A novel dielectric elastomer membrane actuator concept for high-force applications. *Extreme Mech. Lett.* **23**, 24–28 (2018).

184.   H. Zhao, A. M. Hussain, M. Duduta, D. M. Vogt, R. J. Wood, D. R. Clarke, Compact Dielectric Elastomer Linear Actuators. *Adv. Funct. Mater.* **28**, 1804328 (2018).

185.   M. Randazzo, R. Buzio, G. Metta, G. Sandini, U. Valbusa, Y. Bar-Cohen, Ed. (San Diego, California, 2008; http://proceedings.spiedigitallibrary.org/proceeding.aspx?doi=10.1117/12.784981), p. 69272D.

186.   G.-K. Lau, H.-T. Lim, J.-Y. Teo, Y.-W. Chin, Lightweight mechanical amplifiers for rolled dielectric elastomer actuators and their integration with bio-inspired wing flappers. *Smart Mater. Struct.* **23**, 025021 (2014).

187.   C. Tang, B. Li, H. Fang, Z. Li, H. Chen, A speedy, amphibian, robotic cube: Resonance actuation by a dielectric elastomer. *Sens. Actuators Phys.* **270**, 1–7 (2018).

188.   M. Sfakiotakis, D. M. Lane, J. B. C. Davies, Review of fish swimming modes for aquatic locomotion. *IEEE J. Ocean. Eng.* **24**, 237–252 (1999).

189.   K. Y. Ma, P. Chirarattananon, S. B. Fuller, R. J. Wood, Controlled Flight of a Biologically Inspired, Insect-Scale Robot. *Science*. **340**, 603 (2013).

190.   C. Pan, E. J. Markvicka, M. H. Malakooti, J. Yan, L. Hu, K. Matyjaszewski, C. Majidi, A Liquid-Metal–Elastomer Nanocomposite for Stretchable Dielectric Materials. *Adv. Mater.*, 1900663 (2019).

191.   S. J. Dünki, Y. S. Ko, F. A. Nüesch, D. M. Opris, Self-Repairable, High Permittivity Dielectric Elastomers with Large Actuation Strains at Low Electric Fields. *Adv. Funct. Mater.* **25**, 2467–2475 (2015).

192.   K. Watanabe, T. Hoshino, K. Kanda, Y. Haruyama, S. Matsui, Brilliant Blue Observation from a Morpho-Butterfly-Scale Quasi-Structure. *Jpn. J. Appl. Phys.* **44**, L48 (2004).

193.   S. C. Truxal, K. Kurabayashi, Y.-C. Tung, Design of a MEMS Tunable Polymer Grating for Single Detector Spectroscopy. *Int. J. Optomechatronics*. **2**, 75–87 (2008).

194.   Z. Jie, Z. Yong, S. Jiyong, W. Ning, W. Wei, Experiments of a grating light modulator for projection display applications. *Appl. Opt.* **48**, 1675 (2009).

195.   A. Kocabas, A. Aydinli, Polymeric waveguide Bragg grating filter using soft lithography. *Opt. Express*. **14**, 10228 (2006).

196.   C. W. Wong, Y. Jeon, G. Barbastathis, S.-G. Kim, Analog Piezoelectric-Driven Tunable Gratings With Nanometer Resolution. *J. Microelectromechanical Syst.* **13**, 998–1005 (2004).

197.   X. Li, C. Antoine, D. Lee, J.-S. Wang, O. Solgaard, Tunable Blazed Gratings. *J. Microelectromechanical Syst.* **15**, 597–604 (2006).

198.   Y.-S. Yang, Y.-H. Lin, Y.-C. Hu, C.-H. Liu, A large-displacement thermal actuator designed for MEMS pitch-tunable grating. *J. Micromechanics Microengineering*. **19**, 015001 (2009).

199.   H. Yu, G. Zhou, F. S. Chau, S. K. Sinha, Tunable electromagnetically actuated liquid-filled lens. *Sens. Actuators Phys.* **167**, 602–607 (2011).

200.   N.-T. Nguyen, Micro-optofluidic Lenses: A review. *Biomicrofluidics*. **4**, 031501 (2010).

201.   S. Shian, R. M. Diebold, D. R. Clarke, Tunable lenses using transparent dielectric elastomer actuators. *Opt. Express*. **21**, 8669 (2013).

202.   F. Carpi, G. Frediani, S. Turco, D. De Rossi, Bioinspired Tunable Lens with Muscle-Like Electroactive Elastomers. *Adv. Funct. Mater.* **21**, 4152–4158 (2011).

203.   M. Aschwanden, M. Beck, A. Stemmer, Diffractive Transmission Grating Tuned by Dielectric Elastomer Actuator. *IEEE Photonics Technol. Lett.* **19**, 1090–1092 (2007).

204.   M. Kollosche, S. Döring, J. Stumpe, G. Kofod, Voltage-controlled compression for period tuning of optical surface relief gratings. *Opt. Lett.* **36**, 1389 (2011).

205.   Z. H. Fang, C. Punckt, E. Y. Leung, H. C. Schniepp, I. A. Aksay, Tuning of structural color using a dielectric actuator and multifunctional compliant electrodes. *Appl. Opt.* **49**, 6689 (2010).

206.   T. Rasmussen, The Benefits Of Transmission Grating Based Spectroscopy. (*Ibsen Photonics,* 2010).

207.   S. Rosset, O. A. Araromi, H. R. Shea, Maximizing the displacement of compact planar dielectric elastomer actuators. *Extreme Mech. Lett.* **3**, 72–81 (2015).

208.   M. P. Scott, M. Rahman, C. S. Brazel, Application of ionic liquids as low-volatility plasticizers for PMMA. *Eur. Polym. J.* **39**, 1947–1953 (2003).

209.   C. Palmer, Diffraction Grating Handbook, 271.

210.   J. Matsui, S. Yoshida, T. Mikayama, A. Aoki, T. Miyashita, Fabrication of Polymer Langmuir−Blodgett Films Containing Regioregular Poly(3-hexylthiophene) for Application to Field-Effect Transistor. *Langmuir*. **21**, 5343–5348 (2005).

211.   A. El Haitami, E. H. G. Backus, S. Cantin, Synthesis at the Air–Water Interface of a Two-Dimensional Semi-Interpenetrating Network Based on Poly(dimethylsiloxane) and Cellulose Acetate Butyrate. *Langmuir*. **30**, 11919–11927 (2014).

212.   C.-L. Lo, Y.-L. Lee, W.-P. Hsu, Behavior of mixed multi-walled carbon nanotube/P3HT monolayer at the air/water interface. *Synth. Met.* **160**, 2219–2223 (2010).

213. D. Matyszewska, E. Napora, K. Żelechowska, J. F. Biernat, R. Bilewicz, Synthesis, characterization, and interactions of single-walled carbon nanotubes modified with doxorubicin with Langmuir–Blodgett biomimetic membranes. *J. Nanoparticle Res.* **20** (2018), doi:10.1007/s11051-018-4239-x.

214. G. L. Gaines, *Insoluble monolayers at liquid-gas interfaces* (Interscience Publishers, New York, 1966).

215. A. Tao, F. Kim, C. Hess, J. Goldberger, R. He, Y. Sun, Y. Xia, P. Yang, Langmuir−Blodgett Silver Nanowire Monolayers for Molecular Sensing Using Surface-Enhanced Raman Spectroscopy. *Nano Lett.* **3**, 1229–1233 (2003).

216. V. Sgobba, G. Giancane, D. Cannoletta, A. Operamolla, O. Hassan Omar, G. M. Farinola, D. M. Guldi, L. Valli, Langmuir–Schaefer Films for Aligned Carbon Nanotubes Functionalized with a Conjugate Polymer and Photoelectrochemical Response Enhancement. *ACS Appl. Mater. Interfaces*. **6**, 153–158 (2014).

217. L. Huang, X. Hu, L. Chi, Monolayer-Mediated Growth of Organic Semiconductor Films with Improved Device Performance. *Langmuir*. **31**, 9748–9761 (2015).

218. A. Mandal, A. K. Nandi, Noncovalent Functionalization of Multiwalled Carbon Nanotube by a Polythiophene-Based Compatibilizer: Reinforcement and Conductivity Improvement in Poly(vinylidene fluoride) Films. *J. Phys. Chem. C*. **116**, 9360–9371 (2012).

219. J. Moulton, P. Smith, Electrical and mechanical properties of oriented poly(3-alkylthiophenes): 2. Effect of side-chain length. *Polymer*. **33**, 2340–2347 (1992).

220. I. M. Ward, D. W. Hadley, *An introduction to the mechanical properties of solid polymers* (19930000; https://www.bcin.ca/bcin/detail.app?id=144229).

221. J. Wirekoh, Y.-L. Park, Design of flat pneumatic artificial muscles. *Smart Mater. Struct.* **26**, 035009 (2017).

222. T. Ranzani, M. Cianchetti, G. Gerboni, I. D. Falco, A. Menciassi, A Soft Modular Manipulator for Minimally Invasive Surgery: Design and Characterization of a Single Module. *IEEE Trans. Robot.* **32**, 187–200 (2016).

223. T. Akagi, S. Dohta, S. Fujimoto, Y. Tsuji, Y. Fujiwara, Development of Flexible Thin Actuator Driven by Low Boiling Point Liquid. *Int. J. Mater. Sci. Eng.*, 55–59 (2015).

224. S. I. Rich, R. J. Wood, C. Majidi, Untethered soft robotics. *Nat. Electron.* **1**, 102–112 (2018).

225. M. Karpelson, G.-Y. Wei, R. J. Wood, Driving high voltage piezoelectric actuators in microrobotic applications. *Sens. Actuators Phys.* **176**, 78–89 (2012).

226. A. Withana, D. Groeger, J. Steimle, in *The 31st Annual ACM Symposium on User Interface Software and Technology - UIST '18* (ACM Press, Berlin, Germany, 2018; http://dl.acm.org/citation.cfm?doid=3242587.3242645), pp. 365–378.

227. S. Hénon, J. Meunier, Microscope at the Brewster angle: Direct observation of first-order phase transitions in monolayers. *Rev. Sci. Instrum.* **62**, 936–939 (1991).

228. S. Béfahy, P. Lipnik, T. Pardoen, C. Nascimento, B. Patris, P. Bertrand, S. Yunus, Thickness and Elastic Modulus of Plasma Treated PDMS Silica-like Surface Layer. *Langmuir*. **26**, 3372–3375 (2010).

229. E. Steltz, M. Seeman, S. Avadhanula, R. S. Fearing, in *2006 IEEE/RSJ International Conference on Intelligent Robots and Systems* (IEEE, Beijing, China, 2006; http://ieeexplore.ieee.org/document/4058553/), pp. 1322–1328.

230. M. Karpelson, Gu-Yeon Wei, R. J. Wood, in *2008 IEEE International Conference on Robotics and Automation* (IEEE, Pasadena, CA, USA, 2008; http://ieeexplore.ieee.org/document/4543300/), pp. 779–786.

231. R. Mottet, J. Chavanne, A. Boegli, Y. Perriard, in *2018 21st International Conference on Electrical Machines and Systems (ICEMS)* (IEEE, Jeju, 2018; https://ieeexplore.ieee.org/document/8549041/), pp. 2408–2413.

Curriculum Vitae

Xiaobin Ji

Personal data

Born 1990 in Hebei, China

Work address: EPFL - LMTS, Rue de la Maladière 71B, CH - 2000 Neuchâtel, Switzerland

     📞   +41 21 695 4463

     ✉   xiaobin.ji@epfl.ch

Education

2015 - 2019	PhD, Low-voltage fast DEAs, EPFL, Switzerland
2013 - 2015	M.A. Physics-Chemistry, Université de Cergy Pontoise, France
2010 - 2013	B.Sc. Chemistry, Université de Cergy Pontoise, France

Research experience

2018 - 2019	**Training**: "Applications and Industrialization of Electroactive Polymer Devices", Technische Univeristät Darmstadt, **Germany**
2016 - 2017	**Training**: "Microapplications", Linköping University, **Sweden**
2016 - 2017	**Training**: "Modelling and Ionic Electroactive Polymer", University of Tartu, **Estonia**
2015 - 2016	**Training**: "Miniaturized Dielectric Electroactive Polymer & Introductory meeting" EPFL, **Switzerland**
2014 - 2015	**Internship:** Laboratoire de Physicochimie des Polymères et des Interfaces, Université de Cergy Pontoise, **France** Project: "Elaboration and characterization of soft supercapacitor by building up Layer by Layer, using the polymerization in vapor phase" Supervisor: Prof. Cédric Plesse, Prof. Pierre-Henri Aubert.

Languages

Chinese: Native

French: Fluent

English: Fluent

International conferences

EuroEAP 2019, Dresden, Germany (**invited speaker**)
MRS fall 2018, Boston, USA (demonstration)
IROS 2018, Madrid, Spain (poster)
EuroEAP 2018, Lyon, France (poster)
AEPMAR 2017, Xi'an, China (speaker)
ECOF 15th 2017, Dresden, Germany (presentation)
EuroEAP 2017, Cartagena, Spain (poster)
EuroEAP 2016, Helsingør, Denmark (poster)
EuroEAP 2015, Tallinn, Estonia

Skills

Polymer design, synthesis and characterization
Software: MATLAB, SolidWorks, Office, Image J, etc.

Scholarship and award

- "Best Poster Award" by the EuroEAP society, 2018
- "Excellent student scholarship" by the Université de Cergy Pontoise, 2014-2015

List of journal publications

Published papers:

- "Stretchable monolayer electrodes for ultra-low voltage dielectric elastomer actuators"
  X. Ji, A. E. Haitami, F. Sorba, S. Rosset, G. T. Nguyen, C. Plesse, F. Vidal, H. Shea, S. Cantin.
  Sensors and Actuators B: Chemical, vol.261, p.135-143, (2018)
- "Soft tunable diffractive optics with multifunctional transparent electrodes enabling integrated actuation"
  X. Ji, S. Rosset, H. Shea.
  Applied Physics Letters, vol. 109, num. 19, p. 191901, (2016)
- "Triboelectric-TFT flip-flop for bistable latching of dielectric elastomer actuators"
  A. Marette, R. I. Haque, **X. Ji**, R. Hinchet, H. Shea, D. Briand
  Advanced Electronic Materials, Accepted.

In preparation:

- "Untethered Artificial Muscles for Autonomous Soft Machines"
  X. Ji, X. Liu, V. Cacucciolo, M. Imboden, Y. Civet, A. E. Haitami, S. Cantin, Y. Perriard, H. Shea